ORNL/HTSPC-11

ORNL Superconducting Technology Program for Electric Power Systems

Annual Report for FY 1999

April 2000

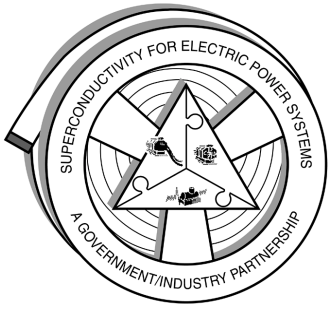

ORNL/HTSPC-11

ORNL SUPERCONDUCTING TECHNOLOGY PROGRAM FOR ELECTRIC POWER SYSTEMS

ANNUAL REPORT FOR FY 1999

Compiled by
R. A. Hawsey
A. W. Murphy

Edited by
W. S. Koncinski

Manuscript Completed: January 2000
Date Published: April 2000

Prepared for the
Office of Power Technologies
Office of Energy Efficiency and Renewable Energy
U.S. DEPARTMENT OF ENERGY
(EB 50 01 00 0)

Prepared by
OAK RIDGE NATIONAL LABORATORY
P.O. Box 2008
Oak Ridge, TN 37831-6285
Managed by
UT-Battelle, LLC,
for the
U.S. DEPARTMENT OF ENERGY
under contract DE-AC05-00OR22725

Contributors

D. B. Beach
J. D. Budai
C. Cantoni[1]
T. G. Chirayil[1]
D. K. Christen
X. Cui[1]
J. A. Demko
A. Ellis
R. Feenstra
M. J. Gouge
A. Goyal
R. A. Hawsey
H. Hsu[2]
D. R. James
B. Kang[1]
H. R. Kerchner
D. M. Kroeger
D. F. Lee
F. A. List III
S. Lu[1]
J. W. Lue
P. M. Martin
B. W. McConnell
D. P. Norton
M. Paranthaman
C. Park[1]
V. Patania
I. Sauers
S. W. Schwenterly
E. D. Specht
J. P. Stovall
D. T. Verebelyi[1]
R. K. Williams

---

[1]ORISE postdoctoral research fellow
[2]Imtech Corporation

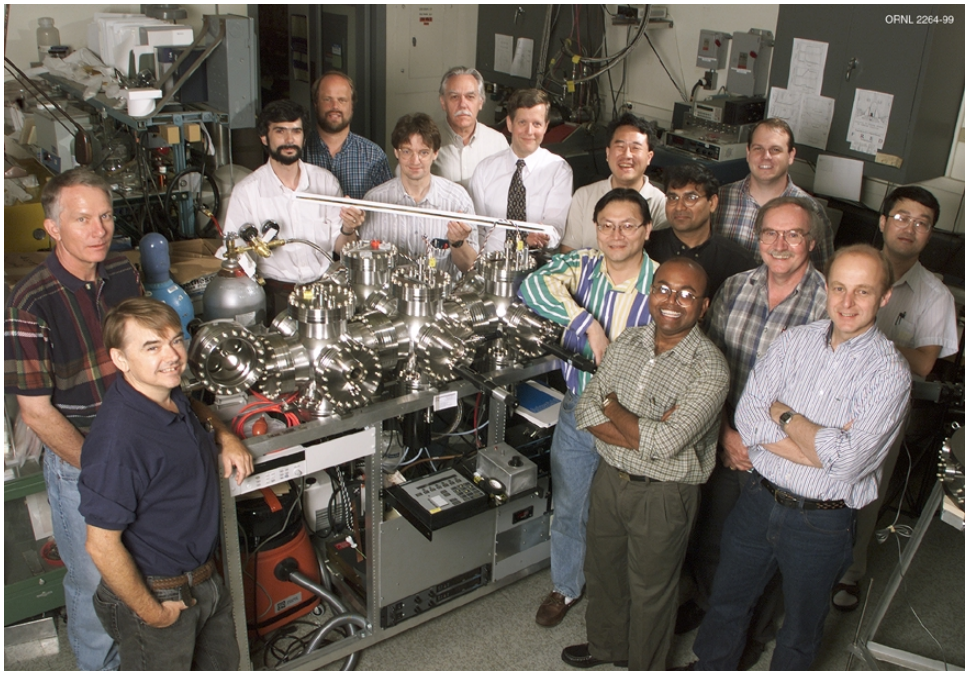

Contents

List of Figures

List of Tables

Acronyms and Initialisms

ac	alternating current
AEM	analytical electron microscopy
ANL	Argonne National Laboratory
ASC	American Superconductor Corporation
BIL	basic impulse level
BKD	backscatter Kikuchi diffraction
CCVD	combustion chemical vapor deposition
CRADA	cooperative research and development agreement
dc	direct current
DOE	U.S. Department of Energy
DOE-HQ	DOE Headquarters
DTA	differential thermal analysis
DTA/TGA	differential thermal analysis/thermogravimetric analysis
e-beam	electron beam
EDS	energy-dispersive spectroscopy
EPR	ethylene propylene rubber
FEG	field emission gun
FRP	fiber/fiberglass-reinforced plastic
FWHM	full width at half maximum
GB	grain boundary
HAGB	high-angle GB
HTS	high-temperature superconductivity/superconductor/superconducting
HV	high vacuum
IBAD	ion-beam-assisted deposition
I_c	critical current
ICP	inductively coupled plasma
IEC	International Electric Commission
IGC	Intermagnetics General Corporation
I_p	peak current
I_{rms}	root mean square cable current
J_c	critical current density
J_E	engineering critical current density
K_c	critical current per unit width of conductor (I_c/w)
KU	University of Kansas
LAGB	low-angle GB
LANL	Los Alamos National Laboratory
LN_2	liquid nitrogen
LTS	low-temperature superconductor
MOCVD	metal-organic chemical vapor deposition
MOD	metal organic decomposition
MSI	Midwest Superconductivity, Inc.
MTTR	mean time to repair
NOLD	non-Ohmic linear differential
ORNL	Oak Ridge National Laboratory
PIT	powder-in-tube
PLD	pulsed-laser deposition
$P(O_2)$	oxygen partial pressure

RABiTS™	Rolling-Assisted Biaxially Textured Substrate
RBS	Rutherford backscattering spectroscopy
RE_2O_3	rare earth oxide
rf	radio frequency
RFQ	request for quotation
RG&E	Rochester Gas and Electric Company
RHEED	reflection high-energy electron diffraction
rms	root mean square
RTA	rapid thermal annealer
SAD	selected area diffraction
SEM	scanning electron microscopy
SEM-EDAX	scanning electron microscopy–energy-dispersive X-ray microanalysis
s.f.	self-field
SFO	surface flashover
SGB	single-grain boundary
SIMS	secondary ion mass spectrometry
SMES	Superconducting Magnetic Energy Storage
SPI	Superconductivity Partnership Initiative
STEM	scanning transmission electron microscopy
SUNY	State University of New York
T_c	critical temperature/transition temperature
TEM	transmission electron microscopy
TFA	triflouroacetate
TGA	thermogravimetric analysis
thd	tetra-methyl-heptane-dionate
UHV	ultrahigh vacuum
ULPA	ultra-low penetrating air
UTS	ultimate tensile strength
WDG	Wire Development Group
WEC	Westinghouse Electric Company
WES	Waukesha Electric Systems
XRD	X-ray diffraction
YBCO	yttrium barium copper oxide
YS	yield strength
YSZ	yttria-stabilized zirconia
Z-STEM	Z-contrast scanning transmission electron microscopy

Executive Summary

The Oak Ridge National Laboratory (ORNL) Superconducting Technology Program is conducted as part of a national effort by the U.S. Department of Energy's Office of Energy Efficiency and Renewable Energy to develop the science and technology base needed by U.S. industry for development of electric power applications of high-temperature superconductivity. The two major elements of this program are wire development and applications development. This document describes the major research and development activities for this program together with related accomplishments. The technical progress reported was summarized from recent open literature publications, presentations, and information prepared for the FY 1999 Annual Program Review held July 26–28, 1999. Aspects of ORNL's work that were presented at the International Cryogenic Materials Conference and the Cryogenic Engineering Conference (July 1999) are included in this report, as well. This ORNL program is highly leveraged by the staff and other resources of U.S. industry and universities. In fact, nearly three-fourths of the ORNL effort is devoted to cooperative projects with private companies. Interlaboratory teams are also in place on a number of industry-driven projects. Working group meetings, staff exchanges, and joint publications and presentations ensure that there *is* technology transfer with U.S. industry. Working together, the collaborative teams are making rapid progress in solving the scientific and technical issues necessary for the commercialization of long lengths of practical high-temperature superconductor wire and wire-using systems.

Highlights

WIRE DEVELOPMENT

- In an effort to develop alternative single-buffer-layer architectures for conductors coated with YBCO ($YBa_2Cu_3O_{7-y}$) , we have studied RE_2O_3 (RE = Y and rare earths) as candidate materials. Reactive electron beam evaporation was used to grow high-quality Y_2O_3, Gd_2O_3, and Yb_2O_3 buffer layers epitaxially on biaxially textured Ni (100) substrates. Using thermodynamic considerations for the formation of metal oxides, we employed both reducing atmospheres and water vapor to oxidize the film in situ to form stoichiometric RE_2O_3. Detailed X-ray studies have shown that the Y_2O_3, Gd_2O_3, and Yb_2O_3 films were grown with a single epitaxial orientation. Scanning electron microscope (SEM) micrographs indicated that ~0.5-μm-thick Y_2O_3 films on rolled-Ni substrates were dense, continuous, and crack-free. A high J_c of 1.8×10^6 A/cm^2 at 77 K and self-field was obtained on YBCO films grown on alternative buffer layers with a layer sequence of YBCO/Yb_2O_3 (sputtered)/Y_2O_3 (e-beam)/Ni. A high J_c was demonstrated on YBCO/Yb_2O_3/CeO_2/Ni and YBCO/Yb_2O_3/YSZ/CeO_2/Ni.

- A sol-gel process was developed that produced an alternative buffer-layer architecture for conductors coated with YBCO ($YBa_2Cu_3O_{7-\delta}$); Yb_2O_3 was chosen as the candidate material. Buffer layers of Yb_2O_3 were epitaxially grown on biaxially textured Ni (100) substrates by the sol-gel process for the first time. The Yb_2O_3 precursor solution was prepared from an alkoxide sol-gel route in 2-methoxyethanol and was deposited on textured-Ni (100) substrates by either spin-coating or dip-coating methods. The amorphous film was then processed at 1160ºC under a flowing Ar-H_2 (96%-4%) gas mixture for 1 h. The Yb_2O_3 film exhibited a strong *c*-axis orientation on the Ni (100) substrates. The phi and omega scans indicated good in-plane and out-of-plane orientations. The X-ray (222) pole figure showed a cube-on-cube epitaxy. High-current YBCO films were grown on the Yb_2O_3 sol-gel buffered-Ni substrates.

- We have performed a systematic study of T_c, J_c, and ρ(T) dependence on oxygen partial pressure and temperature during deposition of thin $Nd_{1+x}Ba_{2-x}Cu_3O_y$ films grown by pulsed-laser deposition. The conditions for optimal NdBCO film growth were selected by varying oxygen partial pressure from 0.02 to 400 mTorr, and substrate temperature between 730 and 800°C. Consequently, we determined the stability line in the 1/T-log[P(O_2)] phase-space for optimal synthesis of NdBCO films. The results of this study show that the best NdBCO films are obtained at oxygen pressure in the range of 0.2 to 1.2 mTorr, depending on the substrate temperature. This range is more than two orders of magnitude lower than the correspondent oxygen pressure appropriate for YBCO film growth.

- Epitaxial (Tl,Pb)-1223 films have been successfully grown on $LaAlO_3$ substrates by thermal spray followed by post-annealing in air at 870°C. The deposition rate of the current method is at least 100 times faster than those of vacuum techniques. The properties of the films are comparable with those obtained by high-vacuum deposition such as laser ablation, magnetron sputtering, and electron-beam evaporation. A transport I_c of 51 A at 77 K and zero field on a 4-mm-wide and 1.2-μm-thick cross section has been obtained, which corresponds to a J_c of 1.1×10^6 A/cm^2 at 77 K. This success provides new options and opportunities to scale up the production of superconducting coatings to large quantities and long lengths.

- We have achieved the epitaxial growth of (001)-oriented YSZ films directly on biaxially textured (001) Ni tapes using pulsed-laser deposition. The orientation of YSZ on the Ni surface depends strongly on the initial state of the substrate, with (001) epitaxy possible by nucleation on what appears to be an oxygen-terminated metal surface. The epitaxial (001) YSZ layer grown on the Ni (001) surface can be

used as a single buffer layer for a high-temperature superconducting coated conductor architecture, yielding superconducting $YBa_2Cu_3O_7$ films with high-critical-current densities.

- NdBCO epitaxial films were grown on $LaAlO_3$ and buffered Ni substrates. NdBCO films on $LaAlO_3$ showed a T_{c0} of 93 K and higher J_c than those of YBCO films in high magnetic field. NdBCO films on YSZ/CeO_2/Ni substrates showed very good texture with grain-to-grain misorientation angles of less than 3°. In these samples J_c(H=0) at 77 K was smaller (270 kA/cm^2) than the value expected from backscattered electron diffraction data, but J_c reduction in magnetic field was smaller and the irreversibility field was higher compared with those of the films on $LaAlO_3$.

- We have demonstrated that several high-quality RE_2O_3 films can be grown epitaxially with a single cube-on-cube orientation on {100}<001> textured Ni substrates by both reactive evaporation and sol-gel processing. The microstructures of RE_2O_3 buffers grown by both techniques were dense, continuous, and crack-free. The performance of the sol-gel–grown buffers approached the quality of e-beam–grown buffers. High-J_c YBCO films were grown on RE_2O_3 templates with two new buffer-layer architectures. A high J_c of 1.8 MA/cm^2 at 77 K and self-field was obtained on this YBCO/Yb_2O_3/Y_2O_3/Ni architecture. Also, a high J_c of more than 1 MA/cm^2 at 77 K and self-field was obtained on this YBCO/CeO_2/YSZ/RE_2O_3/Ni architecture.

- The solution process was used to grow epitaxial $La_2Zr_2O_7$ (LZO) buffer layers on roll-textured Ni (100) substrates for the first time to produce coated $YBa_2Cu_3O_{7-\delta}$ (YBCO) conductors. The LZO precursor solution was prepared from mixed-metal methoxyethoxides in 2-methoxyethanol by an all-alkoxide sol-gel route. The partially hydrolyzed solution was either spin-coated or dip-coated onto the textured-Ni substrates. The amorphous thin film was heat-treated at 1150°C under an Ar-H_2 (96% - 4%) atmosphere for 1 h. X-ray diffraction of the buffer layer indicated a strong *c*-axis orientation on the Ni (100) substrate. The LZO (222) pole figure revealed a single cube-on-cube texture. SEM images of the LZO buffer layer showed a dense microstructure without any cracks. The YBCO deposited on the sol-gel LZO-buffered Ni substrates with sputtered YSZ and CeO_2 top layers had a critical current density of 480 kA/cm^2 at 77 K and self-field.

- $YBa_2Cu_3O_{7-y}$ (YBCO) coated conductors that possess a high engineering current density (J_E) were fabricated on Rolling-Assisted Biaxially Textured Substrates (RABiTS™) with a layer sequence of CeO_2/YSZ/Ni. An industrially scalable ex situ BaF_2 precursor process was used. Biaxially textured Ni (100) substrates with a thickness of 50 μm were used. The YBCO films were grown on PLD-buffered CeO_2/YSZ/Ni (100) substrates by e-beam co-evaporation of Y-BaF_2-Cu precursors followed by post-annealing. As a test model, high-quality YBCO films with a J_c of more than 3.1 MA/cm^2 at 77 K and self-field were grown on CeO_2-buffered YSZ (100) single-crystal substrates. Also, high-quality YBCO films with a thickness of more than 1 mm carried a J_c of more than 1 MA/cm^2 at 77 K and self-field were grown on PLD-buffered CeO_2/YSZ/Ni (100) substrates. A high J_E of more than 28,000 A/cm^2 at 77 K was achieved for a YBCO film thickness of 1.6 mm on RABiTS™ for the first time. This result demonstrates the possibility of using both the ex situ BaF_2 precursor approach and the RABiTS™ process for producing long lengths of coated conductors.

- Equipment has been designed and is being installed to enable continuous processing, measurement, and characterization of lengths of YBCO/RABiTS™. A reel-to-reel X-ray diffraction system has been used to characterize RABiTS™ provided by CRADA partner 3M; to date, 140 m has been characterized.

SYSTEMS DEVELOPMENT

- The test program for the Southwire 5-m, single-phase, prototype cable system was successfully completed. The cable was operated simultaneously at rated voltage (7.2 kV ac line-to-ground) and rated

current (1250 A ac), experimentally proving a valid cable design. The cable was also operated without current at voltage levels up to 18 kV to verify dielectric integrity in the actual cable geometry. HTS cable ac losses were measured as a function of liquid nitrogen temperature.

- Testing of two Southwire 5-m HTS cables was completed. An extended run (27 h) at 7.2 kV ac line-to-ground and at 1250 A (rms) was completed. AC losses were measured for both cables as a function of operating temperature and current. The first 30-m SPI cable exceeds the design rating for critical current by a factor of 2.
- The Southwire SPI 30-m high-temperature superconducting cable system was fully assembled and was undergoing testing in Carrollton, Georgia in October 1999.
- The new second-generation termination design for the Southwire Superconductivity Partnership Initiative (SPI) cable project has passed all qualification tests in the 5-m cable facility.
- The 1-MVA Waukesha demonstration transformer was untanked and completely inspected to determine the cause of the high-voltage tripoff that occurred last year. No damage to any of the coils, instrumentation leads, or the electrical insulation system was found. Instead, damage to aluminized mylar superinsulation blankets on the outside of the liquid nitrogen shield was observed. This could have been caused by eddy currents induced in the superinsulation. The transformer was successfully retested in air to full open-circuit operating voltage of 13.8 kV.
- Sixty-cycle ac and negative-polarity impulse tests have been made on fiber-reinforced plastic (FRP) disks and tubes. The breakdown strength is lowered considerably from that of a pure vacuum gap. Lowering the temperature of FRP has little effect on the surface flashover strength and, if anything, tends to lower the strength slightly. The use of FRP as spacer material in low- temperature vacuum applications is not clearly understood based on the present data, suggesting that additional work is needed.

PROGRAMMATIC

- RABiTS™ won a 1999 R&D 100 Award. The award is given to the top 100 innovations for the year as determined by the editors of *R&D Magazine*. Details are available on the Web at (http://www.rdmag.com/rd100/99_rd100_ornl.htm#rab).
- Amit Goyal was named in the TR100, published in the Massachusetts Institute of Technology's *Technology Review* magazine. Described as "the most remarkable group of innovators under 35 ever assembled," the TR100 can be found on the Web at http://www.techreview.com/tr100/profiles.html.

1. Technical Progress in Wire Development

1.1 GROWTH OF BIAXIALLY TEXTURED RE_2O_3 BUFFER LAYERS ON ROLLED-Ni SUBSTRATES USING REACTIVE EVAPORATION FOR HTS COATED CONDUCTORS

M. Paranthaman, D. F. Lee, A. Goyal, E. D. Specht, P. M. Martin, X. Cui, J. E. Mathis, R. Feenstra, D. K. Christen, and D. M. Kroeger

For the fabrication of $YBa_2Cu_3O_{7-y}$ (YBCO) coated conductors on metal substrates, the Rolling-Assisted Biaxially Textured Substrate (RABiTS™) approach developed earlier by us has emerged as one of the leading techniques. In this approach, the cube texture in the starting Ni (100) substrates was obtained by cold-rolling of Ni rods followed by recrystallization. The buffer layers and the YBCO superconductors were then grown epitaxially on the textured-Ni (100) substrates. During the initial demonstration of the RABiTS™ approach, high-J_c YBCO films were grown with a layer sequence of YBCO/YSZ/CeO_2/Ni substrates; both buffer layers and YBCO superconductors were grown by pulsed laser deposition (PLD). Following this work, scalable techniques like electron-beam (e-beam) evaporation and sputtering were used to produce high-quality CeO_2 and YSZ buffer layers. High-current YBCO films were also grown on both all-e-beam and e-beam/sputtered buffer layers. Recently, we have demonstrated that high-J_c YBCO films can be grown by an ex situ BaF_2 precursor approach on RABiTS™ with a layer sequence of YBCO/ CeO_2/YSZ/CeO_2/Ni. The formation of cracks in CeO_2 films with ≥2000-Å thickness on Ni (100) substrates has prevented us from utilization of CeO_2 as a single buffer layer. There is a clear need to develop an alternative buffer layer architecture to simplify the wire development process and possibly to use a single buffer layer to fabricate high-current coated conductors. In this section, we report our successful demonstration of using reactive evaporation to grow epitaxial RE_2O_3 (RE = Y and rare earths) buffer layers on rolled-Ni substrates.

1.1.1 Structural Aspects and Free Energy of RE_2O_3 Formation

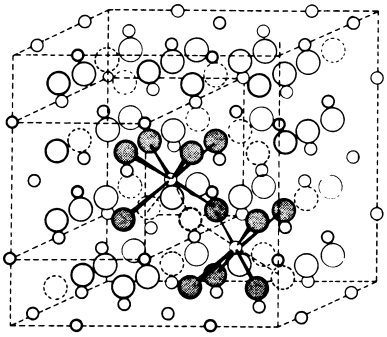

Fig. 1.1. Crystal structure of Y_2O_3.

The crystal structure of Y_2O_3 is shown in Fig. 1.1. This structure is similar to fluorite (CaF_2) structure, where one-fourth of the oxygen ions (shown as dotted circles in Fig 1.1) are removed in order to maintain the charge neutrality between Y^{3+} and O^{2-}. In Fig 1.1, large open circles indicate oxygen, large dotted circles indicate oxygen vacancies, and small circles indicate yttrium ions. The two kinds of 6-coordination groups of yttrium metal ions shown in Fig. 1.1 can be simply described as distorted octahedra. Cubic lattice parameters for Y_2O_3 and RE_2O_3 are reported in Table 1.1. The cubic lattice parameter for Y_2O_3 is 10.604 Å, but the pseudocubic lattice parameter (half of the diagonal of face-centered cubic lattice parameter) is 3.75 Å. This provides a close lattice match (1.89% mismatch) with YBCO. Among the rare earth oxides, Gd_2O_3 has the best lattice match (0.07% mismatch) with YBCO. The calculated lattice misfit data for RE_2O_3 with both YBCO and Ni substrates are also given in Table 1.1. The lattice mismatch was calculated from the following equation: lattice mismatch = 2(a−b)/(a+b). Due to lanthanide contraction, the ionic radii of the 4f metals decrease with increasing atomic number; hence, the lattice

Table 1.1. Structure and the lattice misfit data for RE_2O_3

RE_2O_3	Structure type		% lattice mismatch	
	Cubic lattice parameter a (Å)	pseudocubic a/2√2 (Å)	vs YBCO	vs Ni
Y_2O_3	10.604	3.750	1.89	6.22
La_2O_3	11.327	4.005	4.69	12.78
Nd_2O_3	11.080	3.918	2.50	10.59
Sm_2O_3	10.927	3.864	1.11	9.21
Eu_2O_3	10.868	3.843	0.54	8.64
Gd_2O_3	10.813	3.824	0.07	8.17
Tb_2O_3	10.730	3.794	0.72	7.39
Dy_2O_3	10.665	3.771	1.33	6.78
Ho_2O_3	10.606	3.750	1.89	6.22
Er_2O_3	10.548	3.730	2.42	5.69
Tm_2O_3	10.487	3.708	3.01	5.09
Yb_2O_3	10.436	3.690	−3.50	4.61
Lu_2O_3	10.390	3.674	−3.93	4.17

parameter of RE_2O_3 decreases when passing from La_2O_3 to Lu_2O_3. Using Table 1.1, one can see that the lattice parameters can be tailored to match that of the substrate or the high-temperature superconducting (HTS) film. Depending upon the coordination number for the rare earth element, other structures are also possible. For Y_2O_3, the thermal expansion coefficient is about 7.7×10^{-6}/ºC, which is comparable to that of YBCO (about 11×10^{-6}/ºC).

Figure 1.2 shows plots of $\Delta G_f°$ for the oxidation of selected metals taken from heats of formation and standard entropy tables. From Fig. 1.2, it can be clearly seen that by using H_2O as the oxidizing agent, one can selectively oxidize Ce, Gd, Y, and other rare earth metals over Ni. The oxidation thermodynamics of Ni metal substrates during the deposition of oxide buffer layers is reported in detail by Jackson et al.[1]

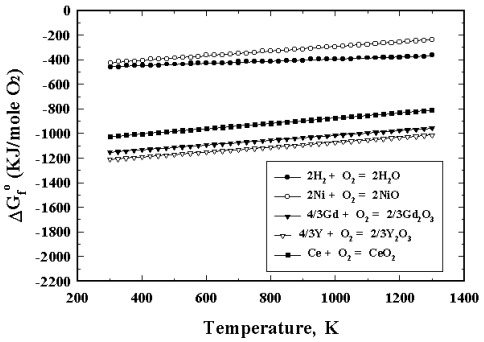

Fig 1.2. The standard free energy for the selected rare earth oxides. The data are compared with the formation of NiO and water.

1.1.2 Experimental Procedure

An e-beam evaporation technique was used to deposit RE_2O_3 films directly on Ni. The as-rolled Ni substrates were cleaned ultrasonically with both acetone and methanol and were recrystallized to the desired {100}<001> cube texture by annealing the substrates at 800ºC for 2 h in a vacuum of

10^{-6} Torr. Biaxially oriented Ni substrates were mounted on a substrate holder with a heater assembly in the e-beam system. After the vacuum in the chamber had reached 1×10^{-6} Torr at room temperature, a gas mixture of 4% H_2 and 96% Ar was introduced until the pressure inside the chamber reached 1 Torr. The Ni substrates were annealed at 650°C for 1 h at that pressure. The chamber was then pumped and maintained at a pressure of 2×10^{-5} Torr using a mixture of 4% H_2 and 96% Ar. The gas flow was controlled by a dc-powered piezoelectric valve. The Y_2O_3, Gd_2O_3, and Yb_2O_3 layers were grown on the Ni substrates at temperatures around 650°C. The crucibles used were either tungsten or graphite. Yttrium, gadolinium, and ytterbium metals were used as the source for the respective oxide growth.

A Dycor Quadruple Gas Analyzer mounted in the e-beam system was used to analyze the chemistry of the oxide formation. The background H_2O pressure was around 1×10^{-5} Torr. The deposition rate for RE_2O_3 was 2–5 Å/s with the operating pressure of 10^{-5} Torr, and the final thickness was varied from 200 to 5000 Å. During the initial deposition, the H_2O pressure slowly decreased to 2×10^{-6} Torr. Then, H_2O was introduced into the chamber, and the H_2O pressure was maintained at 1×10^{-5} Torr. The H_2O pressure in the chamber was sufficient to oxidize the film to form stoichiometric RE_2O_3. The measured partial pressure of O_2 during deposition was in the range of 10^{-8} Torr. Similar conditions were used earlier to grow CeO_2 films using Ce metal as the source. The radio-frequency (rf) magnetron sputtering technique was used to grow Yb_2O_3 on e-beam-grown Y_2O_3-buffered Ni substrates at 780°C. The experimental details of this film growth will be published elsewhere. The PLD technique was used to grow YBCO at 780°C and 185 mTorr O_2 on sputtered Yb_2O_3 layers.

The films were analyzed by X-ray diffraction (XRD). A Philips Model XRG3100 diffractometer with Cu Kα radiation was used to record powder diffraction patterns. For texture analysis, a Rigaku rotating-anode X-ray generator was used; a graphite monochromator selected Cu Kα radiation, and slits defined a 2×2 mm^2 incident beam. A four-circle diffractometer was used to collect pole figures, ω scans, and ϕ scans. SEM micrographs were taken using a Hitachi S-4100 Field Emission Scanning Electron Microscope. The beam voltage used was 15 kV. The thickness of the films was determined both by Rutherford Backscattering Spectroscopy (RBS) and Alpha Step Profilometer scans. The electron backscatter Kikuchi diffraction (BKD) patterns were obtained on RE_2O_3 layers. The experimental details were published earlier.

1.1.3 Results and Discussion

A typical θ-2θ scan for a 3000-Å- thick Y_2O_3 film on a textured-Ni (100) substrate is shown in Fig. 1.3. The strong Y_2O_3 (400) from Fig. 1.3 revealed the presence of a good out-of-plane texture. Figure 1.4 shows ω and ϕ scans for as-grown 800-Å-thick Y_2O_3 on a textured-Ni (100) substrate. The film was grown at 650°C. The full-width-at-half-maximum (FWHM) values for Ni (002) and Y_2O_3 (004) peaks are 7.2° and 7.1°, and that of Ni (202) and Y_2O_3 (222) are 11.7° and 8.4°, respectively.

A typical Y_2O_3 (222) pole figure for 800-Å-thick Y_2O_3 films grown at 650°C on textured-Ni (100) is shown in Fig. 1.5(*a*). Out-of-plane and in-plane texture data for 3000-Å-thick Y_2O_3 film on Ni (100) substrate are reported in Table 1.2. From the XRD results, it can be concluded that Y_2O_3 can

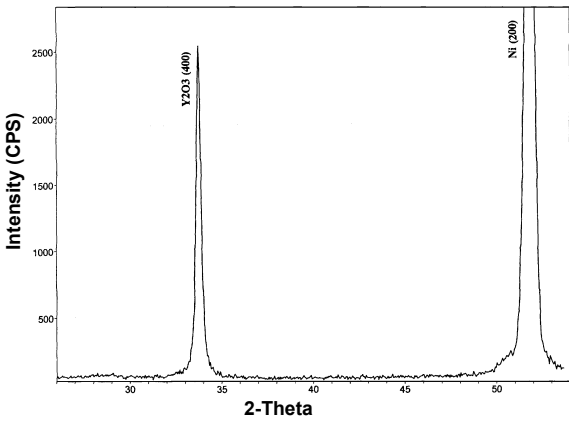

Fig. 1.3. A typical θ-2θ scan for a 3000-Å-thick Y_2O_3 film on Ni (100) substrates.

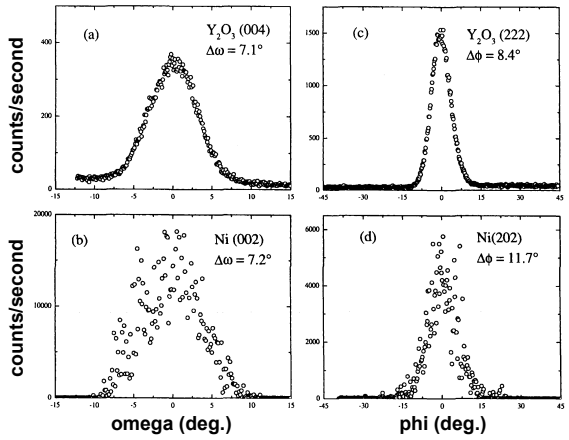

Fig. 1.4. The ω and ϕ scans for an 800-Å-thick Y_2O_3 film on Ni (100) substrates.

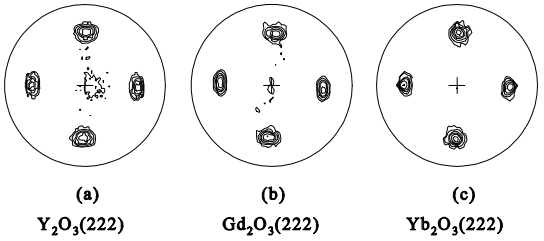

Fig. 1.5. (222) X-ray pole figures of (*a*) Y_2O_3, (*b*) Gd_2O_3, and (*c*) Yb_2O_3. Logarithmic contour levels are 1, 2, 5, 10, 20, and 40 times random texture.

be grown epitaxially on {100}<001> Ni substrates. Out-of-plane and in-plane texture data for 900-Å-thick Gd_2O_3 and Yb_2O_3 films grown on textured-Ni substrates are reported in Table 1.2. The FWHM values of the in-plane texture of both Gd_2O_3 and Yb_2O_3 were similar to that of the Ni substrates. Typical Gd_2O_3 (222) and Yb_2O_3 (222) pole figures for 900-Å-thick Gd_2O_3 and Yb_2O_3 films on textured-Ni substrates are shown in Fig. 1.5 (*b*) and (*c*). From these XRD results, it can be concluded that Gd_2O_3 and Yb_2O_3 can also be grown epitaxially on {100}<001> Ni substrates. Using similar conditions, one should be able to grow other rare earth oxides on Ni (100) substrates.

Table 1.2. Texture analysis data on RE_2O_3 films on rolled-Ni substrates

Sample	Thickness QCM (Å)	Out-of-plane epitaxy, FWHM (deg.)		In-plane epitaxy, FWHM (deg.)	
		RE_2O_3 (004)	Ni (002)	RE_2O_3 (222)	Ni (111)
Y_2O_3/Ni	3000	6.3	7.1	10.3	10.7
Y_2O_3/Ni	800	7.1	7.2	8.4	11.7
Gd_2O_3/Ni	900	5.2	7.1	9.2	10.1
Yb_2O_3/Ni	900	6.4	7.3	8.8	8.7

Typical RBS spectra for 500-Å-thick Yb_2O_3 film grown on a Ni (100) substrate are shown in Fig. 1.6. Similar thickness values were obtained using the profilometer scans. We have used these thickness values to calibrate the quartz crystal monitor in the e-beam system. An SEM micrograph for a 3000-Å-thick Y_2O_3 film on Ni (100) substrate is shown in Fig. 1.7. As can be seen from the SEM micrograph, the Y_2O_3 films grown were dense, crack-free, and continuous. However, the e-beam-grown Gd_2O_3 and Yb_2O_3 films had a porous but crack-free microstructure. Efforts are being made to obtain dense films.

Orientation-image micrographs of a ~0.5-μm-thick Y_2O_3 film grown on a Ni (100) substrate are shown in Fig. 1.8. Figure 1.8(*a*) is the image of the sample created solely from diffraction data. Data were obtained on a hexagonal grid at a spacing of 0.9 μm. Indexing of the pattern at each location gave a unique measure of the orientation at that point. A hypothetical hexagonal lattice with a lattice parameter of 0.9 μm was superimposed at each point from which a pattern was obtained, and resulting grain boundary

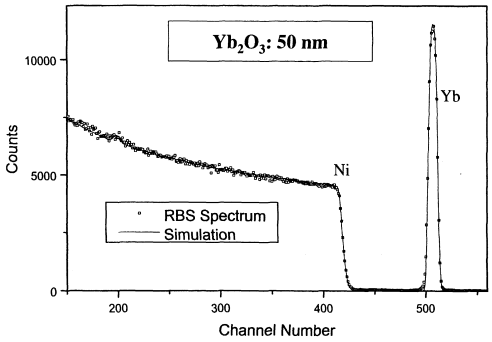

Fig. 1.6. Rutherford backscattering spectra of Yb_2O_3 on Ni (100) substrates. The spectra were measured with 2.0-MeV He^{2+} ions at near-normal incidence, detected at a 160° scattering angle.

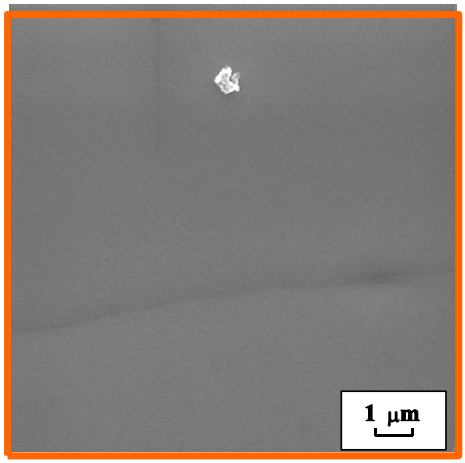

Fig. 1.7. SEM micrograph for a 3000-Å-thick Y_2O_3 film on Ni (100) substrate, indicating the presence of a crack-free and smooth microstructure.

misorientations were then calculated. In order to visualize the percolative path in Y_2O_3 film, grains in Figs. 1.8(*b*) and 1.8(*c*) were color-coded according to the criterion that a single color represents a percolative region of orientation change less than 2° and 5°. It can be seen that most of the film is percolatively connected within 5°. Figure 1.9 shows (100), (111), and (110) pole figures derived from the region shown in Fig. 1.8(*a*). A sharp cube texture is evident.

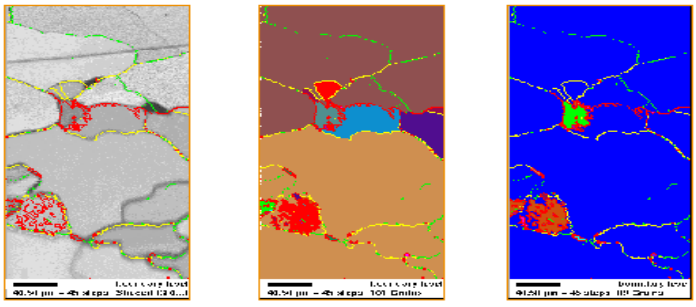

Fig. 1.8. (*a*) Orientation image micrograph from a 5000-Å-thick film on Ni (100) substrate. BKD patterns were obtained in a hexagonal grid with a step of 0.9 μm. Variations in intensity are a reflection of pattern quality or intensity of the Kikuchi bands. Three types of green boundaries denote boundaries with misorientations greater than 1° and less than 5°, yellow lines denote boundaries with misorientations greater than 5° and less than 10°, and red boundaries with misorientations greater than 10°. The orientation image micrographs (*a*) were colored with the criterion that a given color represents a percolative region with in (*b*) 2° and (*c*) 5°. Clearly most of the substrate is well connected by boundaries less than 5° .

During the course of our work, we have learned that Ichinose et al.[2,3] have independently succeeded in growing Y_2O_3 buffer layers on textured-Ni (100) substrates using reactive evaporation. They have grown Y_2O_3 layers at higher temperatures (940°C) in N_2 at a pressure of 5×10^{-4} Torr. The reported microstructure and the in-plane texture measurements on Y_2O_3 layers grown by Ichinose et al. were similar to the results obtained in our work, but so far they have not demonstrated the growth of high-J_c YBCO films on their buffers. We have used a different chemistry for Y_2O_3 and RE_2O_3 film growth on textured-Ni (100) substrates. We have also grown RE_2O_3 buffers at much lower temperatures (650°C) and under partial pressures of H_2/H_2O.

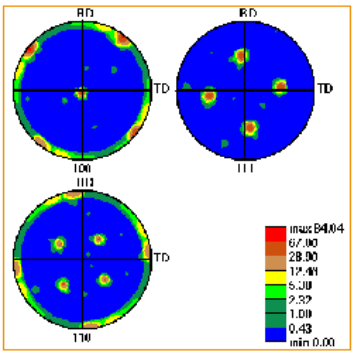

Fig. 1.9. The (100) and (111) and (110) pole figures of the orientations observed for a 5000-Å-thick Y_2O_3 film on Ni (100) substrate in Fig. 1.8. A single orientation of the Y_2O_3 film, rotated 45° with respect to the {100} <100> oriented Ni substrate, is observed.

1.1.4 Conclusions

We have demonstrated that Y_2O_3, Gd_2O_3, and Yb_2O_3 films can be grown epitaxially with a single cube-on-cube orientation on rolled-Ni (100) substrates using reactive evaporation. Using H_2O as the oxygen source, we produced stoichiometric RE_2O_3 films in situ on Ni {100}<001> substrates without the formation of NiO at the substrate-film interface. The microstructure of the e-beam-grown ~0.5-μm-thick Y_2O_3 films was dense, crack-free, and continuous. Both Gd_2O_3 and Yb_2O_3 films grown so far were crack-free but porous. Efforts are being made to produce dense films. The lattice mismatch between YBCO and Gd_2O_3 is small compared with that for YBCO and other rare earth oxides. Our preliminary results are discussed in the next section.

1.1.5 References

1. T. J. Jackson, B. A. Glowacki, and J. E. Evetts, "Oxidation Thermodynamics of Metal Substrates During the Deposition of Buffer Layer Oxides," *Physica C* **296**(3&4), 215–24 (1998).

2. A. Ichinose et al., "Deposition of Y_2O_3 Buffer Layers on Biaxially-Textured Metal Substrates," *Physica C* **302**(1), 51–56 (1998).

3. A. Ichinose et al. "Preparation and Characterization of Y_2O_3 Buffer Layers and YBCO Films on Textured Ni Tape," pp. 2280–83 in *IEEE Trans. on Appl. Supercond.*, Vol. 9, No. 2, June 1999, Superconductivity Conference, Palm Desert, Calif., 1998.

1.2 EPITAXIAL GROWTH OF Yb_2O_3 BUFFER LAYERS ON BIAXIALLY TEXTURED-Ni (100) SUBSTRATES BY SOL-GEL PROCESS

T. G. Chirayil, M. Paranthaman, D. B. Beach, J. S. Morrell, E. Y. Sun, A. Goyal, R. K. Williams, D. F. Lee, P. M. Martin, D. M. Kroeger, R. Feenstra, D. T. Verebelyi, and D. K. Christen

1.2.1 Introduction

The RABiTS™ approach, developed at the Oak Ridge National Laboratory (ORNL), has emerged as one of the leading techniques for the fabrication of the $YBa_2Cu_3O_{7-\delta}$ (YBCO) coated conductors being used in the development of superconducting wires for high-temperature, high-field applications. The process involves obtaining cube-textured Ni (100) substrates by cold-rolling Ni rods followed by recrystallization. The buffer layers are epitaxially grown on the textured metal substrates, and then in-plane-oriented superconducting films are deposited. Critical current densities of YBCO films of more than 1 MA/cm^2 at 77 K have been demonstrated on rare earth oxide (RE_2O_3) buffer layers with various architectures produced via the vacuum process. The goal of this research is to develop the RABiTS™ process using a nonvacuum approach such as the sol-gel or the metal organic decomposition (MOD) processes.

The nonvacuum approach has many advantages. The techniques are very cost-effective and easily scalable. The solution process gives better homogeneity and composition control because the precursors are mixed at atomic levels. Substrates with various shapes and forms can be coated with ease by the spin-coating or dip-coating methods.

Morell et al.[1] at ORNL recently demonstrated the epitaxial growth of a rare earth oxide, Gd_2O_3, buffer layer on textured-Ni (100) substrate by sol-gel process for the first time. Previously, buffer layers prepared

by the sol-gel technique showed epitaxial growth on single-crystal substrates in multiple orientations on textured-Ni (100) substrates. The Gd_2O_3 precursor solution was prepared via an all-alkoxide sol-gel route. The textured film had a continuous and a dense microstructure and no cracks.

In this report, the preparation of the Yb_2O_3 precursor solution, film deposition, and characterization of the sol-gel buffer layer on textured-Ni (100) substrate is described for the first time. We also demonstrate the deposition of a high-J_c YBCO film on a sol-gel-grown buffer layer with two sputtered cap layers: YSZ and CeO_2.

1.2.2 Experimental

The solution preparation was carried out under an Ar atmosphere using a Schlenck-type apparatus. The isopropanol was dried by distillation from aluminum isopropoxide. The ytterbium ingot and 2-methoxy-ethanol (Alfa) were used without further purification. The flow chart for the ytterbium precursor preparation is shown in Fig. 1.10. The first step involved the preparation of ytterbium isopropoxide from ytterbium metal, which was achieved by reacting ytterbium metal filings with dry isopropanol in the presence of a mercuric catalyst. The ytterbium isopropoxide was extracted using a Soxhlet extractor with isopropanol, and was recrystallized to obtain a highly pure final product.

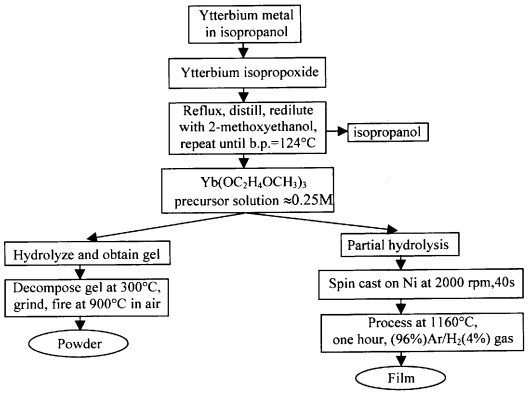

Fig. 1.10. Flow chart for Yb_2O_3 precursor solution preparation.

The second step involved the exchange of the isopropoxide ligand for a methoxyethoxide ligand. About 1.66 g (6.25 mmoles) of ytterbium isopropoxide were weighed out in a 200-mL round bottom flask and dissolved in 50 ml of 2-methoxyethanol. After the solution was refluxed for one hour, approximately 30 ml of the isopropanol and 2-methoxyethanol solvent mixture was removed by distillation. The solution was rediluted with 2-methoxyethanol and was distilled repeatedly to ensure complete ligand exchange. Finally, the volume of the solution was adjusted with 2-methoxyethanol to 25 ml to make a 0.25 M Yb_2O_3 precursor solution.

The precursor solution was partially hydrolyzed by adding approximately one part of 1.0 M water in 2-methoxyethanol to four parts of the stock solution. The solution was allowed to age overnight at room temperature prior to coating. Part of the solution was fully hydrolyzed to obtain gels. The gels were dried on a hot plate and then were fired at 900°C in air for 1 h to obtain the powder for phase identification.

The Yb_2O_3 precursor solution was spin-coated onto textured-Ni substrates. The (100) cube-textured-Ni substrates were prepared by annealing the cold-rolled Ni substrates to recrystallization at 900°C for 2 h under vacuum. The Ni substrates were cleaned ultrasonically in isopropanol for 1 h prior to coating. The coatings were applied with a spin coater operated at 2000 rpm for 40 s. The samples were annealed in a preheated oven at 1160°C for 1 h under flowing gas (96% Ar/4% H_2) and then quenched to room temperature.

The Yb_2O_3 films were characterized in detail by X-ray diffraction. Powder diffraction patterns were obtained with a Philips XRG3100 diffractometer with Cu Kα radiation. A Picker four-circle diffractometer was used to determine the texture of the film. The out-of-plane alignment (ω scans) was measured by scanning the (400) planes of the film. The in-plane alignment (ϕ scans) was determined by measuring the Yb_2O_3 (222) planes. The Yb_2O_3 (222) pole figure was also collected to determine whether the film had a single-cube epitaxy. The microstructure of the Yb_2O_3 films was analyzed using a Hitachi S-4100 field-

emission SEM. The beam voltage used was 5 kV. The thickness of the film was determined with an Alpha-Step 500 (Tencor Instruments) profilometer.

1.2.3 Results and Discussion

1.2.3.1 Yb_2O_3 Buffer Layer Characterization

The XRD pattern of the ytterbium precursor powder fired at 900°C revealed a pure Yb_2O_3 phase. The pseudocubic Yb_2O_3 phase can be indexed with a lattice parameter of 3.69 Å. The lattice mismatch of Yb_2O_3 with YBCO is –3.50%.

The Yb_2O_3 thin film after annealing displayed a golden color. The film thickness of a single coat was determined to be ~1500 Å. The θ-2θ scan of the Yb_2O_3 film (Fig. 1.11) showed a strong peak at 34.5° 2θ from the Yb_2O_3 (400) reflection and a very weak peak at 2 of 29.5° from the Yb_2O_3 (222) reflection. This indicated a good out-of-plane alignment of the Yb_2O_3 film on the Ni(100) substrate. Figure 1.12 shows the ϕ and ω scans of Yb_2O_3 film on textured-Ni (100) substrate. The FWHM values of Yb_2O_3 (400) and Ni (200) omega scans were 9.89° and 7.06°, respectively.

The FWHM values of the ϕ scans were 10.11° for Yb_2O_3 (222) plane and 8.45° for Ni (111) plane. The pole figure (Fig. 1.13) of the Yb_2O_3 sol-gel buffer layer on textured-Ni (100) substrate had predominantly a single-cube epitaxy. From the ϕ scans and the pole figure, we can conclude that the Yb_2O_3 film exhibits a biaxial alignment on the Ni (100) substrate.

The SEM micrograph of the Yb_2O_3 film, shown in Fig. 1.14, was taken at a magnification of 20 k×. The microstructure showed a dense, continuous and a crack-free Yb_2O_3 film on the Ni substrate.

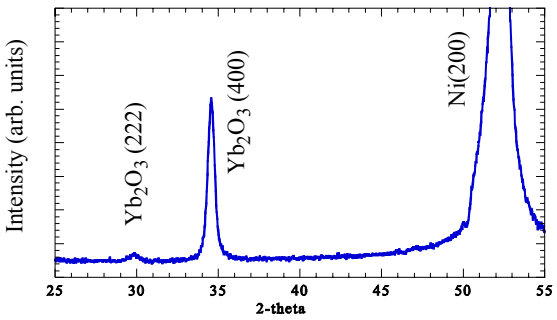

Fig. 1.11. The θ-2θ scan of the Yb_2O_3 film on Ni (100) substrate shows a strong *c*-axis orientation.

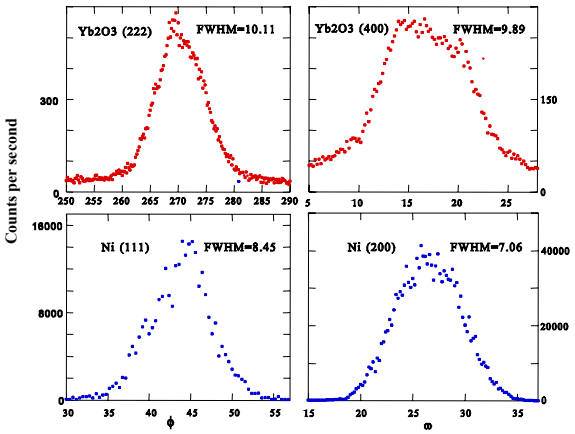

Fig. 1.12. The phi and omega scans of Yb_2O_3 film and Ni (100) substrate.

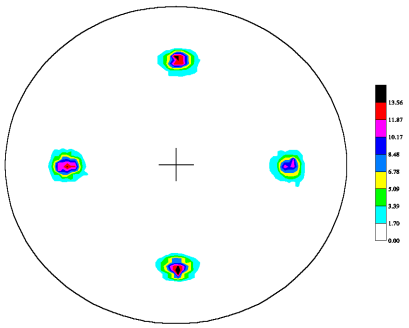

Fig. 1.13. Pole figure of the sol-gel grown Yb_2O_3 film shows a single-cube epitaxy on textured-Ni (100) substrate.

1.2.3.2 YBCO Deposition

With a Yb_2O_3 sol-gel buffer layer as the initial layer, YSZ and CeO_2 cap layers were epitaxially grown by sputtering. The YBCO precursor was then deposited on the CeO_2 by e-beam deposition of BaF_2, yttrium metal, and copper metal and subsequently was annealed in an $H_2O/O_2/Ar$ atmosphere. The RABiTS™ architecture and the temperature-dependent resistivity measurement are shown in Fig. 1.15. The YBCO film had a room-temperature resistivity of 380 μΩ-cm and zero resistance at 90 K. The transport J_c of the YBCO film was

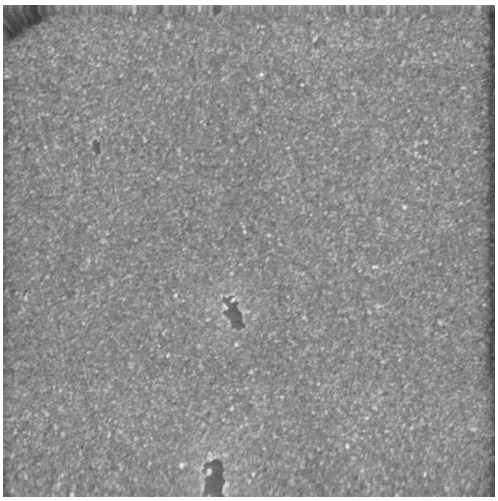

Fig. 1.14. SEM micrograph shows a dense, continuous, and a crack-free Yb_2O_3 film.

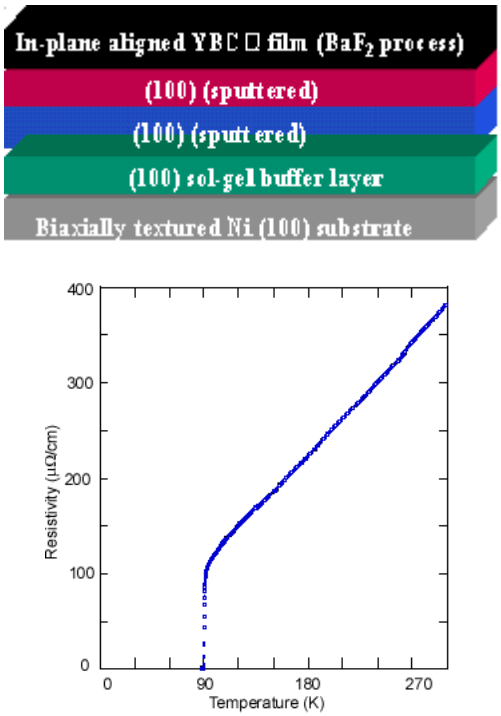

Fig. 1.15. RABiTS™ architecture with Yb_2O_3 sol-gel initial layer (top) and the resistivity curve (bottom).

4.2×10^5 A/cm^2 at 77 K and zero magnetic field. The J_c value decreased to 0.7×10^5 A/cm^2 when a perpendicular magnetic field of 0.5 T was applied.

1.2.4 Conclusions

We have demonstrated the epitaxial growth of Yb_2O_3 buffer layer on textured-Ni (100) substrates by the sol-gel process for the first time. X-ray analysis of the buffer layer indicated good in-plane and out-of-plane alignments. The pole figure of the Yb_2O_3 film showed predominantly a single-cube texture on Ni. The film was dense, continuous, and crack-free. A reasonably high J_c of 4.2×10^5 A/cm^2 at 77 K and zero field was demonstrated on the RABiTS™ architecture: YBCO(BaF_2 process)/CeO_2(sputtered)/YSZ(sputtered)/Yb_2O_3(sol-gel)/Ni. Future research is directed toward depositing epitaxial sol-gel buffer layers and in-plane superconducting films using only a nonvacuum approach.

1.2.5 References

1. J. S. Morrell et al., "Epitaxial Growth of Gadolinium Oxide on Roll-Textured Nickel Using a Solution Growth Technique," *J. Mater. Res.* **15**(93), 621 (2000).

1.3 DEMONSTRATION OF HIGH-CURRENT-DENSITY YBCO-COATED CONDUCTORS ON RE_2O_3- BUFFERED Ni SUBSTRATES WITH TWO NEW ALTERNATIVE ARCHITECTURES

M. Paranthaman, R. Feenstra, D. F. Lee, D. B. Beach, J. S. Morrell, T. G. Chirayil, A. Goyal, X. Cui, D. T. Verebelyi, J. E. Mathis, P. M. Martin, D. P. Norton, E. D. Specht, D. K. Christen, and D. M. Kroeger

To develop single buffer layer architectures, we have studied RE_2O_3 (RE = Y and rare earths) as candidate materials. Three types of crystal structures are known for the rare earth oxides. They are hexagonal (type A), monoclinic (type B), and cubic (type C). Type A has a space group of p3m1 and

contains one molecule per unit cell. Each trivalent cation is bonded to seven oxygen atoms (four short bonds and three long bonds), while the two types of oxygen atoms are bonded to five and four metal atoms, respectively. Type B has a space group of C2/m, contains six molecules per unit cell, and also shows sevenfold cation coordination. The crystal lattice has three different cation sites and five different anion sites that bond to four, five, or six metal atoms. Type C has a space group of Ia3 with 16 molecules per unit cell. It is derived from the fluorite (CaF_2) structure by doubling the lattice parameter and by removing one-fourth of the oxygen ions to maintain the charge neutrality between Y^{3+} and O^{2-}. The crystal lattice has two kinds of sixfold coordinated yttrium ions. Stability relationships for these three structure types for RE_2O_3 are shown in Fig. 1.16. The A:B phase boundary line is vertical and independent of temperature; it lies between neodymium and samarium. The B:C phase boundary is fairly well understood; further extension of the line to higher temperatures is prevented by fusion of the rare earth oxides. Thus, Y_2O_3 and the five heaviest rare earth oxides (namely Ho_2O_3, Er_2O_3, Tm_2O_3, Yb_2O_3, and Lu_2O_3) exist in only the cubic form at ambient pressures. Also, the B:C phase boundary is completely reversible for pure Dy_2O_3, Tb_2O_3, and Gd_2O_3, and for Eu_2O_3, and Sm_2O_3 in the presence of water as a catalyst. The exact locations of these phase boundaries for RE_2O_3 films are under further investigation. The cubic lattice parameters for RE_2O_3 were reported earlier.[1] The lattice parameters can be tailored by choosing the appropriate RE_2O_3 (with one or more rare earths) to match those of the substrate or the HTS film. Recently, we reported our initial demonstration of the growth of epitaxial RE_2O_3 buffer layers on textured Ni substrates using both reactive evaporation and sol-gel alkoxide routes.[1,2] Here, we report our successful demonstration of RE_2O_3 growth of high-current YBCO films on RE_2O_3-buffered Ni substrates with two new alternative buffer layer architectures.

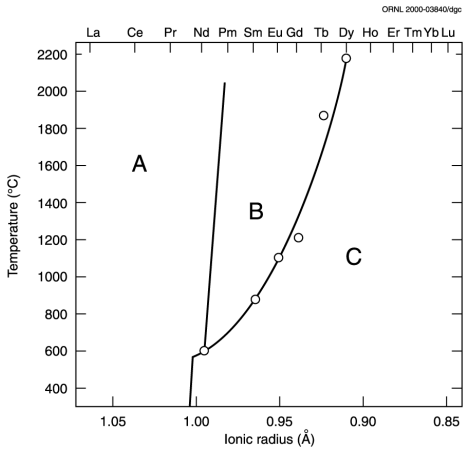

Fig. 1.16. Structural stability relationships for RE_2O_3. The symbol "A" represents the hexagonal structure, "B" represents the monoclinic structure, and "C" represents the cubic structure. [Source: Henry R. Hoekstra, *Inorg. Chem.* 5, 755 (1966) and sources therein.]

1.3.1 Experimental Procedure

An e-beam evaporation technique was used to deposit RE_2O_3 films directly on Ni. Using thermodynamic considerations for the formation of metal oxides, we employed both reducing atmospheres (mixture of 4% H_2 and 96% Ar) and water vapor to oxidize the film in situ to form stoichiometric RE_2O_3. The Y_2O_3, Gd_2O_3, and Yb_2O_3 films were grown on textured Ni substrates at temperatures around 650°C. Similarly, Gd_2O_3, Yb_2O_3, and Eu_2O_3 films were grown on textured Ni substrates using sol-gel alkoxide precursors. (The sol-gel chemistry and details of the solution preparations will be reported elsewhere.) The coating solution was typically 0.25–0.5 M rare earth methoxyethoxide in 2-methoxyethanol. The coating was done either by spin-coating at 2000 rpm for 45 s or by linear dip-coating, in which the Ni strip was immersed in the precursor solution and then withdrawn at a rate of 3 cm/min. After coating, the Ni substrates were annealed in a mixture of 4% H_2 and 96% Ar (forming gas) at temperatures ranging from 1050 to 1150°C for 1 h and were then quenched to room temperature.

The rf magnetron sputtering technique was used to grow Yb_2O_3 on e-beam-grown Y_2O_3-buffered Ni substrates at 780°C. Similarly YSZ and CeO_2 cap layers were grown on RE_2O_3-buffered Ni substrates at 780°C using rf magnetron sputtering. The plasma power was 75 W at 13.56 MHz. The resulting Yb_2O_3, YSZ, and CeO_2 films were smooth and dense. Pulsed laser deposition was used to grow YBCO at 780°C

and in 200 mTorr O_2 on sputtered Yb_2O_3 layers. Precursor YBCO films were grown on CeO_2-buffered YSZ/RE_2O_3 (sol-gel/e-beam)/Ni substrates by e-beam co-evaporation of Y, BaF_2, and Cu at a combined deposition rate of ~6 Å/s.

1.3.2 Results

Reactive evaporation was used to grow high-quality Y_2O_3, Gd_2O_3, and Yb_2O_3 films with a single-cube texture directly on {100}<001> textured-Ni substrates. Similarly, a nonvacuum process was used to grow high-quality Gd_2O_3, Yb_2O_3, and Eu_2O_3 films with a single-cube texture directly on {100}<001> textured-Ni substrates. Detailed microstructure studies indicate that these RE_2O_3 buffers were dense, continuous, and crack-free. A 300-nm-thick superconducting YBCO film deposited onto the Yb_2O_3 (sputtered)/Y_2O_3 (e-beam)/Ni by PLD had a J_c of 1.8 MA/cm^2 at 77 K and self-field. This demonstration of high-current YBCO films on these RE_2O_3-buffered Ni substrates indicates that RE_2O_3 buffers are an excellent diffusion barrier for Ni.[3]

High-J_c, 300-nm-thick YBCO films were also grown onto the CeO_2 (sputtered)/YSZ (sputtered)/Yb_2O_3 (e-beam) or Eu_2O_3 (dip-coated)/Ni by the ex situ BaF_2 precursor process. The θ-2θ scans of these YBCO films indicated the presence of a *c*-axis-aligned film. A small impurity peak at ~ 28.7°, which may be indexed as belonging to $BaCeO_3$, indicates that there is some interaction between the CeO_2 layer and YBCO. Typically for high-J_c YBCO films, this $BaCeO_3$ impurity is almost suppressed. A small amount of NiO impurity was also observed in the film. Detailed pole figure analysis indicated the presence of a single-cube texture for Yb_2O_3 (e-beam) and Eu_2O_3 (sol-gel) layers.

The room-temperature resistivity of the 300-nm-thick YBCO film on CeO_2/YSZ/Yb_2O_3 (e-beam) was around 260 μΩ–cm and the T_c measured was about 90 K. Extrapolating values of the resistivity (between 300 K and above T_c) to below zero indicates the presence of predominantly c⊥ YBCO film. The field dependence of J_c for the same film is shown in Fig. 1.17. The zero-field J_c measured was around 1 MA/cm^2 at 77 K. The J_c at 0.5 T was about 25% of the zero-field J_c. This indicates the presence of a strongly linked YBCO film. The irreversibility field is also above 7 T. Similarly, the room-temperature resistivity of the 300-nm-thick YBCO film on CeO_2/YSZ/Eu_2O_3 (sol-gel)/Ni was low, and the measured T_c was about 90 K. The field dependence of J_c for the same film is shown in Fig. 1.18. The measured zero-field I_c was 16 A, which translates to a J_c of 1.1 MA/cm^2. The J_c at 0.5 T is about 20% of the zero-field J_c. Also, a reproducible J_c of more than 0.4 MA/cm^2 at 77 K and self-field was obtained on 300-nm-thick YBCO films on CeO_2 (sputtered)/YSZ (sputtered)/Gd_2O_3 or Yb_2O_3 (sol-gel)/Ni.

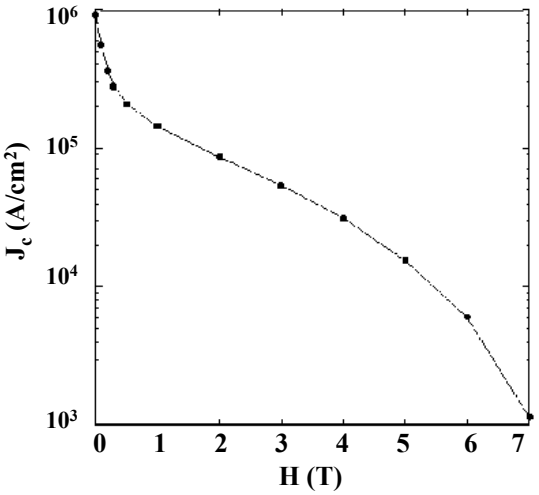

Fig. 1.17. The field dependence of critical current density, J_c, for 300-nm-thick YBCO film on CeO_2 (sputtered)/YSZ (sputtered)/Yb_2O_3 (e-beam)/Ni substrates at 77 K and H||C.

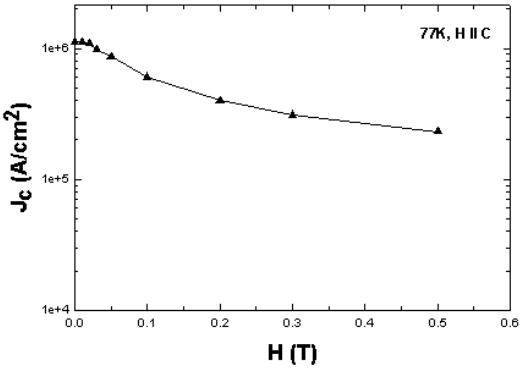

Fig. 1.18. The field dependence of critical current density, J_c, for 300-nm-thick YBCO film on CeO_2 (sputtered)/YSZ (sputter)/Eu_2O_3 (dip-coated)/Ni substrates.

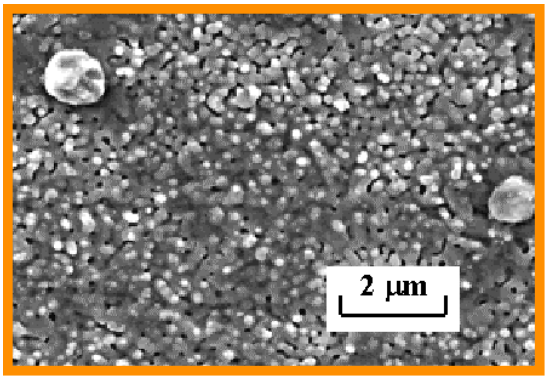
2 μm

Fig. 1.19. SEM micrograph for 300-nm-thick YBCO film on CeO_2 (sputtered)/YSZ (sputtered)/Eu_2O_3 (dip-coated)/Ni sub-

From Figs. 1.17 and 1.18, we can conclude that RE_2O_3 buffers with CeO_2 and YSZ sputtered caps provide a good template for further growth of high-J_c YBCO films through the ex situ BaF_2 precursor process. Furthermore, we note that the performance of the RE_2O_3 sol-gel buffers approached that of the e-beam RE_2O_3 buffers. Efforts are being made to grow YBCO films directly on RE_2O_3-buffered Ni substrates.

An SEM micrograph for 300-nm-thick YBCO film on CeO_2 (sputtered)/YSZ (sputtered)/Eu_2O_3 (dip-coated)/Ni substrate is shown in Fig. 1.19. The microstructure of the YBCO film looks porous but with a plate-like morphology similar to those observed previously for epitaxial Tl-1223 films.

1.3.3 Conclusions

We have demonstrated that several high-quality RE_2O_3 films can be grown epitaxially with a single cube-on-cube orientation on {100}<001> textured Ni substrates using both reactive evaporation and sol-gel processing. The microstructures of RE_2O_3 buffers grown by both techniques were dense, continuous, and crack-free. The performance of sol-gel grown buffers approached the quality of e-beam-grown buffers. High-J_c YBCO films were grown on RE_2O_3 templates with two new buffer-layer architectures. A high J_c of 1.8 MA/cm^2 at 77 K and self-field was obtained on this YBCO/Yb_2O_3/Y_2O_3/Ni architecture. Also, a high J_c (more than 1 MA/cm^2 at 77 K and self-field) was obtained on this YBCO/CeO_2/YSZ/RE_2O_3/Ni architecture.

1.3.4 References

1. M. Paranthaman, D. F. Lee, E. D. Specht, P. M. Martin, X. Cui, J. E. Mathis, R. Feenstra, D. K. Christen, and D. M. Kroeger, "Growth of Biaxially Textured RE_2O_3 Buffer Layers on Rolled-Ni Substrates Using Reactive Evaporation for HTS-Coated Conductors," *Supercond. Sci. Technol.* **12**, 31–25 (1999).

2. J. S. Morrell et al., "Epitaxial Growth of Gadolinium Oxide on Roll-Textured Nickel Using a Solution Growth Technique," *J. Mater. Res.* **15**(93), 621 (2000).

3. D. F. Lee et al., "Alternative Buffer Architectures for High Critical Current Density YBCO Superconducting Deposits on Rolling Assisted Biaxially-Textured Substrates," *Jpn. J. Appl. Phys.* **38**(2B), L178–80 (1999).

1.4 EPITAXIAL GROWTH OF $La_2Zr_2O_7$ THIN FILMS ON ROLLED Ni SUBSTRATES BY SOL-GEL PROCESS FOR HIGH-T_C SUPERCONDUCTING WIRES

T. G. Chirayil, M. Paranthaman, D. B. Beach, J. C. Bryan, D. F. Lee, A. Goyal, R. K. Williams, X. Cui, D. M. Kroeger, R. Feenstra, D. Verebelyi, and D. K. Christen

High-J_c YBCO superconducting films have been grown on RABiTS™ for the purpose of developing superconducting wires for high-temperature, high-magnetic-field applications. The process involves obtaining cube-textured Ni (100) substrates by cold-rolling Ni rods followed by recrystallization. An epitaxial ceramic buffer layer is deposited on the substrate to shield Ni diffusion into the superconducting layer, which can reduce the superconducting properties. In-plane-aligned YBCO superconducting film is then deposited on the buffer layers. The various architectures of buffer layers followed by YBCO films

deposited by vacuum processes such as PLD or e-beam evaporation have been shown to result in J_c values greater than 1 MA/cm^2.

Intense research is currently in progress to grow epitaxial buffer layers and high-J_c superconducting films by nonvacuum processes such as sol-gel or metal organic decomposition (MOD) processes. The nonvacuum approach is attractive for its low cost as well the ease in scalability of the methods. The solution process gives better homogeneity and composition control because the precursors are mixed at atomic levels. Substrates with various shapes and forms can be coated with ease by simple techniques such as spin coating or dip coating.

Initial efforts to grow epitaxial buffer layers on textured-Ni substrates by solution technique resulted in multiple orientations. Morrell et al.[1] at ORNL recently demonstrated the epitaxial growth of a rare earth oxide, Gd_2O_3, buffer layer on textured-Ni (100) substrates by the sol-gel process for the first time. Since then, we have also reported the epitaxial growth of Yb_2O_3 and Eu_2O_3 buffer layers on textured-Ni (100) substrates.[2] A reasonably high J_c value of 4.2×10^5 A/cm^2 was obtained for a YBCO film deposited by the BaF_2 process on RE_2O_3 (RE = Gd, Yb) sol-gel buffered Ni and YSZ and CeO_2 sputtered cap layers. A J_c value greater than 1.1 MA/cm^2 was achieved on Eu_2O_3-based substrates, the highest value reported to date on a sol-gel-based buffer-layer architecture. These results indicate that the sol-gel buffer layers provide a good template and can be key in the development of cost-efficient superconducting wires.

The process window for growing epitaxial RE_2O_3 buffer layers with a single-cube texture is narrow. Some of the rare earth oxides go through a cube-to-monoclinic phase transition. Therefore, alternative buffers are explored. Lanthanum zirconium oxide, $La_2Zr_2O_7$, has a cubic pyrochlore structure and is stable up to ~1500ºC. This aspect enables a wide processing window for the LZO buffer layer. The pseudocubic lattice (half of the diagonal of face-centered-cubic lattice) parameter of 3.882 Å provides a very close lattice match (~0.7%) with YBCO.

Lanthanum zirconate has been of research interest for its catalytical, optical, and electrical properties. The various methods used to synthesize LZO include standard solid-state reaction, coprecipitation, hydrothermal synthesis, and a number of sol-gel routes. The sol-gel chemistry we have used in the preparation of the LZO thin film is entirely different from the works reported in the literature.[3,4,5]

In this paper, we report the epitaxial growth and characterization of LZO thin films on textured Ni (100) substrates for the first time. We also demonstrate a reasonably high J_c YBCO film on the sol-gel buffer layer capped with sputtered YSZ and CeO_2 layers.

1.4.1 Experimental

The lanthanum isopropoxide (Alfa), zirconium n-propoxide in n-propanol (Alfa, 70%) and 2-methoxy ethanol (Alfa, spectrophotometric grade) were used as received. The starting materials were weighed out in an argon-filled glove box, and the solution preparation was carried out under in an argon gas atmosphere using a Schlenck-type apparatus. About 0.988 g (3.125 mmole) of lanthanum isopropoxide and 1.462 g (3.125 mmole) of zirconium n-propoxide was dissolved in 50 ml of 2-methoxyethanol in separate 250-ml round-bottom flasks. The lanthanum methoxyethoxide and zirconium methoxyethoxide were prepared separately by refluxing the isopropoxide with excess 2-methoxyethanol. The isopropanol formed during the reaction was distilled out after refluxing for 1 h. The two precursor solutions were mixed and refluxed for an additional hour before adjusting the concentration to 0.25 M in 2-methoxyethanol. The LZO precursor solution was partially hydrolyzed by adding 1 equivalent of water (1 M H_2O in 2-methoxy-ethanol) per cation equivalent. The solution was allowed to age overnight at room temperature before the substrates were coated by either spin coating or dip coating.

The LZO precursor solution was spin-coated or dip-coated onto textured-Ni substrates. The (100) cube-textured Ni substrates were prepared by annealing the cold-rolled Ni substrates to recrystallization at 800°C for 2 h under vacuum. The Ni substrates were cleaned ultrasonically in isopropanol for 1 h prior to

coating. The spin coatings were applied with a spin coater operated at 2000 rpm for 40 s. The dip coatings were performed at a rate of 3 cm/min.

The samples were placed in a quartz tube and purged with a gas composed of 96% Ar and 4% H_2 for 30 min before introducing them into a preheated furnace at 1150°C for 1 h. The Ni substrates coated with the crystallized LZO buffer layers were then quenched to room temperature inside the quartz tube.

Radio-frequency magnetron sputtering was used to epitaxially deposit YSZ and CeO_2 cap layers on the LZO-buffered Ni substrates at 780°C. The plasma power was 75 W at 13.56 MHz. The YBCO precursor was then deposited on the CeO_2 by e-beam deposition of BaF_2, yttrium metal, and copper metal, and was subsequently annealed in an atmosphere composed of H_2O, O_2, and Ar.

X-ray diffraction of the film was done with a Philips Model XRG3100 diffractometer with Cu Kα radiation. High-temperature X-ray scans were performed with a Siemans D5005 X-ray diffractometer. The Ni substrates coated with LZO precursor film was placed in a closed chamber equipped with a beryllium window. The chamber was flushed with a mixture of 96% Ar and 4% H_2 for 30 min before heat treatment. The X-ray scans were collected in the 2-θ range of 25 to 35° between 800 and 1200°C. A Picker four-circle diffractometer was used to collect pole figures and ω and ϕ scans. The thickness of the LZO buffer layer was determined from Rutherford backscattering spectroscopy (RBS). The Hitachi S-4100 field-emission SEM was used to obtain SEM images. The beam voltage used was 5 kV.

1.4.2 Results and Discussion

The thickness of the golden-colored LZO thin film on the textured Ni after heat treatment was determined to be ~300 Å. The thickness of the buffer layer can be increased with multiple coatings. The θ-2θ scan from 20 to 60° of a single coat, shown in Fig. 1.20, displayed only the (h00) reflections. The peak at 2θ of 33.3° belongs to the LZO phase and is indexed to be the (400) reflection. The strong peak observed at 2θ of 51.8° belongs to Ni (200). This is evidence that the buffer layer is strongly *c*-axis oriented. The high-temperature X-ray scans (Fig. 1.21) showed that the LZO phase forms at ~900°C and is stable at 1200°C. Only the (400) reflection of the LZO phase is observed in the whole temperature range,

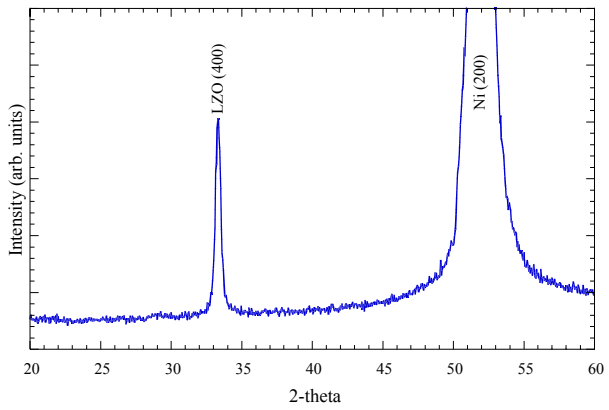

Fig. 1.20. XRD pattern of the LZO thin film on Ni (100) substrate. The θ-2θ scan indicates a strong *c*-axis orientation of the film.

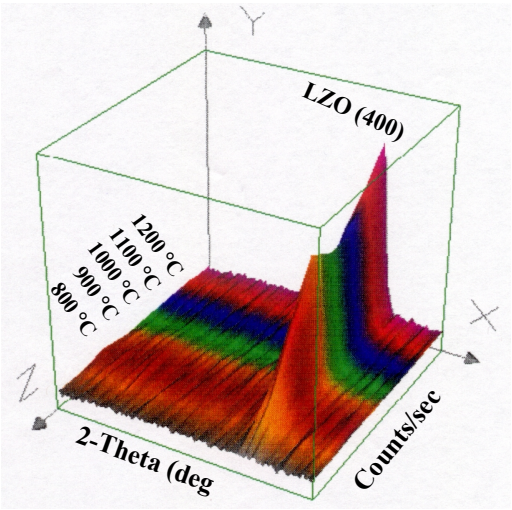

Fig. 1.21. High-temperature X-ray scans of LZO on Ni (100) substrate between 800 and 1200°C in a 96% Ar-4% H_2 gas atmosphere.

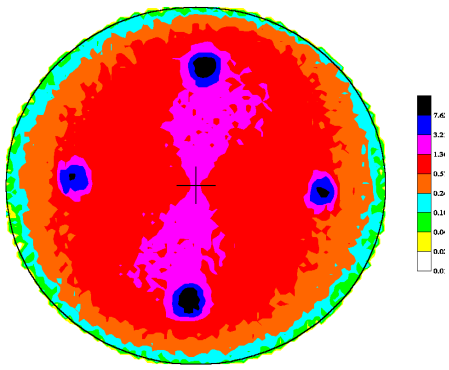

Fig. 1.22. The LZO (222) pole figure shows a single-cube epitaxy.

denoting a wide process window for this buffer layer. The intensity of the (400) peak increased with temperature, indicating better crystallinity at higher temperatures.

The FWHM values of LZO (400) and Ni (200) omega scans were 10.29° and 8.06°, respectively. The FWHM values of the phi scans were 8.97° for LZO (222) plane and 7.52° for Ni (111) plane. The pole figure (Fig. 1.22) of the LZO sol-gel buffer layer showed a single-cube epitaxy on the textured-Ni (100) substrate. From the pole figure, phi scans, and omega scans, we can conclude that the LZO film exhibits a biaxial alignment on the Ni(100) substrate.

The SEM image of the buffer layer at a magnification of 20 k×, showed a continuous and a crack-free microstructure (Fig. 1.23). Multiple coats of the LZO buffer layer also resulted in crack-free films. However, when the concentration of the solution was increased to 1.0 M, mud cracking was noticed in the LZO films.

Attempts to deposit YBCO directly on 600-Å LZO-buffered Ni or on CeO_2 (sol-gel)/ LZO (sol-gel)/ Ni resulted in low T_c values. The X-ray pattern indicated the presence of nickel oxide, which suggested that the buffer layer did not behave as a good diffusion barrier of Ni from the substrate into the superconducting film. Currently, work is in progress to grow thick (3000-Å) LZO buffer layers on the Ni (100) substrates to obtain high-quality YBCO films.

To demonstrate that LZO-buffered Ni substrates could be used as templates to grow quality YBCO films, YSZ and CeO_2 cap layers were deposited on LZO by sputtering. The thicknesses of YSZ and CeO_2 were 5000 Å and 500 Å, respectively. The YBCO film deposited on the CeO_2 was *c*-axis aligned as determined from the θ-2θ scans. The YBCO film had a thickness of about 3000 Å. The ω and ϕ scans on YBCO (BaF_2 process)/CeO_2 (sputtered)/YSZ (sputtered)/ LZO (sol-gel)/Ni are shown in Fig. 1.24. The FWHM values for Ni (111), LZO (222), YSZ (111), and YBCO (103) are 10.6°,

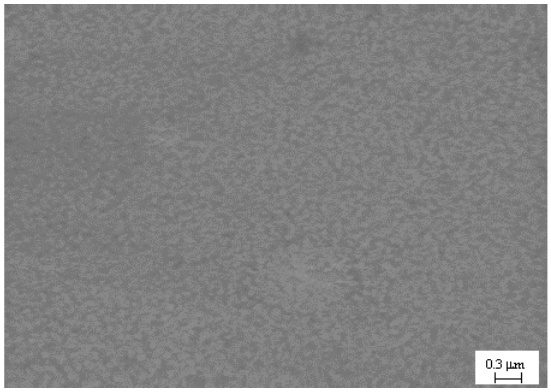

Fig. 1.23. SEM image of the LZO film on Ni (100) substrate at a magnification of 20 k×.

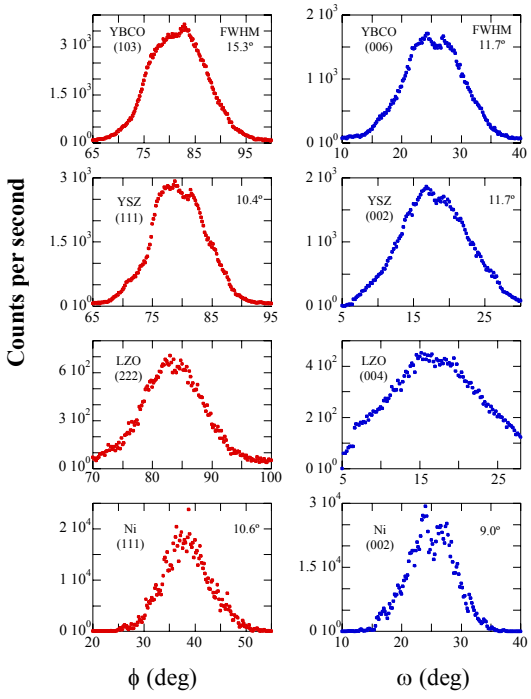

Fig. 1.24. The omega and phi scans for YBCO (BaF_2 process)/CeO_2 (sputtered)/ YSZ (sputtered)/LZO (sol-gel)/Ni (100) substrate.

11.6°, 10.4°, and 15.3°, respectively; values for Ni (002), YSZ (002), and YBCO (006) are 9.0°, 11.7° and 11.7°, respectively. The ω scan showed that the FWHM value for LZO (004) was rather high and was determined to be ~25°.

The resistivity and transport critical current density, J_c, was measured using a standard four-probe technique. The J_c values were calculated using a 1-μV/cm criterion. The temperature-dependent resistivity measurement is shown in Fig. 1.25. The YBCO film had a room-temperature resistivity of 317 μΩ-cm and zero resistance at 89.5 K. The transport J_c of the YBCO film was 4.8×10^5 A/cm^2 at 77 K and zero magnetic field. The J_c values may be suppressed due to the relatively high FWHM values for the LZO buffer layer, which in turn resulted in high FWHM values for the YBCO film. Improving the in-plane and out-of-plane orientations can lead to better critical current density.

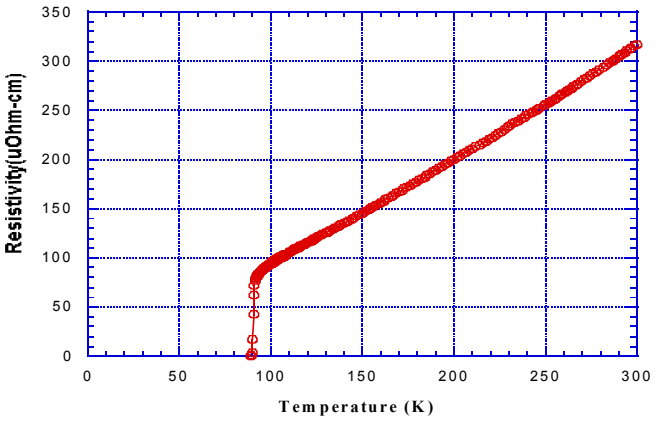

Fig. 1.25. The temperature dependence of resistivity for the YBCO film on CeO_2 (sputtered)/ YSZ (sputtered)/LZO (sol-gel)/textured Ni (100) substrate at 77 K and zero field.

The field dependence of J_c for the YBCO film on CeO_2 (sputtered)/YSZ (sputtered)/LZO (sol-gel)/textured Ni (100) substrate at 77 K and H||C is shown in Fig. 1.26. The J_c of the film decreased to ~1×10^5 A/cm^2 at 0.5 T and to ~1×10^4 A/cm^2 at 5 T from the value at zero field.

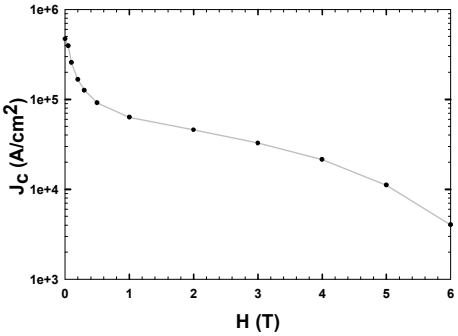

Fig. 1.26. Field dependence of J_c for the YBCO film on CeO_2 (sputtered)/YSZ (sputtered)/LZO (sol-gel)/textured Ni (100) substrate at 77 K and H||C.

1.4.3 Conclusions

The sol-gel technique was used to epitaxially grow LZO buffer layers on textured-Ni (100) substrates for the first time. The LZO buffer layer had a single-cube epitaxy on the substrate. Temperature-dependent XRD showed that the crystallization of the LZO film begins at ~900ºC in an atmosphere of 96% Ar and 4% H_2 and has a wide process window. A YBCO film with a critical current density value of 480,000 A/cm^2 was grown by BaF_2 process. Sputtered YSZ and CeO_2 cap layers were used on LZO-buffered Ni. Attempts are in progress to grow high-quality YBCO films directly on LZO buffer layers.

1.4.4 References

1. J. S. Morrell et al., "Epitaxial Growth of Gadolinium Oxide on Roll-Textured Nickel Using a Solution Growth Technique," *J. Mater. Res.* **15**(93), 621 (2000).

2. T. G. Chirayal et al., "Epitaxial Growth of Yb_2O_3 Buffer Layers on Biaxially Textured-Ni (100) Substrates by Sol-Gel Process," *Mat. Res. Soc. Symp. Proc.* **574,** 51–56 (1999).

3. F. W. Poulson and N. Puil, "Phase Relations and Conductivity of Sr- and La-Zirconates," *Solid State Ionics* **53–56**, 777–83 (1992).

4. M. F. M. Zwinkels et al., "Thermal Stability of Complex Oxide Combustion Catalyst Supports," *Ind. Eng. Chem. Res.* **37**(2), 391–97 (1998).

5. H. Kido, S. Komarneni, and R. Roy, "Preparation of $La_2Zr_2O_7$ by Sol-Gel Route," *J. Am. Ceramic Soc.* **74**(2), 422–24 (1991).

1.5 YBCO COATED CONDUCTORS WITH HIGH ENGINEERING CURRENT DENSITY

M. Paranthaman, C. Park, X. Cui, A. Goyal, D. F. Lee, P. M. Martin, T. G. Chirayil, D. T. Verebelyi, R. Feenstra, D. P. Norton, D. M. Kroeger, and D. K. Christen (ORNL); Chau-Yun Yang and S. E. Babcock (University of Wisconsin)

The successful demonstration of high-performance $YBa_2Cu_3O_{7-y}$ (YBCO) coated conductors from various institutions has generated interest all over the world. This is mainly due to the high cost of Bi,Pb-2223-based powder-in-tube (PIT) wires and to their saturation of the level of performance. The cost of the Bi,Pb-2223 PIT wire is around $300/KA m, as reported by American Superconductor Corporation (ASC). Also, the critical current densities (J_cs) for these conductors are around 70,000 A/cm^2 at 77 K and self-field. This corresponds to an engineering current density, J_E, of more than 21,000 A/cm^2 at 77 K. The absence of biaxial texture in the first generation of Bi,Pb-2223 PIT conductors restricts the limit of its current-carrying capacity. Hence, it is essential to have grain-to-grain orientation with low angle boundaries in the conductors to carry high current densities. The second-generation YBCO coated conductor is one of the best options we have so far. The YBCO-based coated conductors offer the possibility of producing low-cost conductors. In addition, YBCO coated conductors have good field-dependence properties at 77 K. The U.S. Department of Energy's (DOE's) target price for the conductor is close to $10/KA m.

An industrially scalable process for depositing high-quality YBCO films is required. It is possible to use the in situ process, which involves the traditional pulsed-laser deposition (PLD) system or co-evaporation of Y, Ba, and Cu metals under appropriate oxygen atmospheres to fabricate YBCO films.[1] It may be difficult to scale up these processes toward producing low-cost conductors. An alternative, ex situ precursor process can be used. The YBCO precursors used in this process are either co-evaporated Y, BaF_2, and Cu or solution-based Y, Ba, and Cu trifluoroacetates (TFAs). In this process, YBCO precursors can be deposited at room temperature and later post-annealed in a controlled-atmosphere furnace equipped with wet gas mixtures. The advantages of the ex situ process are the separation of the deposition and annealing steps and a wider processing window, made possible by combining temperature, oxygen, and water partial pressures. The control of precursor stoichiometry is straightforward. It can be a batch process. Recently, we have demonstrated that high-current-density YBCO films can be grown on RABiTS™ with the architecture CeO_2/YSZ/CeO_2/Ni using an ex situ BaF_2 precursor process.[2,3] The top CeO_2 layer should be dense, continuous and very compatible with the BaF_2 precursor process. In collaborating with ASC, we have also demonstrated that high-quality YBCO films with a J_c of 1.9 MA/cm^2 at 77 K and self-field can be grown on RABiTS™ by the TFA process.[4] Here, we report our success in fabricating high-J_E YBCO films on PLD-buffered RABiTS™ using the ex situ BaF_2 precursor process.

Biaxially textured Ni (100) substrates were obtained by the mechanical deformation of Ni rods over 95% followed by recrystallization to the desired {100}<001> cube texture by annealing at 1000°C for 1 h in a high-vacuum furnace with a base pressure 2×10^{-6} Torr. After annealing, the Ni substrates were mounted on a heater block using Ag paint and were loaded into the vacuum chamber for PLD. A KrF excimer laser beam with a density of 2.6 J/cm^2 and a deposition rate of 0.25 nm/s was used to deposit both YSZ and CeO_2 layers at 600 to 800°C. The initial nucleation layer of ~5-nm-thick YSZ was deposited at a background pressure of 2×10^{-6} Torr, followed by the additional deposition of a 200-nm-thick YSZ film with an oxygen partial pressure [$P(O_2)$] of 10^{-4} Torr. The initial deposition of YSZ under vacuum is very critical in obtaining the (100) texture. The CeO_2 top layers were deposited under similar YSZ conditions.

Experimental details were reported earlier.[5] The CeO_2-buffered YSZ/Ni substrates were annealed under Ar at 500°C for 1 h prior to superconductor deposition.

YBCO precursor films were grown on both CeO_2-buffered YSZ (100) single-crystal substrates and PLD-buffered (CeO_2/YSZ/Ni) substrates using e-beam co-evaporation of Y, BaF_2, and Cu at a combined deposition rate of ~0.6 nm/s. An AIRCO Temescal CV-14 10-kW power supply with three e-beam guns was used for the deposition. The RABiTS™ samples were mounted on a 4 × 4 in. Cu block inside the e-beam chamber. The deposition was done at room temperature. During evaporation, the initial pressure of 1×10^{-6} Torr rose to 2×10^{-5} Torr. Either graphite or tungsten crucibles were used for the Y and Cu sources. Tantalum crucibles with matching perforated lids were used for steady BaF_2 deposition. To determine the amount of the oxygen and water present, a Dycor Quadruple Gas Analyzer was mounted in the e-beam system. The background H_2O pressure was around 2×10^{-5} Torr. During the deposition, H_2O was introduced into the system to keep the H_2O pressure constant. (The failure to keep the H_2O pressure constant will possibly alter the deposition rate of both Y and Cu. Hence, it is important to keep the H_2O pressure constant during deposition.) The YBCO precursor films were shiny, brown-black in color, and very stable in air. The room-temperature XRD indicated the presence of amorphous oxides and small crystallites of BaF_2 in the precursors. The YBCO precursor films were then post-annealed in a controlled-atmosphere furnace with humid gas mixtures and low $P(O_2)$. The dependence of vapor pressure of H_2O with temperature based on thermodynamic considerations is plotted in Fig. 1.27. The H_2O dew point of 40°C corresponds to approximately 55 Torr of H_2O pressure. During the anneal, the wet gas was switched to dry gas after a certain time. The sample was then cooled to 500°C in 20 min for 30-min oxidation anneals in 1 atm O_2. The high-temperature anneal under wet conditions resulted in conversion of the Y, BaF_2, and Cu into $YBa_2Cu_3O_{7-y}$. The important parameters for this post-annealing process are gas flow rate, H_2O vapor pressure, $P(O_2)$, temperature, and wet annealing time.

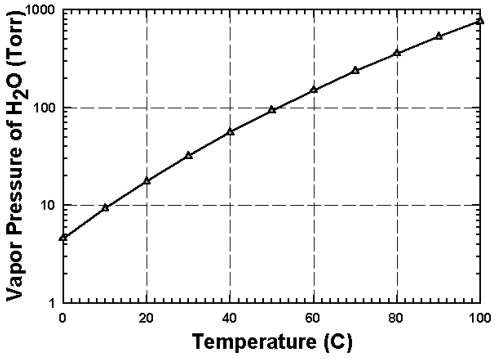

Fig. 1.27. The temperature dependence vapor pressure of H_2O from the thermodynamic considerations.

The films were analyzed by XRD. A Philips model XRG3100 diffractometer with Cu K_a radiation was used to record powder diffraction patterns. A Picker four-circle diffractometer was used to determine the texture of the films. The out-of-plane alignment (ω scans) was measured by scanning the (100) planes of the film. The in-plane alignment (ϕ scans) was determined by measuring the (111) planes of the film. A pole figure was collected for all the layers to determine whether the film had a single-cube texture. SEM micrographs were taken using a Hitachi S-4100 field-emission SEM. The beam voltage used was 10 kV. The thickness of the films was determined by both RBS and Alpha Step profilometer scans. The resistivity and transport critical current density, J_c, were measured using a standard four-probe technique. Values of J_c were calculated using a 1-mV/cm criterion.

The stoichiometry of the e-beam co-evaporated Y, BaF_2, and Cu precursors to produce YBCO was adjusted using the RBS studies. Typical RBS spectra of e-beam co-evaporated YBCO precursors on Si are shown in Fig. 1.28. The simulation studies indicate that the stoichiometry is close to 123. PLD was used to grow high-quality YSZ films directly on {100}<001> textured-Ni substrates with a single-cube texture and without the initial CeO_2 seed layer for the first time. The details of the results were reported earlier.[5] The typical YSZ thickness is around 250 nm. A thin CeO_2 top layer was deposited on YSZ-buffered Ni substrate to enhance the compatibility with the BaF_2 precursor process. Detailed microstructure studies indicate that these buffer layers were dense, highly crystalline, continuous, and crack-free. The YBCO

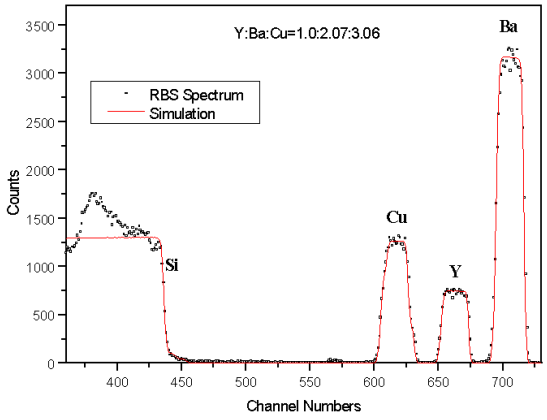

Fig. 1.28. Rutherford backscattering spectra of a typical 300-nm-thick e-beam co-evaporated YBCO precursor (Y, BaF_2, and Cu) on Si. The spectra were measured with 5.0-MeV He ions at near-normal incidence, detected at 160° scattering angle.

precursors were co-evaporated on PLD-buffered CeO_2/YSZ/Ni substrates. As a test model, YBCO precursors were also deposited on CeO_2-buffered YSZ (100) single-crystal substrates. The YBCO films grown on CeO_2-buffered YSZ single-crystal substrates were shiny and black. The room-temperature resistivities of the YBCO films were very low (~300 μΩ-cm) and had a T_c of about 90 K. The extrapolated values of the resistivity data (between 300 K and above T_c) below zero indicate the presence of predominantly c⊥ YBCO films. A high J_c (more than 3.1 MA/cm^2) for a YBCO film thickness of 0.29 μm at 77 K and self-field was obtained. The I_c and J_c data for YBCO films grown on various substrates are reported in Table 1.3.

The typical θ-2θ scans of a 1-mm-thick YBCO film on PLD-buffered CeO_2/YSZ/Ni substrate, as shown in Fig. 1.29, indicate the presence of a *c*-axis-aligned film. A small impurity peak at ~28.7°, which may be indexed as belonging to $BaCeO_3$, indicates that there is some interaction between the CeO_2 layer and YBCO. Typically for high-J_c YBCO films, this $BaCeO_3$ impurity is almost suppressed. A small amount of NiO impurity was also observed in the film.

As shown in Fig. 1.30, the XRD results from ω and ϕ scans on YBCO/CeO_2/YSZ/Ni revealed good epitaxial texturing. The FWHM values for Ni (002), YSZ (002), CeO_2 (002), and YBCO (006) are 8.5°, 8.1°, 10.0°, and 8.4°, respectively; those of Ni (111), YSZ (111), CeO_2 (111), and YBCO (103) are 11.8°, 11.7°, 11.5°, and 13.6°, respectively. The field dependence of J_c for the same film is shown in Fig. 1.31. The zero-field I_c measured was 39 A, which translates to a J_c of 1.1 MA/cm^2 at 77 K (see Table 1.3). The J_c at 0.5 T was about 25 % of the zero-field J_c. This indicates the presence of a strongly linked YBCO film. The irreversibility field is around 5 T. A high J_E of 21,118 A/cm^2 at 77 K and self-field was observed for this film. A SEM micrograph for 1-mm thick YBCO film on PLD-buffered CeO_2/YSZ/Ni substrate is shown in Fig. 1.32. The microstructure of the YBCO film looks porous, but with a plate-like morphology similar to that observed previously for epitaxial Tl-1223 films.

Table 1.3. YBCO films deposited on RABiTS™ using e-beam co-evaporated Y, BaF_2, and Cu precursors

Substrate	YBCO thickness (μm)	Sample width (mm)	I_c (A)	J_c (A/cm^2) 77 K, self-field	J_E (A/cm^2)
CeO2/YSZ (100) xtal	0.29	1.0	9.1	3.1×10^6	-
CeO2/YSZ/Ni[a]	1.0	3.6	39.0	1.1×10^6	21,118
CeO2/YSZ/Ni[a]	1.6	3.0	44.0	0.9×10^6	28,260
CeO2/YSZ/Ni[a]	2.3	3.5	6.7	0.8×10^6	-

[a]Ni substrate thickness is 50 μm, and the total buffer layer thickness is about 0.3 μm.

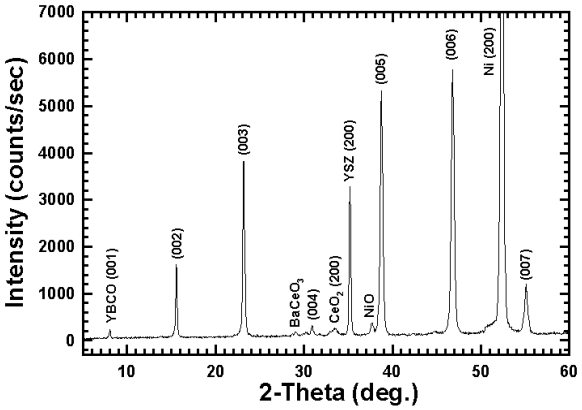

Fig. 1.29. A typical θ–2θ scan for a 1-μm-thick YBCO film on PLD-buffered CeO_2/YSZ/Ni substrates.

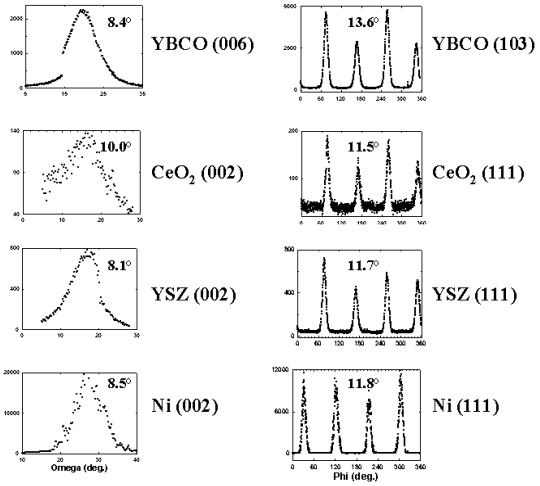

Fig. 1.30 The ω and ϕ scans for a 1-μm-thick YBCO film on PLD-buffered CeO_2/YSZ/Ni substrates. The FWHM values for each scan are shown inside the scans.

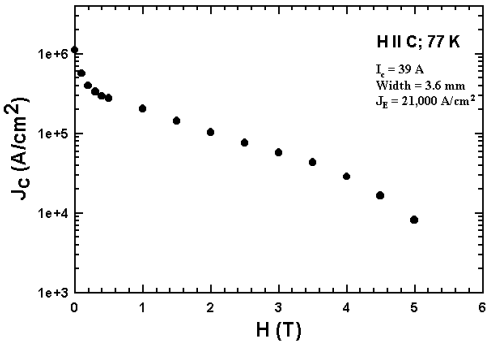

Fig. 1.31 The field dependence of critical current density, J_c, for 1-μm-thick YBCO film on PLD-buffered CeO_2/YSZ/Ni substrates. This film carried an I_c of 39 A, which corresponds to a J_E of 12,118 A/cm^2 at 77 K and self-field.

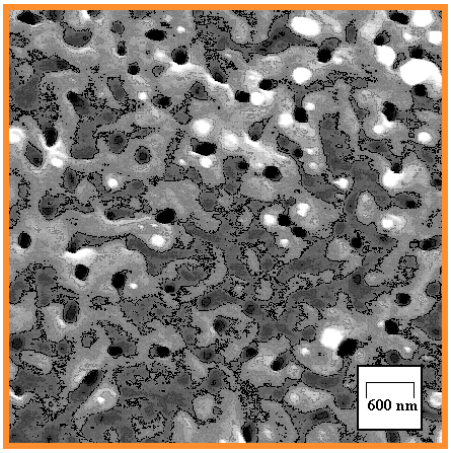

Fig. 1.32. SEM micrograph for a 1-μm-thick YBCO film on PLD-buffered CeO_2/YSZ/Ni.

The XRD studies indicated the presence of good epitaxial texturing for 1.6-μm-thick YBCO films grown on CeO_2/YSZ/Ni substrates. The FWHM values for Ni (002), YSZ (002), and YBCO (006) are 8.8°, 8.8°, and 9.6°, respectively; those of Ni (111), YSZ (111), and YBCO (103) are 10.6°, 11.3°, and 14.1°, respectively. The CeO_2 scans were broad. The zero-field I_c measured was 44 A, which translates to a J_c of 0.9 MA/cm^2, and a J_E of 28,260 A/cm^2 at 77 K and self-field (Table 1.3). This is the highest J_E reported so far for a YBCO film grown on RABiTS™. In spite of the broad YBCO (103) scan, the films carried a J_c close to 1 MA/cm^2. This could be due to the presence of low-angle grain boundaries. Our recent studies on the grain boundary map of ex situ YBCO films on RABiTS™ indicated that the grains are well connected within 2 to 3°. Hence, the J_c threshold could be 2 to 3°. Similar studies on these thick

YBCO films are in progress. Our preliminary studies indicate that it may be difficult to grow >1 MA/cm^2, 2.3-mm-thick YBCO films on PLD-buffered RABiTS™. The YBCO films carried a J_c of only 0.8×10^5 A/cm^2 at 77 K and self-field (Table 1.3). It appears that YBCO films that are more than 2-μm thick had poor transport properties. Optimization of thick YBCO film processing is in progress.

1.5.1 Conclusion

We have demonstrated that high-J_E YBCO films can be grown on PLD-buffered CeO_2/YSZ/Ni substrates using ex situ BaF_2 precursor process. The initial nucleation of epitaxial YSZ layers was deposited directly on biaxially textured Ni (100) substrates under vacuum using PLD. The YBCO films were grown on PLD-buffered CeO_2/YSZ/Ni (100) substrates using e-beam co-evaporated Y-BaF_2-Cu precursors followed by post-annealing. On CeO_2-buffered YSZ (100) single-crystal substrates, high-quality YBCO films with a J_c of over 3.1 MA/cm^2 at 77 K were grown. Also, high-quality YBCO films 1.6 μm thick and 3 mm wide carried an I_c of 44 A. This corresponds to a J_E of more than 28,000 A/cm^2 at 77 K.

1.5.2 References

1. H. Kinder et al., "YBCO Film Deposition on Very Large Areas Up to 2 × 2 cm^2," *Physica C* **282–287**(1) 107–110 (1997).

2. R. Feenstra et al. "Effect of Oxygen Pressure on the Synthesis of $YBa_2Cu_3O_{7-x}$," *J. Appl. Phys.* **69**(9), 6569–85 (1991).

3. R. Feenstra, D. K. Christen, and M. Paranthaman, "Method for Making High-Critical-Current-Density $YBa_2Cu_3O_7$ Superconducting Layers," U.S. Patent No. 5,972,847, October 26, 1999.

4. S. Annavarapu, et al., "Progress Towards A Low-Cost Coated Conductor Technology," *Physica C* (in press) (2000).

5. F. A. List et al., "High J_c YBCO Films on Biaxially Textured Ni with Oxide Buffer Layers Deposited Using Electron Beam Evaporation and Sputtering," *Physica C* **302**(1), 87–92 (1998).

1.6 NUCLEATION OF EPITAXIAL YTTRIA-STABILIZED ZIRCONIA ON BIAXIALLY TEXTURED (001) Ni FOR DEPOSITED CONDUCTORS

C. Park, D. P. Norton, D. F. Lee, D. T. Verebelyi, A. Goyal, D. K. Christen, and J. D. Budai

Significant effort to develop HTS wire or tape has focused on the epitaxial growth of superconducting films on biaxially textured metals.[1–3] This approach is dependent on the heteroepitaxial growth of oxide buffer-layer films on metal surfaces. In order to realize an HTS film possessing a high critical current on a biaxially textured metal substrate, the buffer layer architecture must satisfy a set of rather stringent requirements. The buffer layer construct must be chemically compatible with both the metal and the superconductor. It must be mechanically robust so as to prevent microcrack formation at the HTS-buffer layer interface. It must also be epitaxial relative to the biaxially textured metal with a singular (001) orientation. The latter requirement is particularly challenging because the epitaxy of metal oxides on metal surfaces is determined not only by the relative lattice match between film and substrate, but by possible roles of a native oxide layer and/or intermetallic phases formed during film nucleation.

In previous work, these objectives have required multilayer combinations of various oxide buffer layers. Superconducting films with critical current densities in excess of 1 MA/cm^2 at 77 K have been achieved for epitaxial $YBa_2Cu_3O_7$ films on rolled-textured Ni substrates with the use of certain epitaxial buffer-layer constructs.[4] For example, CeO_2 has been used to nucleate an epitaxial (001)-oriented oxide layer on a biaxially textured (001) Ni surface.[5] A tendency for the CeO_2 layer to crack due to differences in thermal expansion coefficients of the oxide film and metal tape requires an additional epitaxial yttria-

stabilized zirconia (YSZ) buffer layer on the CeO_2 in order to achieve crack-free superconducting films.[1,2] In this case, the superior mechanical properties of the YSZ layer circumvent the cracking problem and enable the formation of superconducting films with high critical currents.

Though effective in forming a high-current superconducting tape, the use of a multilayer buffer architecture introduces significant complexity to the fabrication process. Ideally, one would prefer to use a single buffer layer. One of the most attractive materials for a single buffer layer that is mechanically robust and chemically inert is YSZ.[6–8] Unfortunately, previous efforts to grow epitaxial YSZ films with a single (001) orientation directly on rolled-textured (001) Ni tapes have been unsuccessful, with a mixture of (100) and (111) orientation realized. In this section, we report on the nucleation and growth of epitaxial (001) YSZ on the (001) Ni surface using pulsed-laser deposition (PLD). Nucleation on an oxide-free (001) biaxially textured Ni surface yields a mixed (111) and (001)-oriented film. However, (001)-oriented epitaxy is achieved by nucleating the YSZ film on a surface that is apparently oxygen terminated. Exposing the surface to conditions where significant NiO forms results in the nucleation of polycrystalline material. Using the (001)-oriented YSZ as a template, a $YBa_2Cu_3O_7$/YSZ/biaxially textured Ni structure with a high J_c is realized.

The substrates used in this study were biaxially textured (001) Ni tapes (50 μm thick) produced by cold-rolling and annealing.[9] The starting purity of the Ni tape was 99.99%. For texture development, the cold-rolled metal tape was enclosed in a tantalum envelope and annealed in vacuum with a base pressure of 2×10^{-6} Torr at 800 to 1000°C for 60 min. The tantalum envelope serves as a local oxygen getter during the anneal. The degree of in-plane and out-of-plane texture for the substrates as determined by X-ray diffraction (XRD) rocking curves was approximately 8°. After annealing, the Ni tape was stored in air until mounted on a heater block using Ag paint and loaded into an o-ring-sealed vacuum chamber for PLD. Exposure to air almost immediately oxidized the nickel surface. A 10 mol. % yttria-stabilized ZrO_2 ceramic target was used to deposit the YSZ film. A KrF excimer laser beam was incident on the rotating target surface at an angle of 45°. The laser energy density was 2.6 J/cm^2 with a deposition rate of 0.25 nm/s. The target-to-substrate distance was 7 cm. The base pressure of the growth chamber was 10^{-6} Torr, assumed to consist primarily of water vapor. The YSZ nucleation experiments were performed in the temperature range of 600 to 800°C.

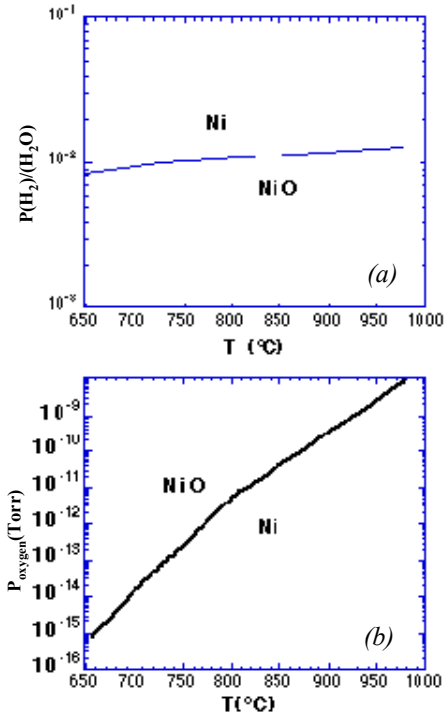

Fig. 1.33 Stability curves for NiO (*a*) as a function of $P(H_2)/P(H_2O)$ and (*b*) as a function of $P(O_2)$.

For the experiments reported here, an initial nucleation layer (~5 nm) of YSZ was deposited under various conditions, followed by the additional epitaxial growth of a 200-nm-thick YSZ film with $P(O_2) = 10^{-4}$ Torr. The relatively thick epitaxial film grown on the nucleated template layer effectively reflects the crystalline orientation of the nucleated layer. Three ambient conditions were considered during nucleation. First, nucleation was carried out on an oxide-free surface by introducing sufficient hydrogen partial pressure (up to 200 mTorr of a 4% H_2 and 96% Ar mixture) so as to reduce any NiO on the Ni surface as determined from the thermodynamics of NiO reduction (case A). Figure 1.33 (*a*) shows the stability curve for NiO in the presence of hydrogen and water vapor.[10] For $P(H_2)/P(H_2O) > 10^{-2}$ at T > 600°C, NiO will be reduced, yielding an oxide-free surface. Second, nucleation was performed under base pressure

conditions (case B). For a vacuum system with a base pressure of ~ 10^{-6} Torr, the residual oxygen pressure will be at least 10^{-8} Torr. According to Ellingham diagrams for binary oxides, the equilibrium oxygen partial pressure for NiO heated to 600 to 800°C should be in the range of 10^{-16} to 10^{-11} Torr as illustrated in Fig. 1.33 (*b*).[10] Under the above conditions, oxygen termination of the surface would be expected. Lastly, nucleation was carried out in an oxygen partial pressure of 5×10^{-6} Torr or greater (case C). Under these conditions, significant NiO coverage of the Ni surface is expected.

For nucleation of YSZ in the presence of sufficient hydrogen to yield an oxide-free nickel surface (case A), polycrystalline films with mixed orientation were realized. This differs from the case for CeO_2, where (001) epitaxy is achieved via nucleation on an oxide-free nickel surface.[1,2] One possible explanation for this difference in CeO_2 and YSZ nucleation resides in the different cation chemistry. Ce can exist in either +4 or +3 valence, while Zr is a monovalent +4. Within the cubic fluorite structure, CeO_{2-x} can accommodate significant oxygen deficiency, while YSZ cannot for a given cation composition. The excess Zr may react with the nickel surface, forming intermetallic compounds that interfere with (001) epitaxy. Additional work needs to be performed to address this issue.

In contrast to nucleation in the presence of hydrogen, nucleation of YSZ at a base pressure of 10^{-6} Torr (case B) results in a singular (001) epitaxial relationship. X-ray diffraction θ-2θ scans along the surface normal show that the epitaxial (001) YSZ film is nucleated on the Ni (001) substrate at 800°C in a background pressure of 2×10^{-6} Torr with no intentional oxygen or hydrogen flow. The film is essentially 100% (001) oriented with an intensity ratio of the (111) to (200) peaks less than 0.01. X-ray diffraction ω scans and ϕ scans of the YSZ peaks indicate that the film is in-plane aligned and epitaxial with respect to the biaxially textured Ni substrate. The in-plane and out-of-plane mosaic spread for the film is slightly smaller than that measured for the substrate. Similar results were obtained for films deposited at temperatures as low as 600°C. For the case where an oxygen partial pressure greater than 5×10^{-6} Torr is introduced during either substrate heating or film nucleation (case C), a significant or dominant YSZ (111) oriented component was evident in the XRD data. An oxygen partial pressure of 10^{-5} Torr or greater during nucleation yields nearly 100% (111)-oriented YSZ.

This study shows that epitaxial (001) YSZ can be nucleated on a Ni(001) surface that is oxygen terminated under limited oxidation conditions that do not lead to significant polycrystalline NiO formation. Surface studies have shown that ~ 3 monolayers of NiO rapidly form on a (001) Ni surface when exposed to oxygen at room temperature.[11–13] Based on the Gibbs free energy for NiO thermal decomposition, desorption of this native NiO layer from the nickel surface under conditions used during film nucleation would not be anticipated.[10] Previous studies on the oxidation of the (001) Ni surface indicate that the native NiO formed at ambient temperatures is polycrystalline with multiple orientations.[11,13] However, the formation of a fine-grained (001) oriented epitaxial NiO layer has been observed after moderate vacuum annealing of an initially mixed oriented NiO thin layer using reflection high-energy electron diffraction (RHEED).[13] It is therefore conceivable that the YSZ (001) nucleates on a (001) NiO surface. However, the Gibbs free energy at 800°C for YSZ is significantly larger in magnitude than that for NiO.[10] Thermodynamically, the reduction of NiO by YSZ is favored. The RHEED studies of ref. 13 were performed on well-oriented single-crystal (001) Ni surfaces, while the (001) biaxially textured Ni substrates used in this work possess a highly oriented polycrystalline structure in which the (001) axis orientations of the individual grains relative to the surface normal have a mosaic spread on the order of 8°. Similar results have also been observed for the epitaxial growth of YSZ on (001) Si, where a thin, amorphous SiO_2 layer is beneficial to achieving (001)-oriented epitaxy.[14–16]

In order to elucidate the surface conditions at nucleation, we have investigated the progression of the Ni(001) surface as a function of background pressure conditions using RHEED in a separate ultrahigh vacuum (UHV) chamber. A biaxially textured Ni substrate was heated to 800°C in $P(H_2) = 8 \times 10^{-7}$ Torr with a base pressure of 1×10^{-8} Torr, then cooled to 700°C and exposed to oxygen. Figure 1.34 (*a*) shows

the initial RHEED pattern at 800°C in $P(H_2) = 8 \times 10^{-7}$ Torr. Based on thermodynamic stability data, the Ni surface is considered to be oxide-free under these conditions. The individual spots presumably represent diffraction from individual Ni grains. Figure 1.34(*b*) shows the RHEED pattern with $P(O_2) = 1.5 \times 10^{-7}$ Torr. Also shown is a plot of the intensity for the (001) Ni specular reflection as the oxygen partial pressure is increased. At $P(O_2) = 1.5 \times 10^{-7}$ Torr, one expects the nickel surface to be oxidized. The RHEED patterns before and after the introduction of $P(O_2) = 1.5 \times 10^{-7}$ Torr are quite similar. There appears to be evidence for NiO (100), although the diffusely scattered nature of the pattern makes this difficult to delineate. As $P(O_2)$ is increased to 1.5×10^{-7} Torr, a slight decrease in the specular reflection intensity is observed. At $P(O_2) > 10^{-6}$ Torr, the RHEED pattern becomes weak and polycrystalline in nature. Clearly a polycrystalline oxide forms on the surface for $P(O_2) > 10^{-6}$ Torr. This is the oxygen pressure that yielded (111) YSZ nucleation. The polycrystalline NiO RHEED pattern remained if the oxygen was then removed to $P(O_2) < 10^{-8}$ Torr, indicating that the oxidized surface is relatively stable once formed.

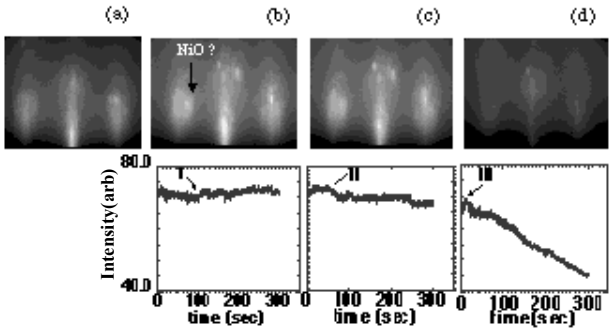

Fig. 1.34. Reflection high-energy electron-diffraction results showing the RHEED pattern of a biaxially textured (001) Ni substrate taken along the Ni(110) direction at (*a*) 800°C in $P(H_2) = 8 \times 10^{-7}$ Torr, and at 700°C in (*b*) $P(O_2) = 1.5 \times 10^{-7}$ Torr, (*c*) 5×10^{-7} Torr, and (*d*) 1.6×10^{-6} Torr. Plots of the specular intensity are also shown, and the point of oxygen introduction is noted (I, II, and III).

With the epitaxial growth of high-quality YSZ on biaxially textured nickel, a single-buffer-layer architecture for the growth of $YBa_2Cu_3O_7$ becomes possible. A 0.25-nm-thick $YBa_2Cu_3O_7$ film was deposited on the 250-nm YSZ layer at a deposition temperature of 750°C and oxygen pressure of 200 mTorr. A θ-2θ XRD scan along the surface normal for the Y $YBa_2Cu_3O_7$/YSZ/Ni structure shows only *c*-axis-oriented $YBa_2Cu_3O_7$, with the intensity ratio of the YSZ (111) to (200) peaks less than 0.02. X-ray diffraction ω scans and ϕ scans for the YSZ and $YBa_2Cu_3O_7$ peaks show that the layers are in-plane aligned and epitaxial with respect to the biaxially textured Ni substrate. The in-plane and out-of-plane mosaic spreads for the $YBa_2Cu_3O_7$ and YSZ layers are similar to that measured for the metal tape. Scanning electron microscopy images of the (001) YSZ/Ni films show no evidence for microcracking in the YSZ layer. The critical current density at 77 K for the $YBa_2Cu_3O_7$ film was 0.5 MA/cm^2, which is the highest reported value for any epitaxial $YBa_2Cu_3O_7$ film on biaxially textured metal substrate with a single buffer layer separating the superconductor from the biaxially textured metal substrate. For this sample, two in-plane variants of the $YBa_2Cu_3O_7$ film, rotated by 45°, are present. This is commonly observed for $YBa_2Cu_3O_7$ epitaxial films deposited on a (001) YSZ surface and is due to the lattice mismatch between $YBa_2Cu_3O_7$ and YSZ.[16] Minimizing or eliminating one of the in-plane variants by optimization of film-growth temperature and oxygen partial pressure should lead to a significant increase in the critical current density for this architecture. A reproducible approach to eliminating one of these in-plane variants is to deposit a thin, epitaxial capping layer of CeO_2 or Y_2O_3 on the YSZ layer to improve the lattice match with $YBa_2Cu_3O_7$.[17,18] Incorporating this capping layer into the above architecture resulted in a relatively simple biaxially textured superconducting structure with a critical current density greater than 1 MA/cm^2.

1.6.1 Conclusion

We have investigated the nucleation of epitaxial YSZ directly on biaxially textured (001) Ni tapes using pulsed-laser deposition. The orientation of YSZ on the (001) Ni surface depends on the initial state of the

substrate, with (001) epitaxy possible by nucleation on an oxygen-terminated metal surface. The epitaxial (001) YSZ layer grown on the Ni (001) surface can be used as a single-buffer layer for a high-temperature superconducting coated conductor architecture, yielding superconducting $YBa_2Cu_3O_7$ films with high critical current densities.

1.6.2 References

1. D. P. Norton et al., "Epitaxial $YBa_2Cu_3O_7$ on Biaxially Textured Nickel (001): An Approach to Superconducting Tapes with High Critical Current Density," *Science* **274**(5788), 755–57 (1996).

2. A. Goyal et al., "High Critical Current Density Superconducting Tapes by Epitaxial Deposition of $YBa_2Cu_3O_x$ Thick Films on Biaxially Textured Metals," *Appl. Phys. Lett*. **69**(12), 1795–97 (1996).

3. M. Paranthaman et al., "Growth of Biaxially Textured RE_2O_3 Buffer Layers on Rolled-Ni Substrates Using Reactive Evaporation for HTS Coated Conductors," *Supercond. Sci. Technol.***12**(5), 319–25 (1999).

4. C. Park et al., "Bend Strain Tolerance of Critical Currents for $YBa_2Cu_3O_7$ films Deposited on Rolled-Textured (001) Ni," *Appl. Phys. Lett.* **73**(13), 1904–1906 (1998).

5. D. P. Norton et al., "Epitaxial Growth of Oxide Thin Films on (001) Metal Surfaces Using Pulsed-Laser Deposition," pp. 401–406 in *Materials Research Society Symp. Proc.* Vol. 474, (Materials Research Society, Pittsburg, 1997).

6. P. Spielbuchler and G. Gritzner, "Mechanical Properties of Yttria-and Ceria-Doped Zirconia Ceramics," *J. Mater. Sci. Lett.* **11**(21) 1426–28 (1992).

7. G. N. Morscher, P. Pirouz, and A. H. Heuer, "Temperature Dependence of Hardness in Yttria-Stabilized Zirconia Single Crystals," *J. Am. Ceram. Soc.* **74**(13), 491–500 (1991).

8. S. Maschio, O. Sbaizero, and S. Meriani, "Mechanical Properties of the Ceria-Zirconia System," *J. Euro. Ceram. Soc.* **9**, 127–32 (1992).

9. H. Makita, S. Hanada, and O. Izumi, "Recrystallization in Cold-Rolled Pure Nickel," *Acta Metall.* **36**(2), 403–12 (1988).

10. T. B. Reed, *Free Energy of Formation of Binary Compounds*, MIT Press, Cambridge, Mass., 1971.

11. N. N. Khoi, W. W. Smeltzer, J. D. Embury, "Growth and Structure of Nickel Oxide on Nickel Crystal Faces," *J. Electrochem. Soc.: Solid State Sci. & Technol.* **122**(11), 1495–1503 (1975).

12. P. H. Holloway and J. B. Hudson, "Kinetics of the Reaction of Oxygen with Clean Nickel Single Crystal Surfaces," *Surf. Sci.* **43**, 123–40 (1974).

13. D. F. Mitchell, P. B. Sewell, and M. Cohen, "A Kinetic Study of the Initial Oxidaton of the Ni(001) Surface by RHEED and X-ray Emission," *Surf. Sci.* **61**, 355–76 (1976).

14. R. D. Vispute et al., "Realization of $Y_1Ba_2Cu_3O_{7-\delta}$ /Y-ZrO_2 Epitaxial Configuration on Silicon (100) by Pulsed Laser Ablation Without Chemical Removal of Native Surface Oxide," *Physica C* **199**(1&2), 59–64 (1992).

15. A. Bardal et al., "Initial Stages of Epitaxial Growth of Y-Stabilized ZrO_2 Thin Films on a-SiO_x/Si (001) Substrates," *J. Appl. Phys.* **75**(6), 2902–16 (1994).

16. S. M. Garrison et al., "Observation of Two In-Plane Epitaxial States in $YBa_2Cu_{y-\delta}$ Films on Yttria-Stabilized Zirconia," *Appl. Phys. Lett.* **58**(19), 2168–70 (1991).

17. D. K. Fork et al., "Effects of Homoepitaxial Surfaces and Interface Compounds on the In-Plane Epitaxy of YBCO Films on Yttria-Stabilized Zirconia," *J. Mater. Res.* **7**(7), 1641–51 (1992).

18. G. L. Skofronick et al., "Interfacial Reaction Products and Film Orientation in $YBa_2Cu_3O_{7-x}$ on Zirconia Substrates With and Without CeO_2 Buffer Layers," *J. Mater. Res.* **8**(11) 2785–98 (1993).

1.7 STRENGTHENED, REDUCED-MAGNETISM SUBSTRATES

A. Goyal, R. Feenstra, D. F. Lee, M. Paranthaman, D. M. Kroeger, C. Park, and D. P. Norton

Various binary alloys of Ni, including Ni-Cr alloys, Ni-V alloys, Ni-W alloys, Ni-Cu alloys, Ni-Mo alloys, and their ternary alloys with other metals such as Al or Mg, were investigated. Significant progress was made in texturing these alloys. We report here results on only the Ni-Cr substrates.

1.7.1 Properties of Textured Ni-Cr Alloy Substrates

Substrates with Cr concentrations ranging from 0 to 13 at. % were studied. It was found that with increasing Cr additions, the Curie point decreased and magnetic moment of the sample decreased considerably. Plots of magnetization vs applied magnetic field indicate that the hysteresis at 77 K for even a 7 at. % Cr substrate was significantly less than that for pure Ni. When the Cr concentration reaches 13 at. %, the sample had no observable hysteresis and the sample was nonmagnetic at 77 K.

Figure 1.35 shows a background-corrected log-scale pole figure of Ni-13%Cr substrate. Only four peaks corresponding to the cube orientation are present. It is important to note that any deleterious, secondary texture components, if present, would have been visible in the log-scale pole figure shown in Fig. 1.35. The texture of this substrate is as good as that obtained for 99.99% Ni. The full-width-half-maximum (FWHM) of the out-of-plane texture as measured using an X-ray rocking curve or an ω-scan is 4.7° in the rolling direction and 8.3° about the rolling direction. The FWHM of the in-plane texture as measured by an X-ray ϕ-scan was 7.0°. Figure 1.36, an orientation micrograph image, created by electron backscatter Kikuchi diffraction, shows the grain orientations in the substrate. In Fig. 1.36, the grains are colored according to the criterion that a single color represents a percolatively connected region within 1° (in the left image of Fig. 1.36) and within 5° (in the right image of Fig. 1.36). It is apparent from Figure 1.36 that most of the substrate is percolatively connected within 5°.

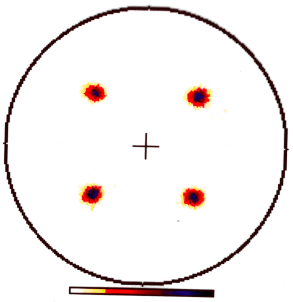

Fig. 1.35. Log-scale, background subtracted (111) pole figure of a cube-textured Ni-13 at. % Cr substrate.

Mechanical properties of these Ni-Cr substrates were measured by performing tensile tests on laser-machined, dog-bone samples. The tests were conducted in the annealed state such that the substrate had the fully developed cube texture and the [100] axis was aligned parallel to the loading axis. With increasing Cr additions, the substrates were significantly strengthened. Both the yield strength (YS) as well as the ultimate tensile strength (UTS) increased substantially and values of select alloys are summarized in Table 1.4.

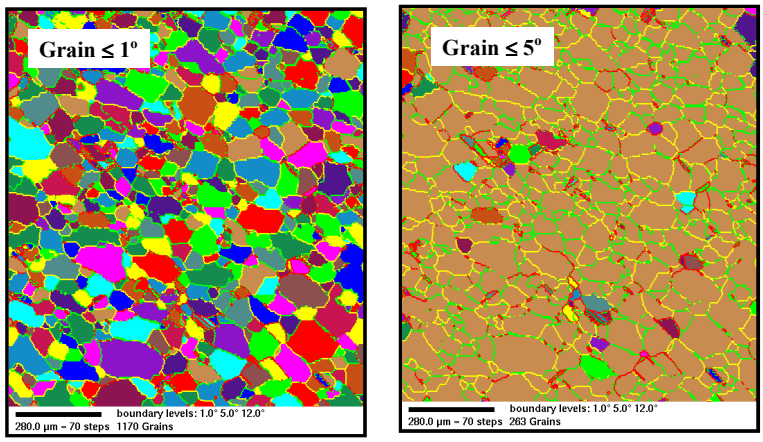

Fig. 1.36. Orientation image of textured Ni-13 at. % Cr substrate measured using electron backscatter Kikuchi diffraction. Grains are colored according to the criterion that a single color represents a percolatively connected region with 1° (left) and 5° (right).

Table 1.4. Summary of yield strength and ultimate tensile strength for Ni-Cr substrates

Substrate	YS, MPa (0.2%)	UTS, MPa
Ni	34	221
Ni-7 at. % Cr	64	304
Ni-13 at. % Cr	164	525
Ni-13 at. % Cr-4 at. % Al	228	657

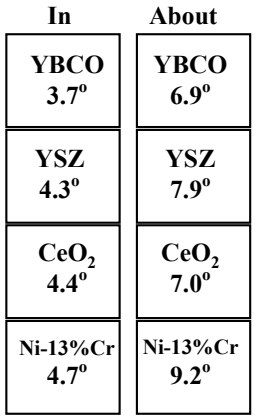

Fig. 1.37. Out-of-plane texture as measured by rocking curves or ω-scans for the various layers in the multilayer. The FWHM of the texture is indicated for each layer. Note the decrease in the FWHM in the YBCO compared with the Ni-13 at. % Cr substrate.

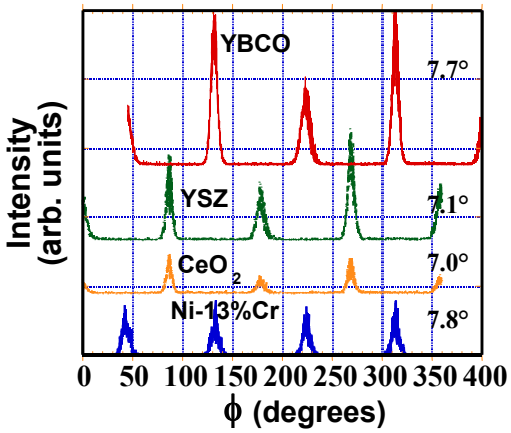

Fig. 1.38. In-plane texture as measured by ϕ-scans for the various layers in the multilayer. The FWHM of the texture is indicated for each layer. Note the similar values FWHM for each layer.

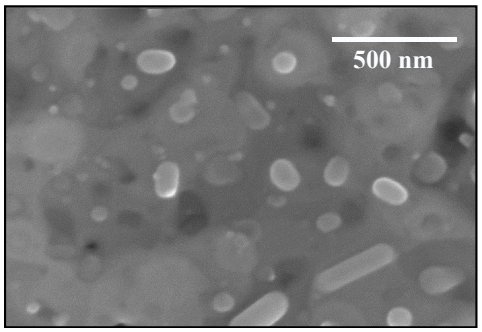

Fig. 1.39. High-magnification SEM image of the YBCO film on Ni-13 at. % Cr. A dense microstructure with no evidence of any microcracks can be seen. Second-phase particles are similar to those typically observed in YBCO films processed ex situ.

1.7.2 Oxide Multilayer Depositions on Ni-13%Cr Substrates

Multilayer oxide buffer layers of configuration CeO_2/YSZ/CeO_2 were deposited on the Ni-13 at. % substrate. The first CeO_2 layer was 100 Å thick and as deposited using e-beam evaporation. The YSZ and the final CeO_2 layer were deposited using sputtering. The YSZ layer was 4000 Å thick, and the CeO_2 cap layer was 100 Å thick.

YBCO was formed on this buffered multilayer using the ex situ BaF_2 technique. BaF_2, Cu, and Y were co-deposited on the substrate using e-beam evaporation at room temperature. The precursor film was 0.3 μm thick. This was followed by high-temperature annealing in the presence of water vapor to remove the fluorine from the precursor film and to enable the formation of the superconducting YBCO phase.

Figure 1.37 shows the out-of-plane texture of the complete multilayer assembly. It can be seen that the out-of-plane texture gets sharper in YBCO than it does in the Ni-13 at. % substrate. The texture sharpens from 4.7° to 3.7° in YBCO compared with the substrate in the rolling direction, and from 9.2° to 6.9° about the rolling direction. Figure 1.38 shows the in-plane texture of the complete multilayer assembly. As can be seen, the in-plane texture remains relatively unchanged through the structure, indicating good epitaxy. Figure 1.39 shows a high-magnification SEM image of the YBCO layer. No

evidence of any micro-cracking is observed, and the film is found to be very dense.

Resistivity vs temperature for the YBCO film on this substrate is shown in Fig. 1.40. As can be seen from the figure, the room-temperature resistivity of the film is low and the resistivity decreases linearly until the start of the superconducting transition around 90 K. Moreover, extrapolation of the resistivity above the transition to 0 K shows an intercept below zero, indicating no residual resistivity. Most HTS films that exhibit high J_cs show negligible residual resitivities.

The critical current density of the YBCO film on Ni-13 at. % Cr as a function of applied magnetic field is shown in Fig. 1.41. The data are compared to Jc vs magnetic field for YBCO films on $SrTiO_3$ and a standard Ni RABiTS™ substrate. In each case the YBCO was deposited using the ex situ BaF_2 process. The zero-field J_c at 77 K for the film on Ni-13 at. % Cr was 1.4 MA/cm^2 compared with 1.6 MA/cm^2 on Ni. The in-field J_c dependence is very similar for all the three samples. As expected, the film on single-crystal $SrTiO_3$ has a higher zero-field J_c.

Figure 1.42 shows an orientation micrograph created by electron backscatter Kikuchi diffraction showing the grain orientations in the YBCO film. The grains are colored according to the criterion that a single color represents a percolatively connected region within 5°. It is apparent from Figure 1.42 that most of the substrate is percolatively connected within 5°. This is in excellent agreement with the grain orientation images of the Ni-13 at. % Cr substrates shown in Fig. 1.36 and indicates very good epitaxy and transference of texture through the multilayer assembly.

These results indicate that the Ni-13 at. % Cr substrates are adequate for practical HTS applications and that they exhibit all of the necessary requirements of a practical substrate for applications at 77 K; they are nonmagnetic and mechanically robust, and high-critical-current-density films can be grown epitaxially on them.

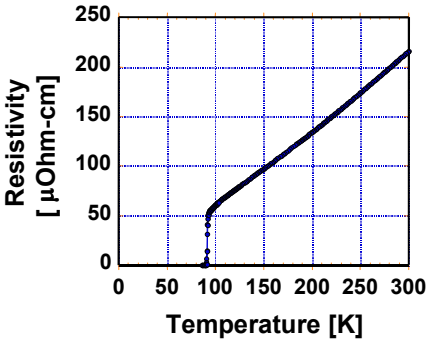

Fig. 1.40. Resistivity vs temperature for the YBCO film on Ni-13 at. % Cr. Low room-temperature resistivity, a sharp superconducting transition ~ 90 K, and no residual resistivity are apparent.

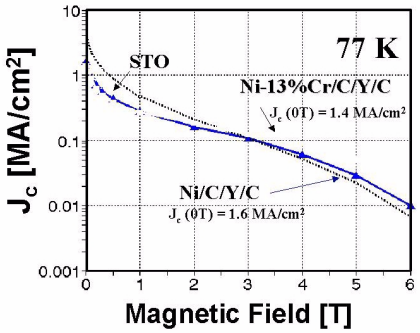

Fig. 1.41. J_c vs applied magnetic field for the YBCO film on Ni-13 at. % Cr compared with similarly processed YBCO films on $SrTiO_3$ and textured Ni substrates.

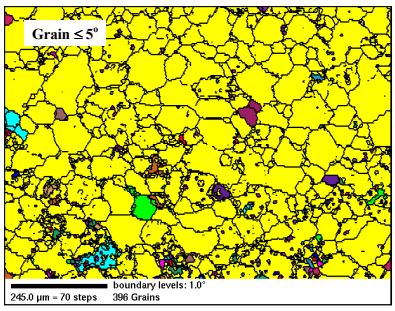

Fig. 1.42. Orientation image of the epitaxial YBCO film on Ni-13 at. % Cr measured using electron backscatter Kikuchi diffraction. Grains are colored according to the criterion that a single color represents a percolatively connected region 5°.

1.8 DEVELOPMENT OF A DEFORMABLE BIAXIALLY TEXTURED BUFFER LAYER FOR RABiTS™

D.F. Lee, M. Paranthaman, E.D. Specht, A. Goyal, and D.M. Kroeger (ORNL); G.N. Riley (American Superconductor Corporation)

Following the initial discovery of-high temperature superconductors (HTSs), a large amount of effort has been expended toward the fabrication of long, flexible conductors with high critical current densities (J_cs). One of the most important steps toward the development of practical HTSs was the fabrication by Heine et al. in 1989 of polycrystalline, silver-sheathed powder-in-tube (PIT) Bi-2212 tapes.[1] Since then, significant progress has been made in the fabrication of long lengths of Bi-2212 and Bi-2223 PIT conductors. Indeed, J_c values in excess of 70,000 A/cm^2 at 77 K and self-field have been obtained in short lengths of PIT Bi-2223 tapes (e.g., Malozemoff et al.[2]). These J_c values, however, are still much lower than those of epitaxial Bi-2223 thin films deposited on single-crystalline substrates. It has been argued that, like the J_c of other HTSs, the J_c of Bi-based superconductors is strongly dependent on grain-boundary misorientation angle. Although PIT processing of Bi-based HTS produces only a strong uniaxial texture, long-range percolative paths of low-energy grain boundaries are developed that permit the strongly linked current flow. Since the current flow is percolative, only a small fraction (~10%) of the cross section of the HTS core is active (Goyal et al.[3]), and the overall J_c is only about one-tenth of the maximum attainable J_c. On the other hand, reports on bi-crystal work suggest that in-plane alignment is not crucial to the current-carrying capability of Bi-2223 PIT conductor; the cracks generated during the forming process, which are absent in the thin-film processes, are the main current limiters. To reconcile the differing opinions, it is necessary to examine the superconducting characteristics of biaxially textured Bi-2223 conductors fabricated by a powdered-precursor approach.

Coated-conductor technique is one potential route toward the attainment of a biaxially textured Bi-2223 conductor using powdered precursors. By depositing a Bi-2223 precursor on polycrystalline Ag foils, D. F. Lee[4] and Riley et al.[5] have obtained J_c values of 40,000 A/cm^2 at 77 K. More importantly, the out-of-plane alignment of these Bi-2223 conductors has been found to be less than 10° FWHM, significantly better than that of PIT tapes. A number of technical challenges, however, have to be overcome before biaxial texture can be obtained. First and foremost is the choice of a textured substrate. For the powdered-precursor approach, mechanical densification is necessary to reduce the porosity in the precursor and to promote HTS phase formation. Consequently, single-crystal substrates cannot be used because of cracking under mechanical pressure. The remaining choices, then, are biaxially textured metal substrates such as RABiTS™ and ion-beam-assisted deposition (IBAD). Unfortunately, these substrates utilize ceramic buffer layers as diffusion barriers as well as transitional layers to obtain final HTS epitaxy. Due to the brittle nature of the ceramic buffers, cracks will be initiated and will propagate within the buffers when the substrate is subjected to mechanical pressure. During subsequent high-temperature formation of Bi-2223, these flaws will permit the diffusion of undesirable elements to the HTS as well as the formation of rough metallic oxides (Fig. 1.43), thereby disrupting HTS grain alignment and severely degrading the superconducting properties of the coated conductor.

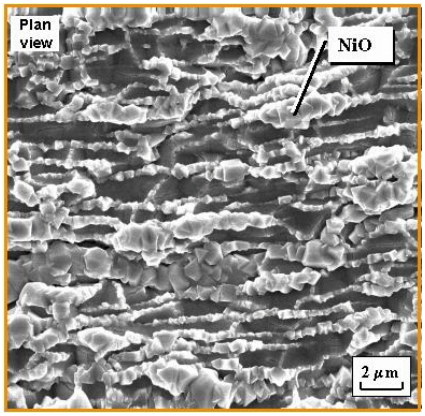

Fig. 1.43. SEM image of a YSZ/CeO_2/Ni substrate subjected to pressing and annealing in an oxidizing atmosphere. NiO particles are observed to grow through the cracks within the buffers.

We have been investigating the possibility of an alternative buffer that can circumvent the cracking problem. A suitable

candidate has to be deformable, capable of retaining the biaxial texture through deformation and subsequent heat-treatment processes, and capable of preventing Ni diffusion. If the HTS precursor is to be deposited directly onto the alternative buffer, it has an additional requirement of nonreactivity with Bi-2223. Silver has been identified as such buffer.

To investigate the ability of Ag to forego recrystallization and accompanying changes in texture, a 25-mm-thick Ag buffer was epitaxially deposited onto a biaxially textured RABiTS™. The as-sputtered Ag buffer was biaxially textured as seen in (111) Ag pole figure [Fig. 1.44(*a*)] with an out-of-plane alignment of 3.6° FWHM [Fig. 1.45(*a*)] and an in-plane alignment of 6.8° FWHM [Fig. 1.46(*a*)]. This sample was then subjected to uniaxial pressing between polished steel platens at 750 MPa pressure. An Ag pole figure of the deformed sample remained identical to that of the undeformed stage, as seen in Fig. 1.44(*b*), indicating that the biaxial texture has not been altered in the Ag buffer. The out-of-plane [Fig. 1.45(*b*)] and in-plane [Fig. 1.46(*b*)] textures were found to be 4° and 10.2° FWHM, respectively. Following pressing, the deformed substrate was subjected to heat treatment with a temperature profile typical of Bi-2223 annealing treatment. Specifically, the sample was heated to 350°C at a rate of 10°C/min in a 7.5% O_2 and 92.5% Ar gas mixture. After holding at 350°C for 1 h, the sample was heated to 825°C at a rate of
100°C/h. The sample was held at this temperature for 2 h before being furnace-cooled to room temperature. The 7.5% O_2 and 92.5% Ar oxidizing environment was maintained throughout the entire heat treatment. Figure 1.44(*c*) shows the Ag pole figure of the pressed and annealed sample, which is identical to those of both the as-pressed and the as-sputtered stages. This result indicates that the Ag buffer did not recrystallize and that the biaxial texture had not been altered. The out-of-plane texture was found to be 4.2° FWHM [Fig. 1.45(*c*)] with an in-plane texture of 8.9° FWHM, as shown in Fig. 1.46(*c*).

To demonstrate that rolling and annealing do not alter the biaxial texture of Ag buffer, a 25-μm-thick Ag buffer was epitaxially deposited onto another RABiTS™. Figure 1.47(*a*) shows the (220) Ag pole figure of the as-sputtered sample, indicating that cube-on-cube relationship with the textured substrate was maintained. Out-of-plane and in-plane alignments of the Ag buffer determined from ω-scans [Fig. 1.48(*a*)] and ϕ-scans [Fig. 1.49(*a*)] of the (200) and (220) planes are 6.4° FWHM and 10.0° FWHM, respectively. This sample was then rolled from an initial sample thickness of 150 mm to a final thickness of 141.5 mm. After rolling, Ag pole figure of the sample [Fig. 1.47(*b*)] remained identical to that of the undeformed stage, indicating that the biaxial texture has not been altered in the Ag buffer. The out-of-plane texture was found to be 6.4° FWHM [Fig. 1.48(*b*)], and the in-plane texture was determined to be 10.7° FWHM [Fig. 1.49(*b*)]. As with the pressed sample, this rolled sample was heated to 350°C in a 7.5% O_2 and 92.5% Ar gas mixture. After holding at 350°C for 1 h, the sample was heated to 825°C and held for 2 h before being furnace cooled to room temperature. The 7.5% O_2 and 92.5% Ar oxidizing environment was maintained throughout the entire heat treatment. Figure 1.47(*c*) shows the Ag pole figure of the rolled and annealed sample, which is identical to those of the as-rolled as well as the as-sputtered stages. The out-of-plane and in-plane textures of the Ag buffer were determined to be 6.4° FWHM [Fig. 1.48(*c*)] and 9.8° FWHM [Fig. 1.49(*c*)], respectively. These detailed X-ray examinations confirmed that deforming and annealing of the Ag buffer do not alter the cube-on-cube biaxial alignment that is essential in the densification of powdered precursors for the investigation of biaxially textured Bi-2223.

To summarize, we have identified a ductile metallic buffer with a stable cube texture that is maintained through deformation and subsequent annealing treatment at elevated temperatures. This favorable characteristic will enable the mechanical densification of Bi-2223 precursors without the disastrous consequences of loss of biaxial texture or failure in diffusion protection. Work is under way to examine the possible occurrence of cube-on-cube epitaxy of Bi-2223 using the powdered precursor approach.

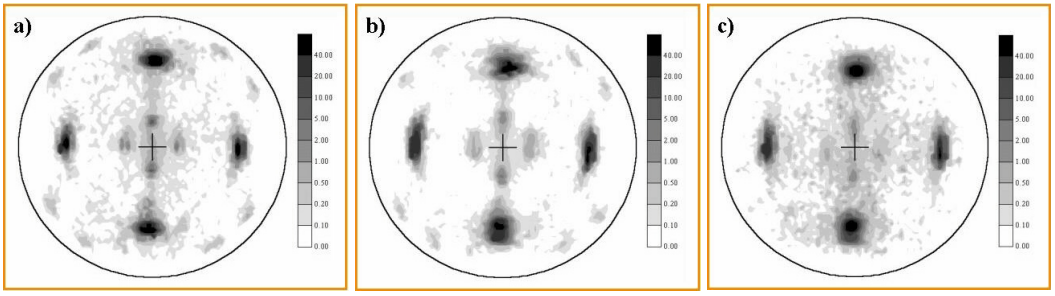

Fig. 1.44. (111) Ag pole figures. (*a*) An as-sputtered Ag buffer showing cube-on-cube biaxial texture. (*b*) The sample after uniaxial pressing; it is identical to that of the undeformed stage. (*c*) The sample after uniaxial pressing and annealing; it is identical to that of the as-pressed and as-sputtered stages, indicating that Ag cube-on-cube texture is preserved after pressing and annealing.

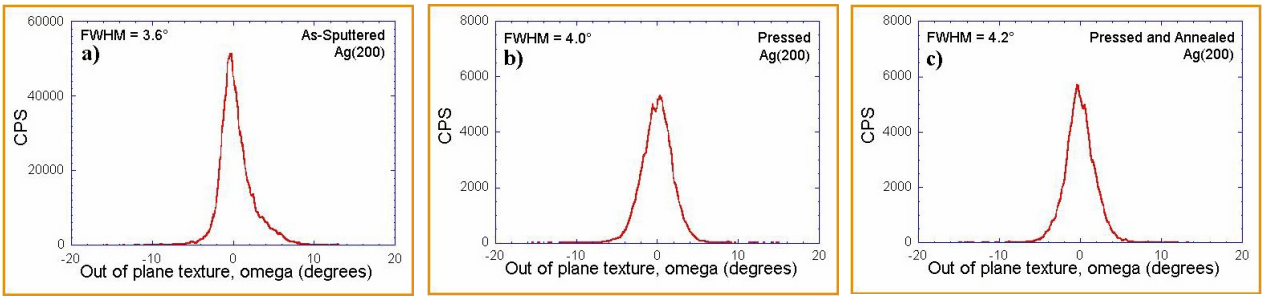

Fig. 1.45. Out-of-plane texture of the (200) Ag plane. (*a*) On the as-sputtered sample shown in Fig. 1.44(*a*) with a FWHM of 3.6°. (*b*) On the pressed sample shown in Fig. 1.44(*b*) with a FWHM of 4°. (*c*) On the pressed and annealed sample shown in Fig. 1.44(*c*) with a FWHM of 4.2°.

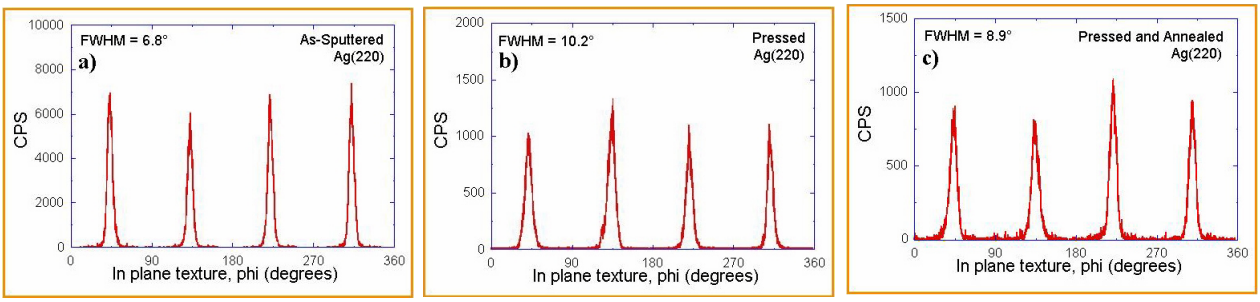

Fig. 1.46. In-plane texture of the (220) Ag plane. (*a*) On the as-sputtered sample shown in Fig. 1.44(*a*) with a FWHM of 6.8°. (*b*) On the pressed sample shown in Fig. 1.44(*b*) with a FWHM of 10.2°. (*c*) On the pressed and annealed sample shown in Fig. 1.44(*c*) with a FWHM of 8.9°.

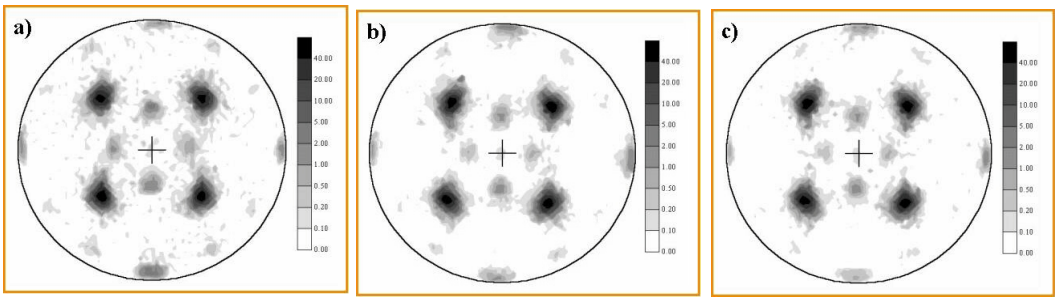

Fig. 1.47. (220) Ag pole figures. (*a*) An as-sputtered Ag buffer showing cube-on-cube biaxial texture. (*b*) After rolling; it is identical to that of the undeformed stage. (*c*) The sample after rolling and annealing; it is identical to that of the as-rolled and as-sputtered stages, indicating that Ag cube-on-cube texture is preserved after rolling and annealing.

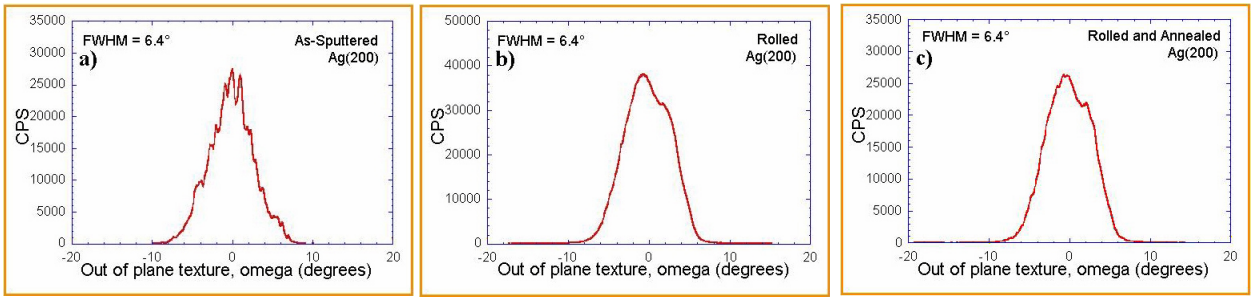

Fig. 1.48. Out-of-plane texture of the (200) Ag plane. (*a*) On the as-sputtered sample shown in Fig. 1.47(*a*) with a FWHM of 6.4°. (*b*) On the rolled sample shown in Fig. 1.47(*b*) with a FWHM of 6.4°. (*c*) On the rolled and annealed shown in Fig. 1.47(*c*) with a FWHM of 6.4°.

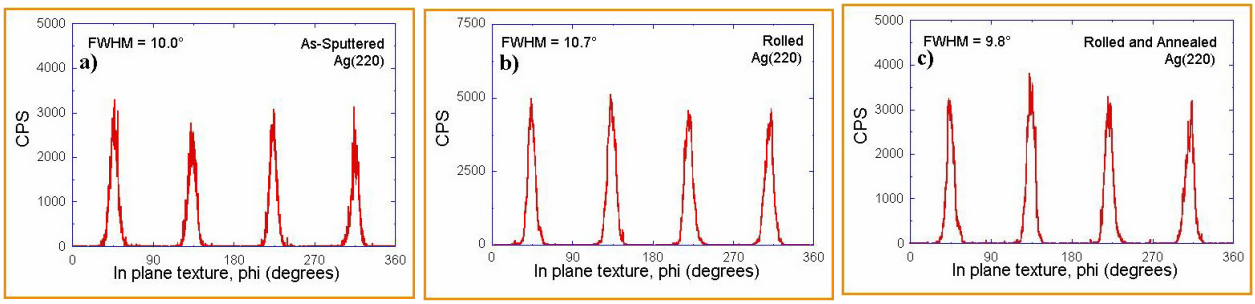

Fig. 1.49. In-plane texture of the (220) Ag plane. (*a*) On the as-sputtered sample shown in Fig. 1.47(*a*) with a FWHM of 10.0°. On the rolled sample shown in Fig. 1.47(*b*) with a FWHM of 10.7°. (*c*) On the rolled and annealed sample shown in Fig. 1.47(*c*) with a FWHM of 9.8°.

1.8.1 References

1. K. Heine, J. Tenbrink, and M. Thoner, "High-Field Critical Current Densities in $Bi_2Sr_2Ca_1Cu_2O_{8+x}$/Ag Wires," *Appl. Phys. Lett*. **55**(23), 2441 (1989).

2. A. P. Malozemoff et al., "HTS Wire at Commercial Performance Levels," *IEEE Trans. Appl. Supercond*. **9**(2), 2469–73 (1999).

3. A. Goyal et al., "Grain Boundary Misorientations and Percolative Current Paths in High-J_c Powder-in-Tube $(Bi,Pb)_2Sr_3Ca_3Cu_3O_x$," *Appl. Phys. Lett*. **66**(21), 2903–2905 (1995).

4. D. F. Lee, "An Alternative Approach: BSCCO Coated-Conductor Development," pp. 422–39 in Proc. *1998 DOE Superconductivity Program for Electric Systems Annual Peer Review*, Vol. 2, 1998.

5. G. N. Riley et al., "BSCCO Coated-Conductor Development," pp. 65–74 in *Proc. 1999 DOE Superconductivity Program for Electric Systems Annual Peer Review*, Vol. 1, 1999.

1.9 PROGRESS IN SCALING UP YBCO-COATED CONDUCTOR ON RABiTS™ USING THE BaF_2 PRECURSOR APPROACH

D.F. Lee, F.A. List, X. Cui, P.M. Martin, E.D. Specht, A. Goyal, D.M. Kroeger, and M. Paranthaman (ORNL); W.B. Robbins (3M)

Since the inception of the Rolling Assisted Biaxially Textured Substrate (RABiTS™) approach at ORNL, ample results have demonstrated that high-quality biaxially textured YBCO-coated conductors can be obtained on these flexible substrates. High-J_c values ranging from 1 to 3 MA/cm^2 at 77 K and self-field have been obtained in short lengths (~ 1cm) for YBCO deposition by both the in situ (e.g., pulsed-laser deposition) and ex situ (e.g., BaF_2 precursor) methods. Scalability of the various steps in the preparation of a RABiTS™-type conductor is presently being addressed. Utilizing information gained from short-length results, we have been examining the issues related to scaling up YBCO on RABiTS™ with the BaF_2 precursor method.

For the BaF_2 precursor method, the CeO_2/YSZ/CeO_2/Ni RABiTS™ architecture has resulted in J_cs in excess of 2.3 MA/cm^2 (R. Feenstra et al., unpublished) and is the architecture used in this work (Fig. 1.50). Meter-long lengths of Ni were annealed, and the first 300-Å-thick CeO_2 buffer layer was deposited by reactive sputtering at 3M in a moving configuration. The fast deposition rate of reactive sputtering resulted in a dense and smooth CeO_2 buffer (Fig. 1.51) with rapid sample throughput. Both the out-of-plane and in-plane textures of the CeO_2 buffer, however, are wider than those of the textured Ni (Fig. 1.52). Further optimization of deposition parameters is being performed to improve the buffer textures.

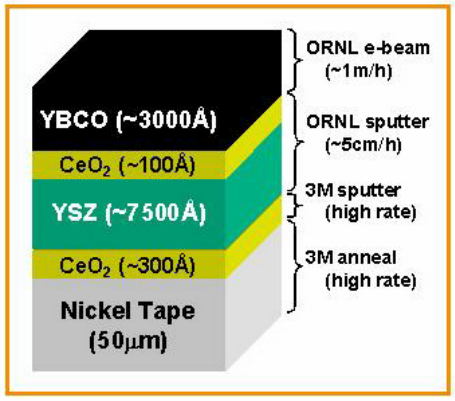

Fig. 1.50. RABiTS™ architecture used in the present work to examine the scaling up of YBCO on RABiTS™ by the BaF_2 precursor approach.

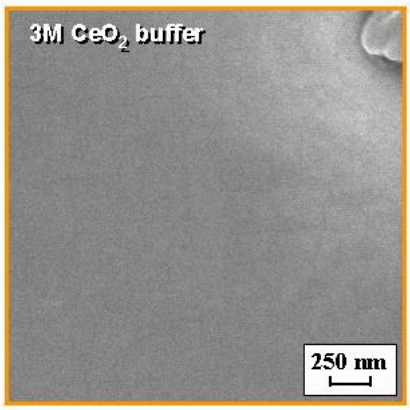

Fig. 1.51. SEM image of dense and smooth CeO_2 buffer layer deposited by high-rate reactive sputtering.

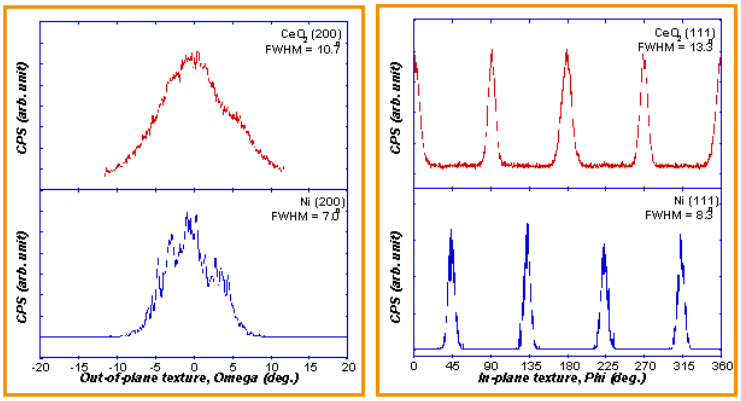

Fig. 1.52. Out-of-plane and in-plane textures of Ni and CeO_2 buffer deposited by high-rate reactive sputtering.

Subsequent CeO_2/YSZ buffers were deposited on these buffered tapes at ORNL using a reel-to-reel rf magnetron sputtering system in a moving configuration (Fig. 1.53). During buffer deposition, the moving tape glides over 6-in. heating blocks that are situated above the sputtering guns. Because the tape is not heated from end to end, the entire tape is shielded except for 3-in.-wide openings centered at each heating block. The purpose of the shields is to avoid any accidental deposition of materials onto portions of the tape not heated to the desired temperature, which usually leads to incorrect and irreversible textures. This consequence is demonstrated in Fig. 1.54 which shows the θ-2θ scans of a 50-cm tape not subjected to shielding during deposition; at the start of deposition, YSZ buffer deposited onto the leading end of the tape, which is in contact with the heater, is *c*-axis textured. The trailing end shows substantial (111) peak, owing to undesired deposition of YSZ onto the area while it is out of position and at a lower temperature. With adequate shielding, however, the problem is circumvented (Fig. 1.54).

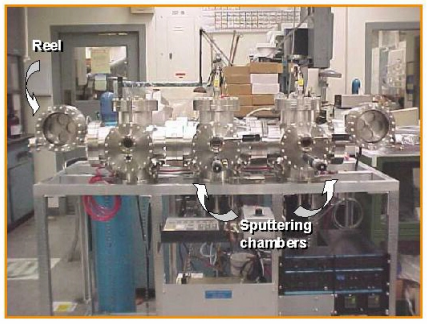

Fig. 1.53. Reel-to-reel rf magnetron sputtering system for buffer deposition.

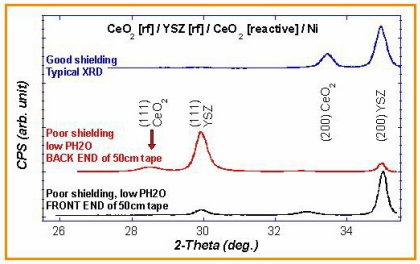

Fig. 1.54. The θ-2θ scans of YSZ and CeO_2 buffers deposited with and without shielding during rf sputtering of YSZ.

It was also found that buffer delamination at the CeO_2/Ni interface frequently occurred when an atmosphere of 98% Ar and 4% H_2 was the only atmosphere provided during YSZ sputtering (Fig. 1.55). The θ-2θ scans of delaminated tapes revealed that oxygen stoichiometry of the initial CeO_2 layer had changed during YSZ deposition (Fig. 1.56). It is believed that, because of the longer deposition time required for long lengths, background oxygen within the deposition chamber was depleted to a much greater extent, leading to out-diffusion of oxygen from CeO_2 to the YSZ buffer. This can result in stress development within the CeO_2 buffer and eventually leads to delamination. In order to avoid buffer delamination, a low level of H_2O was provided as an oxygen source during YSZ sputtering. Figure 1.56 indicates that H_2O is effective in preventing buffer delamination without oxidizing the Ni substrate.

A 5000-Å-thick YSZ buffer and a 300-Å-thick CeO_2 cap layer were deposited onto the CeO_2/Ni tapes from 3M at 650°C and at a tape speed of roughly 5cm/h. Out-of-plane and in-plane textures of sections of these RABiTS™ were examined by X ray. Figure 1.57 shows the results of ω and ϕ scans from one such section. Scans were obtained at 1-cm increments and revealed that both out-of-plane and in-plane textures

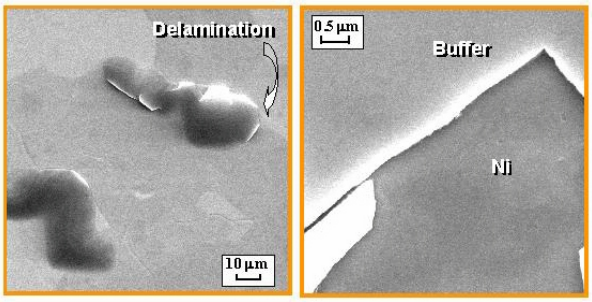

Fig. 1.55. SEM images of buffer delamination for rf magnetron sputtering in the absence of H_2O.

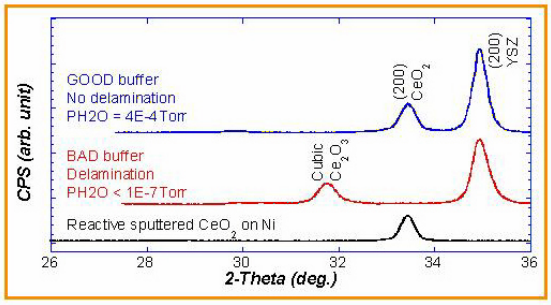

Fig. 1.56. The θ-2θ scans of YSZ and CeO_2 buffers deposited with and without a source of H_2O.

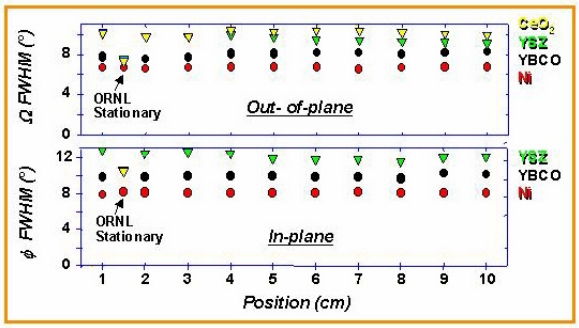

Fig. 1.57. Out-of-plane and in-plane textures of a 12-cm-long moving YBCO (BaF_2)/ CeO_2 (rf sputtered)/YSZ (rf sputtered)/CeO_2 (reactive sputtered)/Ni tape. Also included is the texture information of its stationary counterpart.

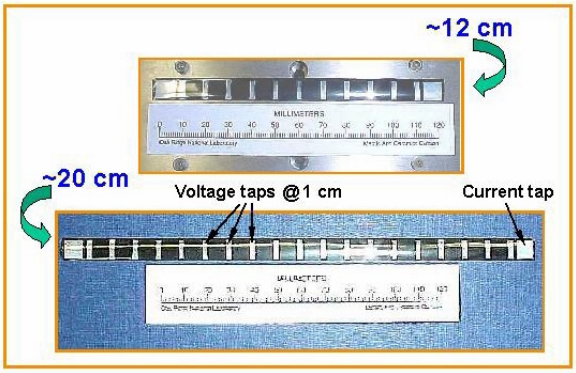

Fig. 1.58. 12- and 20-cm-long samples following BaF_2 conversion and oxygen annealing. Samples appear to be shiny, black, and uniform.

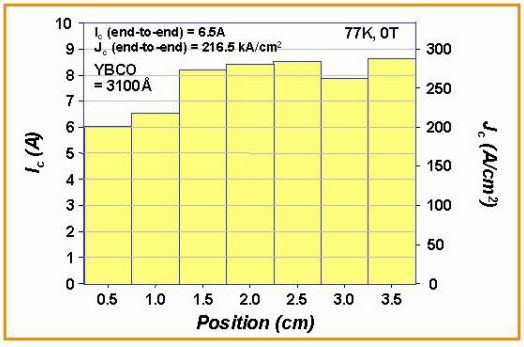

Fig. 1.59. J_c distribution of a 5-cm sample. Total voltage separation is 3.5 cm.

of these tapes were uniform along the length. While the uniformity of texture was excellent, the FWHMs of the moving buffers were typically about 2° wider than those of their stationary counterparts. This broadening of the buffer textures is believed to originate from the first CeO_2 buffer, and the texture should improve once the reactive sputtering parameters are optimized.

Following buffer depositions, a BaF_2 precursor was deposited on the fully buffered tapes in a moving configuration using our reel-to-reel e-beam system[1]. Briefly, the BaF_2 precursor was deposited without tape heating in this 3-gun, 3-pocket system using Y, BaF_2 and Cu sources at a deposition rate and tape speed of roughly 10 Å/s and 1 m/h, respectively. BaF_2 precursor deposited on these tapes looked shiny, black, and uniform.

YBCO conversion was performed in our stationary extended-zone reaction chamber. Due to the incomplete reaction observed by R. Feenstra et al.[2] in their longitudinal-flow reaction chamber, this extended-zone chamber was constructed so as to provide a transverse-flow geometry. The length of the reaction zone in this furnace is 30 cm, with a temperature uniformity of roughly ±2.5°C. Samples measuring 5, 12, and 20 cm long by 1 cm wide were individually placed in the center of the reaction zone and were heat-treated under identical conditions. Briefly, each sample was heated to 740°C at a ramp rate of ~ 23°C/min in flowing 180-ppm oxygen gas (balance N_2) that was bubbled through 40°C H_2O. After holding at this temperature for 3 h, the annealing gas was reverted to a dry condition, and the sample was annealed for another 0.5 h before cooling down to room temperature. Then, Ag current and voltage taps were sputtered on the samples, and the samples were oxygen annealed for 1 h at 500°C. Figure 1.58 shows the appearance of the 12- and 20-cm-long samples. These samples appear shiny, black, and uniform. As seen in Fig. 1.57, YBCO out-of-plane and in-plane textures are uniform with FWHM of roughly 8° and 10°, respectively. Figure 1.59 shows the I_c and J_c distribution of a 5-cm-long sample with a 3.5-cm voltage tap separation. The J_c values of individual 0.5-cm sections ranged between 200,000 and 280,000 A/cm^2 at 77 K, with an end-to-end J_c of 216,500 A/cm^2. These J_cs are comparable to those of short (1-cm) samples with similar textures, which

typically vary from 200,000 to 400,000 A/cm^2. Figures 1.60 and 1.61 show the J_c values of the 12- and 20-cm-long samples, with end-to-end J_cs of 180,000 and 82,300 A/cm^2, respectively. Although it appears that the J_cs are lower and less uniform, it is important to note that the processing conditions were identical to those of the 5-cm sample, thus justifying the utilization of a transverse-flow geometry. When another 5-cm-long sample with a slightly richer Ba content was subjected to the same heat treatments (Fig. 1.62), the end-to-end J_c was determined to be 540,000 A/cm^2 with a maximum value of 630,000 A/cm^2 and an excellent ±7% standard deviation. To further address issues concerning the uniformity and scaling up of BaF_2 precursor conversion, we are currently developing a multi-zoned reel-to-reel transverse-flow reaction chamber, which will be reported in the future.

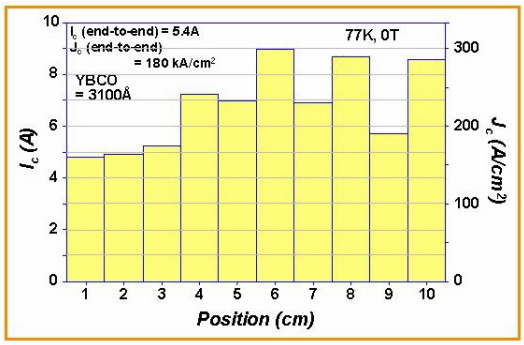

Fig. 1.60. J_c distribution of a 12-cm sample. Total voltage separation is 10 cm.

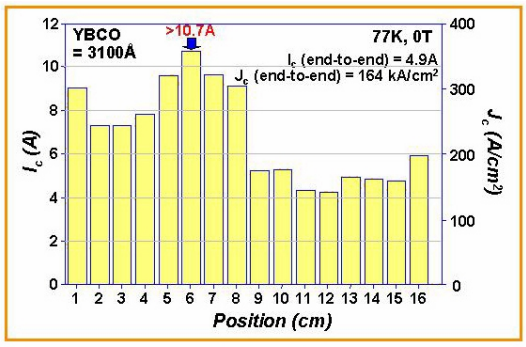

Fig. 1.61. J_c distribution of a 20-cm sample. Total voltage separation is 18 cm.

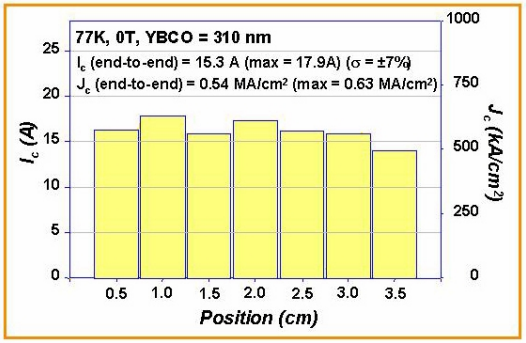

Fig. 1.62. J_c distribution of a 5-cm Ba-rich sample. Total voltage separation is 3.5 cm.

1.9.1 References

1. X. Cui et al., "Continuous Deposition of Ex-Situ Processed YBCO Precursor Films on Rolling-Assisted Biaxially Textured Substrates by Electron Beam Evaporation," *Physica C* (submitted).

2. R. Feenstra et al., "An Ex-Situ Processed YBCO Coated Conductor," pp. 361–84 in *Proc. 1999 DOE Superconductivity Program for Electric Systems Annual Peer Review*, Vol. 1, 1999.

1.10 PROGRESS TOWARD CONTINUOUS PROCESSING OF YBCO/RABiTS™ TAPE

F. A. List

Processing of YBCO/RABiTS™ tape of lengths greater than ~1 m generally requires techniques and equipment that are compatible with tape motion from one spool to another. In order to assist our cooperative research and development (CRADA) partners in resolving scale-up issues, a complete line of so-called "roll-to-roll" equipment is being developed at ORNL to process and characterize YBCO/

RABiTS™ tape of lengths up to ~2 m. This equipment includes capabilities for

- cleaning as-rolled metal tape,
- annealing metal tape to develop texture,
- reacting the BaF_2 precursor to form YBCO,
- depositing silver on YBCO/RABiTS™ tape,
- characterizing tape by X-ray diffraction, and
- measuring critical current (I_c) of tape.

Common to all this equipment is a roll-to-roll tape-handling system. A micro-stepper motor drives a pay-out spool and determines, through open-loop control, the tape position, speed, and direction. Tape speeds are dictated by the process and can range from 10^{-3} to 10^3 m/h. A bidirectional torque motor drives a take-up spool and provides tape tension.

Figure 1.63 shows a drawing of the equipment used for cleaning as-rolled metal tape. The roll-to-roll cassette is submerged halfway into an ultrasonic bath, and tape is cleaned while it travels between spools.

Figure 1.64 shows a drawing of the vacuum system used for both annealing metal tape and e-beam evaporating of buffer layers. The pay-out and take-up spools are mounted inside the vacuum system of ferro-fluid vacuum feedthroughs. Noncontact annealing of tape is accomplished by thermal radiation from an rf-heated tantalum tube mounted coaxially to the tape. Annealing temperatures up to ~1200°C are expected with this system.

Reaction of BaF_2 precursor to form YBCO occurs in a vacuum-compatible system that is equipped with a roll-to-roll tape-handling system. Gas is preheated and flows perpendicularly to the tape length, both to and from perforated manifolds. Temperature of the reacting tape is controlled with a 22-zone, 2-m furnace.

Silver is dc-sputter-deposited on moving YBCO/RABiTS™ tape in a roll-to-roll-compatible vacuum system. Silver is required for good electrical contact to the YBCO. Tape speeds of ~1m/h are expected for deposition of a 2-μm layer of silver.

Figure 1.65 shows a sketch of the roll-to-roll tape transport system used for X-ray texture determinations of metal tape, buffered tape, and YBCO/RABiTS™ tape. This system is mounted in the chi circle of a four-circle goniometer and includes a rotating Cu anode X-ray source. For any point along a 20-m tape, θ-2θ, ϕ, and ω scans typically require 2 min each, and a

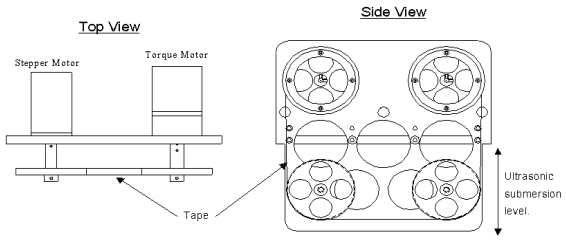

Fig. 1.63. Drawing of the equipment used for cleaning as-rolled metal tape.

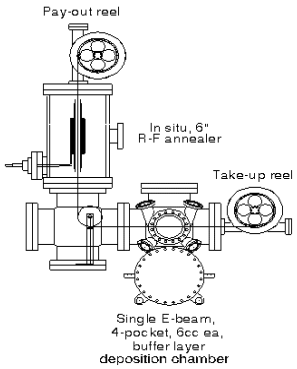

Fig. 1.64. Drawing of the vacuum system used for annealing metal tape and e-beam evaporating of buffer layers.

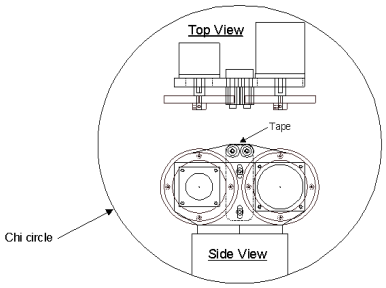

Fig. 1.65. Sketch of the roll-to-roll tape transport system used for X-ray texture determinations of metal tape, buffered tape, and YBCO/RABiTS™ tape.

complete pole figure requires ~30 min. For fixed diffraction geometry, X-ray tape scans are obtained for tape speeds ~5 cm/s. To date, ~140 m of buffered tape have been characterized with this system.

Figure 1.66 shows a drawing of the equipment used for measuring transport I_c at 77 K for YBCO/RABiTS™ tape. The roll-to-roll cassette is submerged halfway into a liquid nitrogen bath, and transport I_c is measured for points along a tape by engaging a dc four-point probe assembly. Noncontact ac determination of I_c at 77 K can be accomplished on a moving tape by exchanging the probe assembly.

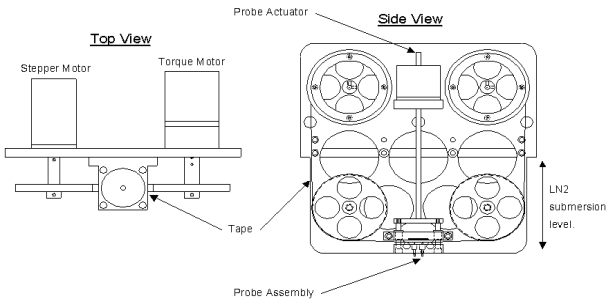

Fig. 1.66. Drawing of the equipment used for measuring transport I_c at 77 K for YBCO/RABiTS™.

When fully developed, the roll-to-roll equipment will enable continuous processing and characterization of YBCO/RABiTS™ tape of lengths up to ~2 m at ORNL. With this capability, issues of scale-up can be directly addressed for the first time.

1.11 GROWTH AND SUPERCONDUCTING PROPERTIES OF $YBa_2Cu_3O_{7-\delta}$ FILMS ON CONDUCTIVE $SrRuO_3$ AND $LaNiO_3$ MULTILAYERS FOR COATED-CONDUCTOR APPLICATIONS

T. Aytug, J. Z. Wu, C. Cantoni, D.T . Verebelyi, E. D. Specht, M. Paranthaman, D. P. Norton, D.K. Christen, R. E. Ericson, and C. L. Thomas.

A key issue in the RABiTS™ approach to coated-conductor development is the necessity to use buffer-layer structures that are compatible with both the underlying metal substrate, Ni or Ni alloy, and YBCO. To date, buffer-layer studies have mainly concentrated on insulating oxides, and the preferred architecture in RABiTS™ technology is a combination of YSZ and CeO_2. In these types of conductors the HTS film is not electrically coupled to the underlying metallic substrate. The insulating intermediate layer does not affect the performance of relatively short samples; however, the development of a totally electrically connected structure is very important for potential high-power applications of coated conductors. In practical long-sample applications (e.g., magnets, transport cables), thermally activated flux-flow during temperature instability transients can lead to sufficient heat generation to cause transition of the superconductor to the normal state. If the superconducting layer is electrically connected to the Ni substrate, the heat dissipation above J_c will be greatly reduced because a significant portion of the current will flow in the Ni tape for $J>J_c$.

In recent years, thin films of conductive oxides [$SrRuO_3$ (SRO), and $LaNiO_3$ (LNO)] have attracted considerable interest due to their potential for many technological applications. Both SRO and LNO are perovskite-type, conductive metallic oxides with pseudocubic lattice parameters of 3.93 Å and 3.83 Å with room-temperature resistivities of 280 μΩ cm and 540 μΩ cm, respectively. These values are close to those of orthorhombic YBCO and other high-temperature superconductors. It has been found that high-quality epitaxial YBCO thin films having high superconducting transition temperatures (T_c = 91 K) and high critical current densities ($J_c = 2 \times 10^6$ A/cm^2 at 77 K) can be grown on SRO-buffered single-crystal substrates. However, to date there have not been any reports on the successful growth of SRO layers on textured metals for the development of YBCO-based coated conductors. On the other hand, He et al.[1] recently reported growth of YBCO films on highly textured LNO buffer layers successfully deposited onto Ni tapes. These YBCO films showed suppressed T_c values around 75 to 80 K, consistent with earlier results of YBCO films on LNO-buffered single-crystal substrates. The observations that SRO is compatible with YBCO and that LNO can be successfully grown on Ni have motivated the present study of

SRO/LNO multilayers for application as a conductive buffer-layer structure for YBCO-based coated conductors. In this report, we have made a comparative study of the structural and the superconducting properties (T_c, J_c) of YBCO films grown on multilayers of SRO/LNO and on single-layer LNO, SRO. The substrates used were (100)-oriented $LaAlO_3$ (LAO) and $SrTiO_3$ (STO) single crystal, as well as textured Ni (100) metal tapes.

The deposition of LNO buffer layers was performed with a rf-magnetron sputtering system using a single-phase LNO powder target, which was pressed into a 95-mm copper tray. Typical sputtering conditions consisted of a mixture of Ar and O_2 at a ratio of $Ar:O_2 = 15:2$, with a total pressure of 10 mTorr. The substrate temperature was in the range of 550 to 600°C for films deposited on single crystals and 400 to 450°C for films deposited on textured Ni. In the latter case an increase in the substrate temperature caused formation of NiO at the LNO interface and nucleation of LNO grains with orientation different from the (100). The deposition rate was ~0.42 Å/s with a corresponding film thickness of about 3000 Å. Pulsed laser deposition (PLD) was employed for the deposition of SRO as well as the YBCO films. A KrF excimer laser system that was operated with an energy density of ~3 J/cm^2 was used. During the deposition of SRO layers the substrates were kept at 600°C in an O_2 atmosphere of 5 mTorr for films deposited on STO, LAO, or LNO/Ni, and 0.5 mTorr for films deposited on bare Ni. The deposition of YBCO films was achieved at 780°C in 100 mTorr of O_2. After deposition, the O_2 pressure inside the PLD chamber was increased to 500 Torr and the films were then cooled to room temperature at a rate of 10°C/min. Typical film thicknesses for SRO and YBCO were 2000 Å and 3000 Å, respectively. The structures of the films were characterized with a Huber high-resolution X-ray diffractometer. A standard four-probe technique was used to evaluate the electrical properties of the samples. The values of J_c were assigned using a 1-mV/cm criterion. Silver contacts were deposited onto the samples using dc-magnetron sputtering followed by an O_2 annealing in 1 atm for 30 min at 500°C. Secondary ion mass spectrometry (SIMS) depth profile and inductively coupled plasma (ICP) analysis of the samples were also made to document possible cation contamination of the YBCO.

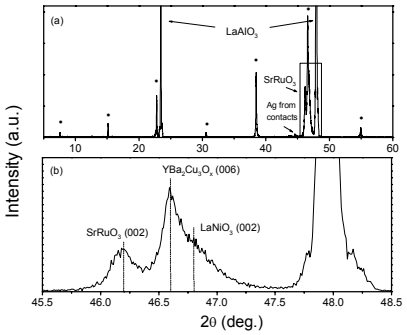

Fig. 1.67. An XRD θ-2θ scan for YBCO/SRO/LNO/LAO multilayer (*a*). YBCO (00l) peaks are indicated by (•). The weak Ag peak is due to electrical contacts. The LNO(002) scattering can be seen from the enlargement of the boxed region (*b*).

An X-ray diffraction (XRD) θ-2θ spectrum for a typical YBCO film on SRO/LNO/LAO multilayer structure is shown in Fig. 1.67(*a*). The pattern indicates only (00*l*) reflections from both the YBCO and SRO layers, demonstrating that the YBCO/SRO/LNO are c-axis-oriented. The LNO (002) reflection can be seen as a shoulder on the YBCO (006) peak from the enlargement of the boxed region, as shown in Fig. 1.67(*b*). The epitaxial relation of YBCO films on the substrates is determined by XRD pole figure analysis. The (102) pole figure of a YBCO film on SRO/LNO/LAO, shown in Fig. 1.68, indicates a single epitaxy with YBCO(001)// substrate(001) and YBCO(110)//substrate(110). Similar crystallographic relations were observed for the YBCO/SRO/LNO/ STO, YBCO/LNO/(LAO and STO) and YBCO/SRO/LAO multilayer structures.

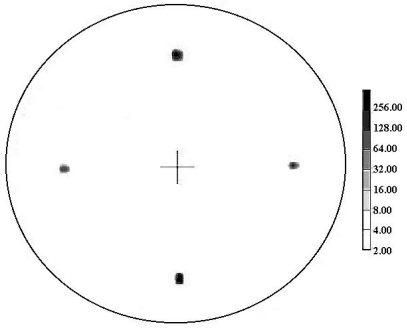

Fig. 1.68. The (102) pole figure of YBCO grown on SRO/ LNO/LAO multilayer.

The LNO films grown on textured Ni also showed single (100) orientation and very good grain alignment, as shown in the pole

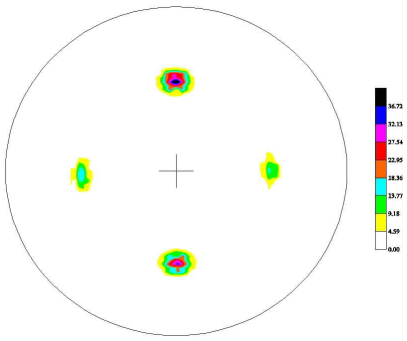

Fig. 1.69. The (111) pole figure of an LNO film grown on textured Ni.

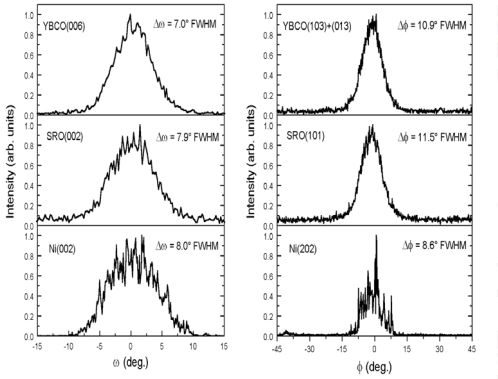

Fig. 1.70. Rocking curves for the Ni(002), SRO(002), and YBCO(006) peaks. ϕ-scans for the Ni(202), SRO(101), and YBCO(103)+(013) peaks of a YBCO/SRO/LNO/Ni sample.

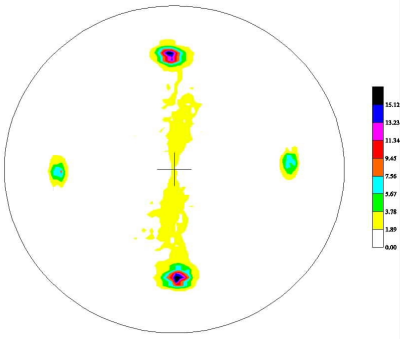

Fig. 1.71. Pole figure of the (102) reflection for a YBCO film grown on a RABiTS™ with the following structure: SRO/LNO/Ni.

figure for the LNO (111) reflection of a LNO/Ni sample (Fig. 1.69). The FWHM values for the in-plane and out-of-plane distribution of the LNO layer are comparable with those of the Ni substrate, and the epitaxial relation between Ni and LNO is cube-on-cube. Figure 1.70 shows the in-plane and out-of-plane epitaxial relations between YBCO, SRO, and the Ni substrate in a sample with the structure YBCO/SRO/LNO/Ni. Figure 1.71 is the YBCO (102) pole figure for the same sample. The YBCO film deposited on this multilayer structure has a single *c*-axis orientation with values of Δω and Δϕ typical of a good performance film on RABiTS™.

The differences in electrical and superconducting properties of the multilayer samples can be seen from the temperature-dependent resistivity curves of samples deposited on insulating single-crystal substrates (see Fig. 1.72). The inset shows an enlarged view of the transition region. For comparison, the result of a YBCO film on a STO substrate is included. Figure 1.72 shows the net resistivity (ρ_{net}), which is calculated from the total thickness of the conductive structure (YBCO + buffer layers). It is clear that an additional SRO buffer layer on LNO/(LAO and STO) improves the superconducting properties of the YBCO films by increasing T_c and decreasing ρ_{net}. The T_c of the YBCO/SRO/LNO/(LAO and STO) samples was observed to be higher than 90 K, being close to the T_c=92 K and 91 K values of the YBCO films grown on single-crystal STO

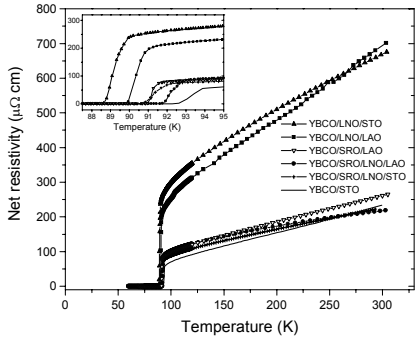

Fig. 1.72. Temperature dependence of the net resisitivity of YBCO/SRO/LNO/(LAO and STO), YBCO/LNO/(LAO and STO), YBCO/SRO/LAO, and YBCO/STO structures. Inset shows the enlarged view of the superconducting transition region.

and SRO buffered LAO substrates, respectively. However, T_cs of the YBCO/LNO/(LAO and STO) were lower than 90 K, with normal-state ρ_{net} being 3 to 4 times higher than those of YBCO/SRO/LNO/(LAO and STO). The differences in these results suggest the possible Ni contamination of the YBCO films from the LNO layers. In fact, SIMS depth profile measurements and ICP analysis of YBCO/LNO/(LAO and STO) samples qualitatively confirmed the presence of Ni in the YBCO. It is well known that Ni impurities in the superconducting structure can significantly reduce T_c and increase ρ. The T_c of YBCO films deposited on RABiTS™ with the structure LNO/Ni was particularly low, typically more than 10 K lower than in YBCO films deposited on LNO/(LAO and STO). The highly suppressed T_c indicates that diffusion of Ni into the YBCO is enhanced when the YBCO and the LNO are deposited on the Ni substrate, which acts as an infinite Ni reservoir.

The expression for the resistivity ratio, ρ_{net}/ρ_Y, of an electrically connected bilayer structure can be given by $\rho_{net}/\rho_Y = [(A_Y + A_B)/(A_Y + (\rho_Y/\rho_B)A_B)]$, where A_Y, ρ_Y and A_B, ρ_B are the cross-sectional areas and the resistivities of the YBCO and the conductive buffer-layer structures, respectively. According to this expression, ρ_{net}/ρ_Y is always >1 if $\rho_B > \rho_Y$, and <1 if $\rho_B < \rho_Y$. Because rY ≈ 300 μΩ cm and $\rho_{SRO} \approx \rho_{LNO} \approx \rho_Y$, we should expect $\rho_{net} \approx \rho_Y$. Indeed, in contrast to YBCO films on LNO layers where Ni contamination is an issue, the fact that ρ_{net} of the YBCO/SRO/LNO multilayer is similar to ρ_{net} of the YBCO on STO, and comparable to the one on SRO/LAO, is an indication of excellent electrical contact among all three layers. Also, the T_c values of samples on LAO substrates appear to be ≈ 2 K higher than those of samples on STO substrates, suggesting that LAO serves as a marginally better substrate for growth of such buffer-layer structures. Confirmation of this effect needs further investigation.

Figure 1.73 shows the magnetic field dependence of the transport J_c for the multilayers grown on single-crystal substrates at 77 K, with the field applied parallel to the *c*-axis. At zero applied field, all samples support high $J_c \geq 1.0 \times 10^6$ A/cm^2, with irreversibility fields (H_{irr}) ≥ 6 T. Consistently high J_c performance was observed for samples on SRO layers. Specifically, the self-field J_c of the YBCO/SRO/LNO/LAO is near 4.4×10^6 A/cm^2 with a high H_{irr} of 7.5 T (data not shown in plot for consistency). These values are comparable to those of the benchmark films of YBCO/STO ($J_c = 4.4 \times 10^6$ A/cm^2, H_{irr} = 8 T), and confirms high-quality epitaxial growth of YBCO on SRO/LNO multilayers. However, the YBCO/LNO/(LAO and STO) multilayer structures showed somewhat lower J_c values (1.4×10^6 and 1×10^6 A/cm^2) with $H_{irr} \cong 6$ T. This is also consistent with the lower T_c values observed for the YBCO films on LNO layers. These results further support the low-level contamination of YBCO through LNO layers. It should also be mentioned that, similar to the observations made in the ρ_{net} vs T data, J_c values of YBCO films on LAO substrates are also slightly higher than those on STO substrates.

The SRO/LNO buffer-layer architecture also provided a good template for subsequent YBCO growth when deposited on textured Ni. Figure 1.74 shows the J_c dependence on magnetic field at 77 K of a YBCO/SRO/LNO/Ni sample, compared with the J_c dependence of a YBCO film on STO and a YBCO film grown on RABiTS™ with the usual architecture CeO_2/YSZ/CeO_2. The critical current in self-field is 620 KA/cm^2, and the irreversibility field is 7.5 T. We observe that the critical current in the YBCO/SRO/LNO/Ni sample is reduced by a factor of 3 to 4 with respect to the sample with standard architecture. However, SEM analysis of the surface shows good morphology, very similar to that of YBCO films on STO

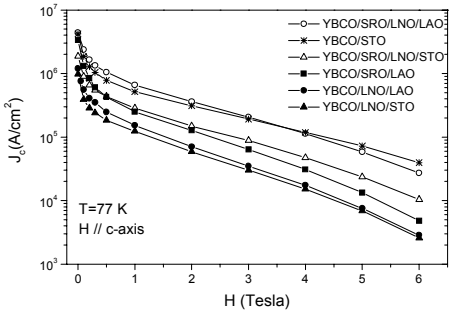

Fig. 1.73. Magnetic field dependence of J_c of YBCO/SRO/LNO/(LAO and STO), YBCO/LNO/(LAO and STO), and YBCO/SRO/LAO multilayers at 77 K. For comparison, J_c data of YBCO/STO is also included.

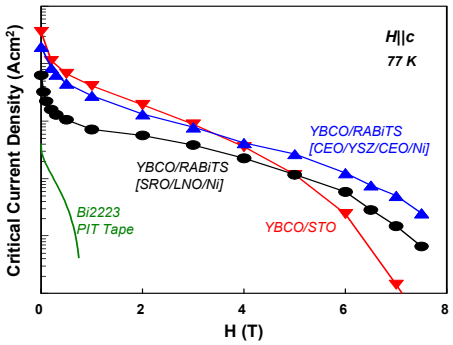

Fig. 1.74. Comparison between J_c dependencies on magnetic field for YBCO/SRO/LNO/Ni, YBCO on conventional RABiTS™, YBCO/STO, and a Bi-2223 PIT tape.

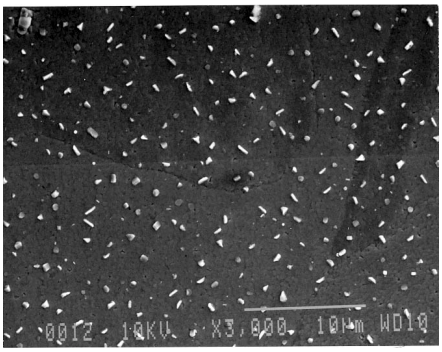

Fig. 1.75. SEM micrograph of a YBCO film grown on a SRO/LNO/Ni structure.

and free of microcracks (Fig. 1.75). To improve the J_c values, further investigation of the SRO/LNO/Ni structure is ongoing at present. Although SRO is chemically compatible with YBCO, we found that an initial layer of LNO on Ni is necessary to achieve high J_cs on this type of coated conductor. In fact, XRD of SRO films deposited directly on Ni showed poorer crystallinity than LNO films on Ni, and significant amounts of NiO with (111) and (200) orientation. As a consequence, J_c (0 T, 77 K) in these samples were never higher than 100 to 200 KA/cm^2.

In summary, structural and superconducting properties of conductive multilayer structures of YBCO/SRO/LNO, YBCO/SRO, and YBCO/LNO grown on LAO, STO, and Ni substrates have been investigated. Highly crystalline, low-resistive and chemically compatible YBCO/SRO/LNO/(LAO and STO) samples have been obtained. The T_c and J_c of YBCO films on SRO/LNO multilayers have showed significantly higher values than those of the YBCO films grown on single LNO layers.

SRO/LNO multilayers were successfully grown on (100) textured Ni tapes showing single (100) orientation and very good alignment with the underlying substrate. High T_c and J_c were obtained in YBCO films deposited on RABiTS™ with the structure SRO/LNO/Ni. These results indicate that the observed Ni contamination of YBCO through the LNO and LNO/Ni layers can be prevented by an additional, highly stable SRO layer. Therefore, the multilayer structure SRO/LNO is a promising buffer layer for the development of RABiTS™-based, fully conductive YBCO coated conductors.

1.11.1 Reference

1. Q. He et al., "Growth of Biaxially Oriented Conductive $LaNiO_3$ Buffered Layers on Textured Ni Tapes for High-T_c-Coated Conductors," *Physica C* **314**(1&2), 105–111 (1999).

1.12 LOW-ANGLE GRAIN-BOUNDARY TRANSPORT IN YBCO COATED CONDUCTORS

D. Verebelyi

Second-generation superconducting wires consist of an epitaxial film deposited on a textured, buffered metallic tape. These "coated conductors" are based on a substrate that is polycrystalline but very well aligned. In fact, grain boundary (GB) misorientations of only a few degrees are typical. This is essential because Chaudhari et al.[1] discovered that high-angle grain boundaries (HAGBs) disrupt the superconducting order parameter and that the transport across the boundary is governed by the Josephson effect. These large grain misalignments in $YBa_2Cu_3O_{7-\delta}$ (YBCO) result in a perturbed boundary that remains ordered and can be described by a specific sequence of structural units. With only small grain misalignment, mismatch is accommodated by periodic dislocations along the GB, separated by only slightly perturbed material. Chisholm et al.[2] investigated the disordered region with transmission electron

microscopy (TEM) and correlated atomic displacement to strain, which is modeled as a linear decrease in critical current density (J_c) at low θ. Analysis of HAGBs provides a model for the apparent exponential dependence of J_c at large θ due to a linear increase in the width of the boundary. Several studies indicate a near-exponential dependence at high θ , but large discrepancies still exist within the literature for the low-angle grain boundary (LAGB) regime. A more complete understanding of LAGBs is necessary for the advanced development of coated conductors targeting power delivery and high-magnetic-field applications.

First, we address the problem of measurements in this low-angle regime. Table 1.5 documents that a mediocre grain J_c can result in inconsistent GB results. Of particular importance is the ratio J_c^{GB}/J_c^{GR}, which is a widely reported quantity based on the assumption that J_c^{GR} scales with grain J_c^{GB}. In the ideal case this is expected to hold true, but the variables responsible for reduced grain J_c may have a lesser effect on the GB due to its disordered nature. Even an anti-correlation between J_c^{GR} and J_c^{GB} could be possible based on a doping scenario in which the preferred stoichiometry of the GB differs from that of the grain. To counter some of these concerns, our approach investigates the grain-GB system through the analysis of the V-J relationship in magnetic field combined with extended V-J curves, which enables simultaneous measurement of both the grain and GB response. This permits a direct comparison of the grain and GB while reducing the chance of experimental variables affecting the results. We combine these measurements with the practice of reporting absolute values of J_c and validating the consistently high-J_cs of the grains with successive patterning.

Two systems have been studied: the first system uses a $SrTiO_3$ (STO) bicrystal as a template for producing a single YBCO [001]-tilt boundary; the second is an ensemble of YBCO tilt boundaries formed by biaxially aligned polycrystalline substrates. Single-grain-boundary (SGB) studies give a fundamental

Table 1.5. Comparison of the grain and grain-boundary properties for YBCO 2°, 4.5°, and 7° single-grain boundaries at 77 K, self-field

Sample	θ (deg)	J_c^{GB} (MA/cm^2)	$V=J^N$	J_c^{GR} (MA/cm^2)	$V=J^N$	J_c^{GB}/J_c^{GR}
PLD	2	4.2	22	4.2[a]	22	1.00
BaF_2	2	1.6	15	1.9	13	0.84
BaF_2	2	0.93	29	0.83	23	1.12
PLD	4.5	0.79	1	4.5[a,b]	19	0.17
BaF_2	4.5	0.45	19	1.6	17	0.28
BaF_2	4.5	0.83	17	1.5	38	0.55
PLD	7	0.27	1	4.4[a]	24	0.06
PLD	7	0.38	1	1.5	20	0.25
PLD	7	0.37	1	1.4	13	0.26
PLD	7	0.62	16	0.83	20	0.74
BaF_2	7	0.34	10	0.76	9	0.45

[a]Films shown in Fig. 1.78.
[b]Film shown in Fig. 1.76.

approach to GB transport while polycrystalline samples allow for a statistical verification of the developed model, to the extent that the grain misorientation predominantly influences the transport.

SGB samples were prepared by pulsed laser deposition of YBCO on bicrystals of STO with symmetric [001]-tilt boundaries. GBs in YBCO epitaxial films have been found to match the misorientation of the substrate but can have both symmetric and asymmetric facet components. Faceting describes the discrete changes in the direction of the GB that occur on a length scale of about 50 nm, apparently due to film nucleation and overgrowth of the substrate boundary.

The biaxially aligned polycrystalline samples were fabricated by two coated-conductor techniques: ion-beam assisted deposition (IBAD) and rolling-assisted biaxially textured substrate (RABiTS™). Both architectures were completed with a YBCO film produced by the ex situ barium fluoride process. Consistently high J_c values are produced with this approach, which uses electron-beam deposited Y, BaF_2, and Cu precursors to form a dense, epitaxial YBCO film from an amorphous precursor by post-deposition processing in water vapor and oxygen at high temperature. The RABiTS™ structure, in this case, uses buffer layers of CeO_2/YSZ/CeO_2 on textured Ni (or Ni alloy), which provides an epitaxial template that is both an oxygen diffusion barrier and chemically compatible with YBCO. The IBAD architecture consists of an untextured, metallic alloy substrate coated with ion-beam-aligned YSZ and capped with a layer of CeO_2 for compatibility with the ex situ BaF_2 process.

Microstructural characterization suggests that the overall distribution of grain boundary tilts in these polycrystalline films are correlated on a local scale. According to electron backscattering maps of the grain misorientation distribution, we define an "equivalent" GB angle such that pervasive, long-range connectivity is observed (connecting 70% of the cross section with GB angles less than or equal to θ_{eq}). This enhanced, local alignment of grains presumably results from both rolling and ion-beam texturing techniques. Therefore, current transport in coated conductors may be limited by LAGBs of only a few degrees, despite global distributions with FWHM values greater than 10° according to X-ray diffraction.

We previously characterized the V-J curves for HAGBs and identified a signature non-ohmic, linear differential (NOLD) behavior. Figure 1.76 shows both intergrain and intragrain dissipation for a 4.5° SGB, with NOLD behavior at applied fields up to 4 Telsa. This is a confirmation of a result reported by Diaz et al.[3] for a 4° SGB that exhibited clear NOLD behavior at 1.6 Tesla, 77 K. We therefore propose that the transport properties of a wide range of GB angles can be grouped together by a common NOLD signature, which is likely tunneling-dominated behavior. HAGBs are characterized by a disordered boundary, while the low-angle regime shows regions of YBCO that are structurally intact and only periodically punctuated by dislocations. As the GB angle is reduced below 4°, the well-ordered regions between dislocation cores become larger than the coherence length of YBCO, and grain-like dissipation is expected. In this case, we expect that the macroscopic J_c will be fractionally reduced due to the cross-sectional loss of supercurrent from dislocations uninhabited by vortices.

To test the strongly coupled model expected at low θ, a nominal 2° GB was measured and showed grain-like V-J

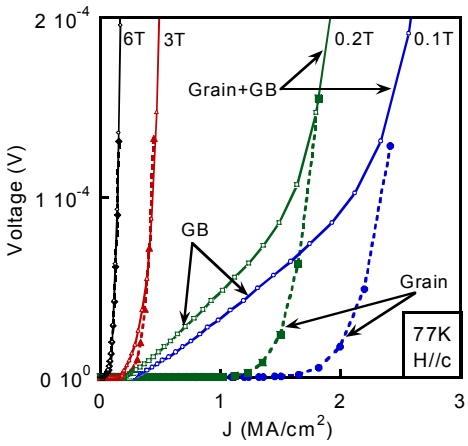

Fig. 1.76. V-J characteristics (H, 77 K) of a 4.5° SGB. The GB shows non-Ohmic, linear differential behavior with a transition to nonlinear characteristics as the surrounding grains dominate dissipation. A separate patterning of a grain is also plotted that shows the complete nonlinear V-J curve of a grain. Voltage is plotted in place of electric field due to the uncertainty of the width of the GB.

characteristics and a self-field J_c (77 K) of 4 MA/cm^2. A subsequent 50-mm patterning of the grain and GB confirmed the film homogeneity with nearly identical results. High-resolution X-ray diffraction confirmed the expected YBCO misorientations: 1.83° [001]-tilt and 0.13° [100]-tilt. According to TEM micrographs and the relationship $D = |b|/2\sin(\theta/2)$, the dislocation spacing for a 2° GB is D ϕ 11 nm, assuming b is a Burger's vector of 0.4 nm. A maximum strong channel size of 10 nm can be approximated from visual inspection of the dislocation cores from TEM images. Extrapolation with the assumption of a constant core size indicates that a 4.5° GB would have a strong channel equal to the 77 K coherence length (3.5 nm). A more elegant approach modeled by Gurevich and Pashitskii[4] predicts that nonsuperconducting regions will overlap at 4°, due to excess ion charge. This leads to a view of a 2° GB in which J_c is limited by strongly coupled material punctuated by a periodic array of dislocations that reduce the cross-sectional area available for superconducting transport. This is particularly true at low applied fields where numerous dislocations are unoccupied by vortices, due to the large equivalent field (20 T) of the defect density.

If, on the other hand, weak-linked dissipation dominated a 2° GB, simulations using extrapolated values from the HAGB regime, J_c (2×10^6 A/cm^2) and GB resistivity (1×10^{-10} Ω cm^2), find that NOLD behavior would clearly be observed in the V-J relations. However, if the strong channels of the GB exhibit grain-like, nonlinear V-J characteristics, our typical measurement configuration would be insensitive to the small voltage generated at the GB when in series with typical sized grains. This observation is consistent with the results and suggests the need for a transport-current experiment with voltage probes closer than 10 mm to achieve the sensitivity required to further investigate GBs of a few degrees. The difference in character between the strongly and weakly coupled regimes was demonstrated by Polyanskii et al.,[5] where magneto-optical imaging showed flux penetration into a 5° but not a 3° SGB at 748 Oe (7 K).

Equation (1) phenomenologically quantifies the effect of misorientation angle on J_c for the weakly coupled regime:

$$J_c(\theta) = J_c(0)\exp(-\theta/\alpha);\ [\theta\ \mu\ 4^\circ]\ . \qquad (1)$$

A fit to our SGB data above 4°, using Eq. (1), finds $\alpha = 3.2°$ and $J_c(0) = 3.2$ MA/cm^2, at 77 K, self-field. Published data at 77 K give $\alpha = 4.0°$ and $\alpha = 4.4°$. Recent data at 4.2 K find $\alpha = 5.5°$.

Figure 1.77 combines the SGB data and exponential curve fit from Eq. (1) for comparison with the J_c measurements on both IBAD and RABiTS™ tapes. These coated conductors give a unique opportunity to verify this low-angle regime with the advantage of statistics and small grain size. In the case of high-purity Ni RABiTS™, the grain size typically ranges from 10 to 100 μm, providing sampling of hundreds of thousands of GBs with the applied transport current. This number is at least an order of magnitude larger with IBAD samples, where the grain size is typically less than 1 μm. The present data underscore the important role of biaxial texture by indicating a direct correlation between J_c and the grain-to-grain orientation distribution, as parameterized by the equivalent angle θ_{eq}. This implies that the coated conductors are limited by LAGBs and that the intragrain J_c is higher than 3 MA/cm^2. To close the gap between single-crystal data and the weak-linked regime at 4°, a linear interpolation is also represented in Fig. 1.77. This linear dependence on angle is proposed to approximate the expected change in channel size. To reiterate, the data suggest that the strongly coupled GBs found in coated conductors provide sensitivity to an expected reduction in J_c from disorder along the GB.

Another perspective on tunneling-dominated vs grain-like behavior is illustrated by the results of J_c in magnetic field. Figure 1.78 shows the 77 K field dependence of J_c for several SGB samples, up to their grain irreversibility field. The field dependences of the GBs are consistent with models in which the adjacent flux lattice modifies the equivalent width of, or dephases, the order parameter near the GB. This approach yields the field dependence,

$$J_c(B) = J_c(0)\ [B\mathrm{o}/B]^{1/2}\ . \qquad (2)$$

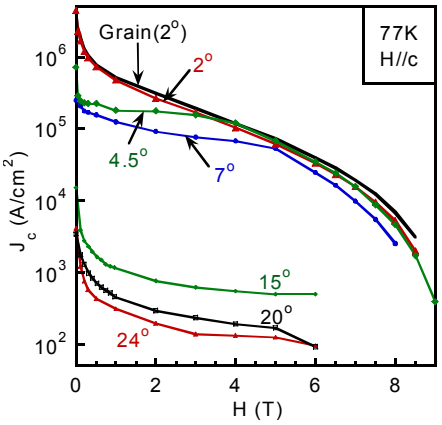

Fig. 1.77. J_c vs misorientation angle for the SGBs, IBAD, and RABiTS™ samples. An equivalent angle is used in the case of the coated conductors that represents the best estimate of the limiting angle according to electron backscattering diffraction maps. The HAGBs fit an exponential dependence, while the strongly coupled regime below 4° is interpolated with a linear dependence to zero misorientation, 4.5 MA/cm^2, which is represented by both a PLD-deposited YBCO/STO and a BaF_2-deposited YBCO/CeO_2/YSZ.

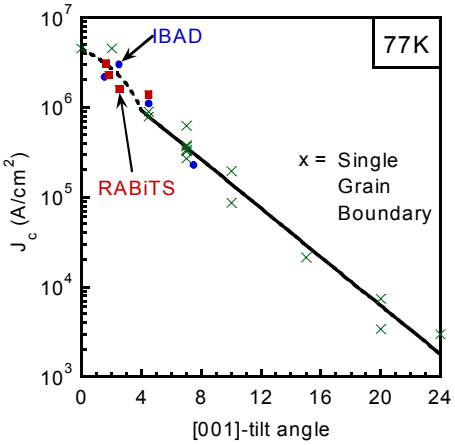

Fig. 1.78. Magnetic field dependence of several SGBs at 77 K, up to their irreversibility field. Above 4°, GBs have a reduced J_c and are less sensitive to field than their adjacent grains. At high fields and low θ, J_c is limited by the grains, not by the GB.

With an inhomogeneous flux array near the GB, the exponent decreases to 1/4. Fits to a general expression find a range of exponents from 0.63 to 0.15 for 24° to 4.5°, respectively. There is good agreement for all of the SGBs for the value of the characteristic field *B*o, which implies a constant effective junction area.

Of particular interest is the field-dependent behavior of the tunneling-dominated 4.5°, and 7° SGBs, which at low field have significantly lower J_cs than their adjacent grains, but like the HAGBs they are relatively insensitive to field. A direct product of this field dependence is a range of high fields in which the dissipation in the GB is indistinguishable compared with those of the surrounding grains. This implies that at high fields, the GBs in coated conductors are transparent to transport measurements of loss.

According to experimental findings, three characteristic regimes appear to exist for $J_c(\theta)$: the first ($\theta \leq 4°$) exhibits grain-like V-J behavior as a result of strong coupling; the second regime ($4° \leq \theta \leq 24°$) tunneling occurs across an inhomogeneous normal (or semimetal) barrier, which produces a distinct J_c with the accompanying NOLD signature; the third regime ($\theta \leq 24°$) is characterized by increased disorder at the GB, which results in more homogeneous flux penetration at the GB, larger Josephson vortices, and tunneling, which and can be described by a resistively shunted junction model.

1.12.1 Summary

The best coated conductors are characterized by grain-to-grain connectivity of only a few degrees. This can be visualized as grain boundaries perforated by islands of disorder separating channels of strongly coupled superconductor. At small fields, periodic disordered regions will be more numerous than vortices, resulting in a reduction in superconducting cross section. However, at high fields, the properties of coated conductors are indistinguishable from those of single-orientation YBCO films.

1.12.2 References

1. P. Chaudhari et al., "Direct Measurement of the Superconducting Properties of Single Grain Boundaries in $Y_1Ba_2Cu_3O_{7-\delta}$," *Phys. Rev. Lett*. **60**(16), 1653–56 (1988).

2. M. F. Chisholm and S. J. Pennycook, "Structural Origin of Reduced Critical Currents at $YBa_2Cu_3O_{7-\delta}$ Grain Boundaries," *Nature* 351, **47** (1991).

3. A. Diaz et al., "Observation of Viscous Flux Flow in $YBa_2Cu_3O_{7-x}$," *Phys. Rev. B* **58**(6), R2960–63 (1998).

4. A. Gurevich and E. A. Pashitskii, "Current Transport Through Low-Angle Grain Boundaries in High-Temperature Superconductors," *Phys. Rev. B* **57**(21), 13878–97 (1998).

5. A. A. Polyanskii et al., "Magneto-Optical Flux Study of Flux Penetration and Critical Current Densities in [001] Tilt $YBa_2Cu_3O_{7-\delta}$ Thin Film Bicrystals," *Phys. Rev. B* **53**(13), 8687–97 (1996).

2. Technical Progress in Applications Development

2.1 HTS POWER TRANSMISSION CABLE ORNL/SOUTHWIRE SUPERCONDUCTIVITY PARTNERSHIP INITIATIVE FY 1999 ANNUAL PROGRESS REPORT

J. W. Lue, J. A. Demko, M. J. Gouge, P. W. Fisher, and C. A. Foster, Fusion Energy Division; J. P. Stovall, Energy Division; D. R. James and I. Sauers, Life Sciences Division; P. M. Martin, Metals and Ceramics Division

2.1.1 Introduction

For this 3-year joint development project, Southwire will construct a 30-m-long (100-ft-long), 3-phase high-temperature superconducting (HTS) power cable, complete with electrical and thermal insulation, to demonstrate the feasibility of this promising electric utility application. The cable will be installed between two overhead utility towers and will supply 1,250 A of current at 12.4 kV to the utility and building wire-manufacturing plants located at Southwire Company Headquarters in Carrollton, Georgia. This is the first application of an HTS cable in the United States in a demanding industrial environment. The cable will be placed into full service in FY 2000 for an extended testing period under real-use situations, highlighting Southwire's expertise in HTS cables and field-testing this viable technology for the electric utility industry.

The overall objectives for ORNL in FY 1999 have been to (1) rigorously test two 5-m HTS cables and all subsystems in a laboratory environment as a proof-of-design concept, (2) validate the cryogenic dielectric system for the HTS cable, and (3) assist Southwire in preparing for the 30-m field test in Carrollton by finalizing the cryogenic system design and testing three recently constructed 30.5-m HTS cables. In a major additional task completed by ORNL in FY 1999, an alternative cable termination was designed, and hardware was procured by Southwire and jointly tested. The FY 1999 and FY 2000 activities are being conducted as a Superconductivity Partnership Initiative (SPI) cooperative agreement project, awarded to Southwire by the U.S. Department of Energy (DOE) in June 1998.

The format of the report is as follows.

- Section 2.1.2 lists the major events in chronological order for the fiscal year. These events were drawn from the quarterly progress reports.
- Section 2.1.3 describes the testing and analysis of the two 5-m superconducting cables in the ORNL Cable Test Facility. The section is based upon a technical paper presented at the 1999 Cryogenic Engineering and International Cryogenic Materials Conference in July 1999.
- Section 2.1.4 describes the testing and analysis of the cryogenic system in the ORNL Cable Test Facility. The section is based upon a technical paper presented at the 1999 Cryogenic Engineering and International Cryogenic Materials Conference in July 1999.
- Section 2.1.5 describes the overcurrent testing performed on HTS tapes.
- Section 2.1.6 describes the critical-current measurement made on Phases 1 and 2 of the 30-m superconducting cables at Carrollton, Georgia.
- Section 2.1.7 describes the cryogenic system requirements for HTS cables and is based upon the specification that was developed for the cryogenic system purchased for the 30-m superconducting cables.
- Section 2.1.8 describes the development and testing of a new pressurized termination, which was a major additional task completed by ORNL in FY 1999.
- Section 2.1.9 gives an overall summary of the project progress and results for the fiscal year.

Reported in another chapter of this progress report is the investigation of the properties of the cryogenic dielectric material being used in the superconducting cable.

2.1.2 Summary of FY 1999 Activities

2.1.2.1 First Quarter of FY 1999—October 1 to December 31, 1998

- The test program for the 5-m, single-phase prototype cable successfully completed a major milestone this quarter. The cable was operated simultaneously at rated voltage (7.2 kV ac line-to-ground) and rated current (1250 A ac), experimentally proving a valid cable design. The cable was also operated without current at voltage levels up to 18 kV to verify dielectric integrity in the actual cable geometry. HTS cable ac losses were measured as a function of liquid nitrogen temperature.
- The dielectric testing of Cryoflex continued during the quarter. Both impulse and ac breakdown tests were conducted on model cables with the same total insulation thickness proposed to be used on the 30-m HTS cables. The impulse breakdown tests of model cables found the basic impulse insulation level to be more than adequate.
- ORNL provided expertise in development of the technical specification for the 3-phase, 30-m cable to be installed at Southwire facilities in Carrollton, Georgia. Conceptual design was initiated of an alternative cable-termination configuration (operating at pressure instead of under vacuum).
- Mr. Roy Richards, Jr., Southwire CEO, visited ORNL on October 2, 1998, and toured the cable test facility, dielectric test facility, and superconducting tape testing laboratory.

2.1.2.2 Second Quarter FY 1999—January 1 to March 31, 1999

- The test program for the 5-m, single-phase prototype cables continued during the quarter with significant progress. The first round of testing was completed on Cable #1 with an extended time run at rated voltage (7.2 kV ac line-to-ground) and rated current (1250 A rms). During the week of February 1, 1999, Cable #1 was removed from the test facility and Cable #2 was installed. Cable #2 was then successfully subjected to a full series of tests (dc critical current, ac losses, ac voltage withstand, and extended operation).
- The dielectric testing of Cryoflex continued during the quarter as both impulse and ac breakdown tests were conducted on model cables with the same total insulation thickness proposed to be used on the 30-m HTS cables.
- ORNL assisted Southwire in the evaluation of cryogenic system proposals. A request for quotation (RFQ)was issued by Southwire, and several proposals were received in February 1999. The RFQ contained the technical specification for a cryogenic system to cool the 3-phase, 30-m cable to be installed later this calendar year at Southwire in Carrolton, Georgia. Southwire selected a firm (PHPK Technologies, Inc.) to provide the cryogenic system, and an initial project review meeting was held in March 1999 at ORNL.
- The conceptual design of an alternative cable-termination configuration operating at pressure instead of under vacuum was completed and was reviewed with Southwire during the quarter. Based upon the successful design review, a prototype will be built and tested with 5-m Cable #2 later this fiscal year.
- ORNL assisted Southwire in measuring the critical current of their first 30-m cable. Southwire completed manufacturing of the first of three 30-m cables. Southwire installed the cable in a cryostat and has fabricated end connections for the cryostat. ORNL loaned Southwire a dc power supply and data-acquisition system. ORNL assisted Southwire in measuring the critical current of both the inner and outer conductors as a quality check of the cable manufacturing and HTS tape performance.
- ORNL measured the neutral-connection contact resistances on a 0.5-m prototype cable made by Southwire. Two different methods of connecting the neutral or outer conductor were simulated on the 0.5-m prototype cable.

2.1.2.3 Third Quarter FY 1999—April 1 to June 30, 1999

- The major activity in the quarter was fabrication, assembly, and successful testing of a new pressurized termination (T2) design. The concept and the prototype design were developed by Chris Foster and Paul Fisher (ORNL).
- ORNL assisted Southwire in the review of system process calculations and design drawings submitted by the 30-m cable cryogenic system vendor, PHPK Technologies Inc. There was also an on-site visit to review plans and facilities for component fabrication
- ORNL continued to assist Southwire in measuring the critical current of their 30-m HTS cables.

2.1.2.4 Fourth Quarter FY 1999—July 1 to September 30, 1999

- Two technical papers were presented at the 1999 Cryogenic Engineering and International Cryogenic Materials Conference (July 12–16, 1999, Montréal, Québec, Canada). The first paper summarized the electrical testing of the two 5-m HTS cables.[1] The second paper summarized the cryogenic system testing.[2] Excerpts from these papers are included in this report.
- A project presentation summarizing the FY 1999 accomplishments and experimental results was given at the 1999 Annual Peer Review of the Superconductivity Program for Electric Systems (July 26–27, 1999, Washington, D.C.).
- Assembly of six terminations for the 30-m cable began and is scheduled to be completed in October 1999.
- Testing of the partial-discharge diagnostic system for the 30-m cable was completed on the 5-m cable.
- Overcurrent tests of HTS tapes and copper wires were completed and summarized in Sect. 2.1.5 of this report.
- Aging tests of Cryoflex model cables began.
- Critical-current test of two phases of the 30-meter HTS cable were completed and are summarized in Sect. 2.1.6 of this report.
- A summary of the general requirements of a cryogenic system for an HTS cable was developed and is summarized in Sect. 2.1.7 of this report.

2.1.3 Single-Phase 5-m HTS Transmission Cable Tests

The development of HTS transmission cables headed by Southwire Company went into the phase of building and testing cables with dielectrics, high voltage, and long-duration tests. This followed the construction and testing of several 1-m-long prototypes of core conductor for electrical and thermal evaluations.[3] Two 5-m single-phase HTS transmission cables were built with Bi-2223/Ag tapes and a cold-dielectric, superconducting shield and were completed with vacuum-jacketed enclosure.

A versatile HTS cable test facility has been designed and built at ORNL to evaluate the performance of prototype HTS power transmission cables at lengths on the order of 10 m.[4] The two 5-m cables were tested for dc characteristics, ac losses, high-voltage withstand, and long-duration performance.

2.1.3.1 The 5-m HTS Cables

The single-phase, 5-m HTS cables were built based on a cold-dielectric design. The core conductor consists of four layers of helically wound, Bi-2223/Ag tapes supplied by Intermagnetics General Corporation (IGC). Four layers and a total of 104 tapes were chosen to provide enough capability for the design current of 1250 A. The tapes were machine-wound on a flexible stainless steel former with an outer diameter of 38 mm. Cryoflex cold-dielectric tapes were wrapped between the inner conductor and the outer HTS shield. The outer HTS conductor, which is similar to the inner conductor, provides shielding of

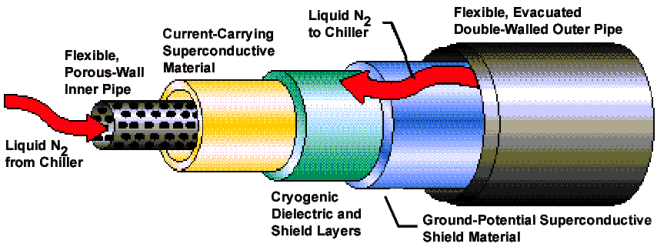

Fig. 2.1. A cutaway view of the Southwire HTS 5-m cable.

the field generated by the currents flowing on the inner conductor and thus eliminates magnetic fields and eddy currents in the external structure.

Figure 2.1 shows a cutaway view of the cable. The liquid nitrogen coolant is to flow down the center of the former and return through the annulus between the HTS shield and the vacuum-jacketed outer pipe. The second cable was wound with an improved winding head, and a different technique was used for the shield terminal connections. Both cables were designed for 1250 A rms at a phase-to-ground voltage of 7.2 kV. These cables serve as a prototype of the longer (30-m) three-phase cable to be installed in late 1999 at the Southwire Company cable manufacturing complex in Carrollton, Georgia.

2.1.3.2 The HTS Cable Test Facility

The initial HTS cable test facility consisted of a pair of vacuum terminations (T1), a high-vacuum pumping station, a cryogenic cooling system, dc and ac high-current power supplies, ac high-voltage power supplies, and a data-acquisition system. A sketch of the test facility is provided in Fig. 2.2. The 5-m HTS cable is located between two terminations, one on the east end of the facility, the other on the west end. The termination provides a transition from sub-cooled (70–80 K) liquid nitrogen at 3 to 7 bar in cable space to a vacuum chamber, and a second transition from vacuum to atmosphere at room temperature. Bushings for the transitions are rated for full cable current and voltage. The two terminations are pumped through a common vacuum header by a pumping station to the 10^{-6} Torr range to provide sufficient thermal and electrical insulation.

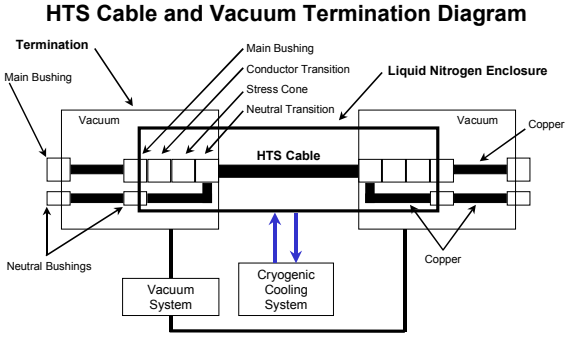

Fig. 2.2. ORNL/Southwire HTS Cable Test Facility layout.

The cryogenic cooling system is built on a liquid nitrogen skid that can provide about 1 kW of cooling at 70 to 80 K. It consists of a pressure/surge dewar, a subcooler, a liquid nitrogen circulation pump, and the associated piping. A vacuum pump is also included to pump the subcooler bath to between 70 and 77 K. Not shown in Fig. 2.2 are a 3-kA dc power supply, a 2-kA rms ac power supply, a 25-kA dc power supply that can supply a pulse loading to the cable, and a 100-kV high-voltage power supply. The data-acquisition system contains three ten-channel multimeters with fiber-optic links for the high-voltage signals to a PC using the LabVIEW program.

2.1.3.3 DC Measurements

Cooldown of the HTS cable to the testing temperatures was achieved by first precooling the cable with nitrogen gas and liquid nitrogen supplied from the outside storage tank. The nitrogen skid was then started, and subcooled liquid nitrogen was flowed to the cable via one termination, through the center of the former, turned around at the other termination, through the annulus of the cable and the cryostat, and back to the skid for closed-loop cooling. (Details of the cryogenic system, performance of the skid, and the heat load of the terminations are reported in ref. 2.)

A series of dc voltage-current scans were performed to characterize the 5-m cables. The observed dc V-I curves showed a broad resistive transition, which is characteristic of the HTS tapes supplied by IGC. The measured curves of resistivity (proportional to voltage drop), ρ, of the cable vs current density, J, can be reasonably well fitted by a power law: $\rho = k \cdot J^n$. Around the critical current, the curve-fitted n-value averages only about 2.2. The critical currents of the two cables (as defined by the voltage drop criterion of 1 μV/cm) as a function of the average cable temperature are shown in Fig. 2.3. In the temperature range of 72 to 82 K, the measured critical currents increase nearly linearly as the cable temperature decreases.

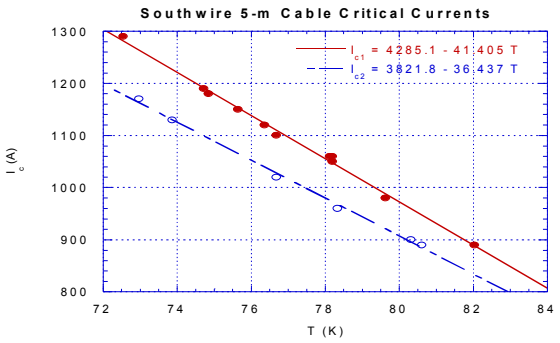

Fig. 2.3. Critical currents of the two 5-m cables as a function of temperature.

2.1.3.4 AC Loss Measurements

Measurements of ac loss of the cables were made by an electrical technique similar to that used for the 1-m core conductor prototypes.[3] Voltage taps were placed on the two ends of the core conductor, and one lead was laid between the HTS and the dielectric tapes to follow the cable to the other end. A digital lock-in amplifier measured the voltage across the cable and the phase angle between the voltage signal and the current signal. The product of the current and the voltage in phase with the current gives the ac loss ($P = I \cdot V \cos\theta$) of the main conductor. A signal from a Rogowski coil with an integrator was used as the reference signal, and a second Rogowski coil corrected its phase error. Curve fitting of the loss voltage was also made to take out the linear term due to the resistive terminal joints.

Because of the existence of the shield layer, there was a concern about its effect on the measured loss voltage. Figure 2.4 shows the measured ac loss per unit length of the cable as a function of the ac rms current taken on two different runs. On the first test, the shield layer was grounded at one end only and was open at the other end. On the second test, the shield was also grounded at one end, but an external Cu cable was used to tie the two ends together to form a closed loop. The induced current in the shield layer should be quite different in these two tests. However, nearly the same loss data were obtained. Thus, the main conductor ac loss measured by the present technique is independent of the shield current.

The ac losses of the cables were measured at several different cable temperatures. Figure 2.5 shows the ac loss of the first cable as a function of the ac rms current at four different temperatures.

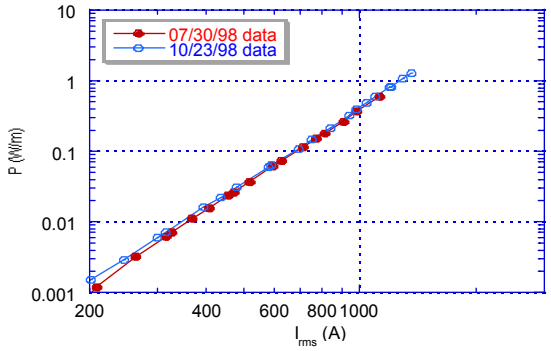

Fig. 2.4. ac loss of the first 5-m cable measured with two different shield connections.

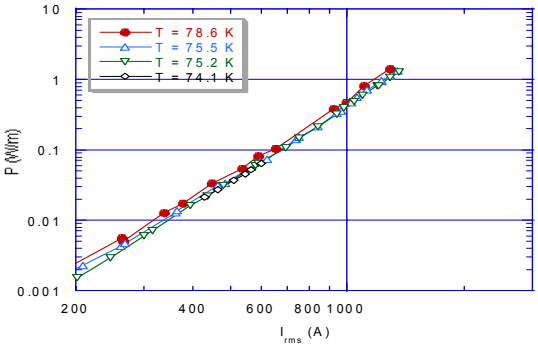

Fig. 2.5. ac loss of the first 5-m cable measured at four different temperatures.

There are small but notable differences in the measured losses. Loss rates of 0.8 to 1.3 W/m were measured at the rated current of 1250 A rms.

The main effect of a changing temperature to the cable is the increase in critical current as temperature lowers. Thus, a good comparison in ac losses at different temperatures could be in terms of the peak current to the critical current ratio, I_p/I_c. But, as is noted earlier, the broad resistive transition of the HTS tapes can be reasonably well fitted by a power law: $\rho = k \cdot J^n$. Under this assumption, Dresner has studied the ac loss of HTS cables.[5,6] In the limit of incomplete penetration (at lower currents), the dependence of ac loss of the cable P_{cable} on I_p/I_c was found to take the form

$$P_{cable} \propto I_c^{\alpha} \cdot (I_p / I_c)^{\kappa},$$

$$\alpha = \frac{2n + 3}{n + 2}, \qquad \kappa = \frac{3n + 4}{n + 2}$$

The proportional constant in the above equation depends mainly on the geometric factor of the cable. For conductors with sharp resistive transitions (i.e., having high n-values, $\alpha = 2$ and $\kappa = 3$, the same as predicted by the critical-state model. It is also to be noted that both α and κ are not too far from the critical-state model values, even for the present very low n-value of 2.2.

The above equation indicated that the proper way to compare ac losses is not to simply plot P_{cable} vs I_p/I_c, but to plot the normalized cable loss $P_{cable}/I_c\alpha$ vs I_p/I_c. For the present low n-value of 2.2, $\alpha = 1.76$. Thus, in Fig. 2.6 $P_{cable}/I_c^{1.76}$ vs I_p/I_c is plotted at the four different temperatures. The normalized ac losses at different temperatures converge onto a single curve. Thus, the present loss data agree well with the scaling law predicted by Dresner.

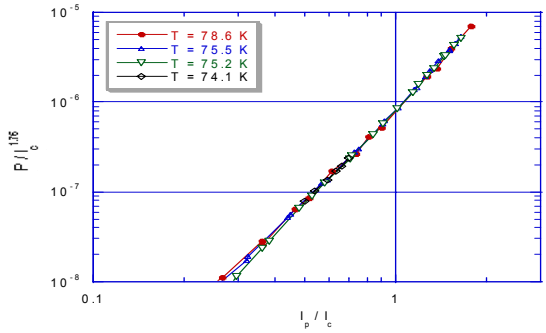

Fig. 2.6. Normalized ac loss of the first 5-m cable measured at four different temperatures.

Similar results were obtained for the second 5-m cable. Figure 2.7 compares the ac losses of the two cables at a temperature of about 76 K. Although Cable #2 had lower I_c than Cable #1 (as shown in Fig. 2.3), it had lower ac losses. At 1250 A rms, the ac loss of Cable #2 is 0.7 W/m as compared with 1 W/m of Cable #1. This may be the result of the tighter and more uniform winding achieved in Cable #2.

2.1.3.5 Induced Current in the Shield Conductor

Both ends of the HTS shield layer were brought out to room temperature by long lengths of Cu through cold liquid-nitrogen-to-vacuum and vacuum-to-atmosphere feedthroughs. During most of the cable test, the shield was grounded at one end, and an external Cu cable was used to tie the two ends together to form a closed current loop. The external cable consists of two Cu cables rated at 500 A. The induced current through the shield was measured for core conductor currents up to 1400 A. Figure 2.8 shows that the shield current increases linearly with the core current as expected, but its magnitude is only about 46% of the main current. In a later

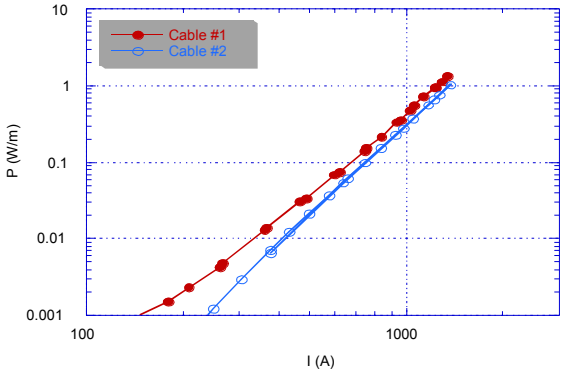

Fig. 2.7. Comparison of the ac losses of the two 5-m cables at ~76 K.

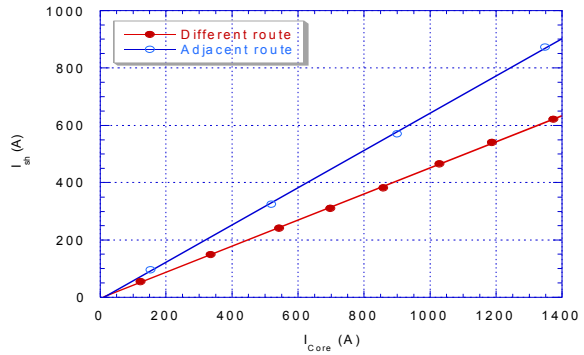

Fig. 2.8. Measured shield currents as a function of the core conductor current with two different external cable-routing geometries.

test, the shield external cable was rerouted to follow more closely the supply cable of the main conductor. The second curve in Fig. 2.8 shows that the shield current increased to about 65% of the main current. Thus, the magnitude of the shield current in a single-phase test depends strongly on the relative loops (geometry) of the primary and the secondary circuit.

A measurement of the shield current was also made after a long-duration test (more than 3 d) of the cable. The shield current had lowered from 46 to 43% of the core current. When one of the two external interconnecting Cu cables was disconnected, the shield current further reduced to 37% of the core current. Apparently, the magnitude of the shield current also depends on the impedance in its loop. The reduction of shield current after a long-duration test can be explained by the warming up and the resultant increase in the resistance of the Cu braids connecting the HTS shield to the room-temperature feedthrough.

2.1.3.6 High-Voltage Testing

A high-voltage withstand test of the cable-termination system was made at a termination vacuum of 4.2×10^{-6} Torr. Voltage was stepped up to 18 kV ac (2.5 times the design operating voltage) without a breakdown. Testing at this level was performed to verify that the cable and terminations would meet an industry voltage standard. The high voltage was held for 30 min at 18 kV. Figure 2.9 shows the measured partial discharge in picocoulombs (pC) and the leakage current as a function of the applied voltage. The partial discharge was independent of the applied voltage and stayed at the background value of about 23 pC. The leakage current increased linearly with the applied voltage as expected. The measured leakage currents were consistent with the capacitances estimated for the HTS cable and the external room-temperature cable insulated with ethylene propylene rubber (EPR).

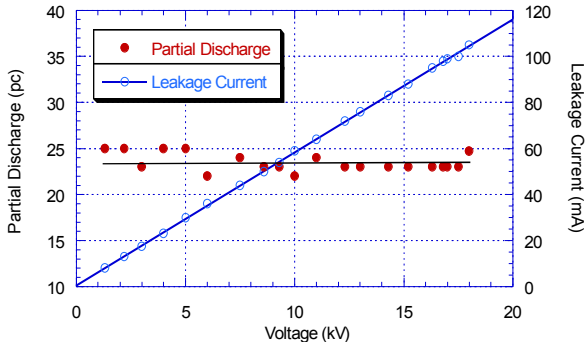

Fig. 2.9. Partial discharge and leakage current of the cable-termination system as a function of the applied voltage.

A test was also made with the voltage held at the design operating value of 7.2 kV ac and with the current increased from zero to 1420 A rms. The leakage current was found to be steady at about 44 mA.

2.1.3.7 Long-Duration Test

Another test of the integrity of the HTS cable and the test facility is a long-duration run of the cable at its design operating conditions. The first 5-m cable was run at 7.2 kV ac line-to-ground voltage and 1250 A rms current for 27 h. The inlet liquid nitrogen temperature remained constant at 79 K, and the outlet from the cable remained at 82 K during the entire test.

The second 5-m cable was run continuously for 80 h. Figure 2.10 shows the inlet and outlet temperatures of the liquid nitrogen to and from the cable. Again the inlet temperature remained at about 79 K. In the first three days, the flow rate was set at 250 g/s (5 gpm), and the outlet temperature remained constant at about 82 K. Then a burnout of a wire nut in the power supply transformer circuit caused a period of no ac current for about 8 h. During that time the outlet temperature lowered to about 80.5 K. After the current was restored, the outlet temperature went back to 82 K. The circulation rate of the coolant was next varied in several steps. This resulted in the corresponding changes in the outlet temperature shown in Fig. 2.10.

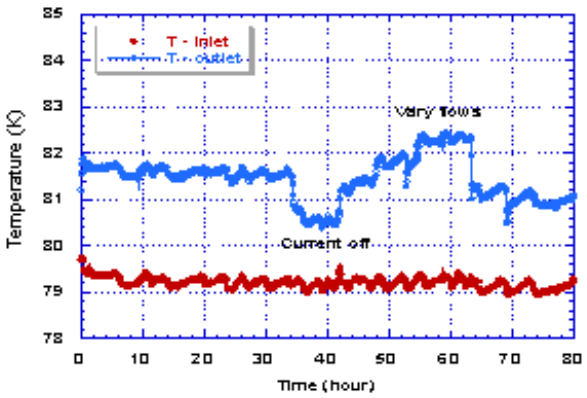

Fig. 2.10. Inlet and outlet temperatures of the liquid nitrogen coolant during the long-duration test of the second 5-m cable.

During both design-condition long-duration runs, the subcooler bath on the cryogenic skid was not pumped and the cable main conductor temperature was stable at about 80.5 K. At this temperature the operating current has a peak value of 1.8 to 1.9 times the dc critical current. Thus, the broad resistive transition of the HTS tapes made it possible to operate the cable stably at currents significantly above its critical current.

2.1.3.8 Conclusions

Two 5-m-long single-phase HTS cables have been built and tested successfully in this phase of the development of HTS transmission cables by the Southwire/ORNL team. The cables were designed and built with cold dielectrics and a coaxial HTS shield. Test results showed that both cables met or exceeded the design parameters.

DC characteristics of both of the cables have been measured at temperatures between 72 and 82 K. The critical currents were found to increase linearly with decreasing temperatures in this range. The ac loss of the cables was measured as a function of currents at line frequency at several different temperatures. The ac losses of 1 W/m for the first cable and of 0.7 W/m for the second cable were measured at the design current of 1250 A rms. The ac losses were also found to scale as the ratio of ac current to the critical current ratio, as predicted by Dresner's theory.

High-voltage testing of the cable-termination system proved the integrity of the cold-dielectric and the termination design. Both cables and the terminations surpassed 2.5 times the operating voltage (18-kV ac) without a breakdown. Both cables have operated continuously for extended periods of time (up to 72 h) stably at the rated 7.2 kV line-to-ground voltage and the rated 1250 A current.

System heat loads, liquid nitrogen flows, and pressure drops have also been measured (see sections 2.1.4 and 2.1.8). These and the above test results provide confidence in the design approach. Valuable information from the 5-m prototype cable test program is being used in the design and construction of the 30-m three-phase cables.

2.1.4 HTS Cable Cryogenic System Tests

A series of tests of the first 5-m HTS transmission cable were conducted in the cable test facility. The simplified diagram of the HTS cable cryogenic system in Fig. 2.11 shows the main flow loop and instrumentation locations used in the pressure-drop and calorimetric measurements of the HTS cable system. The liquid nitrogen flows through the cable in a counterflow cooling mode as described earlier.

Table 2.1. Description of main operating parameters for each test run

Run	Duration (h)	Flow (g/s)	Current (A rms)	Voltage (kV)
1	8	Varied	0	0
2	10	187	1250	7.5
3	12	210	1250	7.5
4	26	206	1250 to 0	7.5 to 0
5	80	Varied	1250 to 0	7.5 to 0

The results of four runs of the system are described. The main operating parameters for the runs are listed in Table 2.1. The first run was conducted to establish a baseline of the system performance without any current applied to the cable. This made possible the measurement of the background heat loads and pressure-drop dependency on flow rate. The second and third runs were conducted to extend the operating time of the cable. Steady-state operation was not confirmed, so Run 4 was undertaken to operate the cable at voltage and current for 26 h to achieve steady-state operation for an extended period. A fifth run, conducted for 80 h, demonstrated the capability of operating the cable for extended periods at current and voltage. These runs simulated the normal operation of the cable expected in the field.

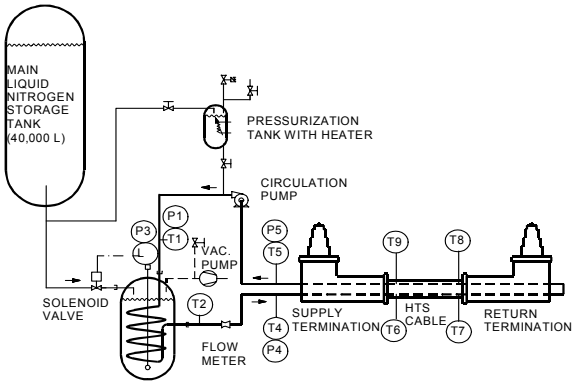

Fig. 2.11. Simplified schematic of HTS cable cryogenic system.

The pressure drops in the HTS cable system were measured as a function of flow without carrying current in Run 1. The HTS cable pressure drop was measured across the supply and return lines to the HTS cable (P4-P5). The data fit well with the following expression for the pressure drops in the system:

$$\Delta P = \Delta P_g + K_L \dot{m}^2$$

where the pressure drop ΔP is a combination of the contribution due to changes in elevation within the system ΔP_g and the mass flow rate through a modified loss coefficient K_L for the HTS cable and terminations [$K_L = 2.8 \times 10^{-6}$ bar/(g/s)^2].

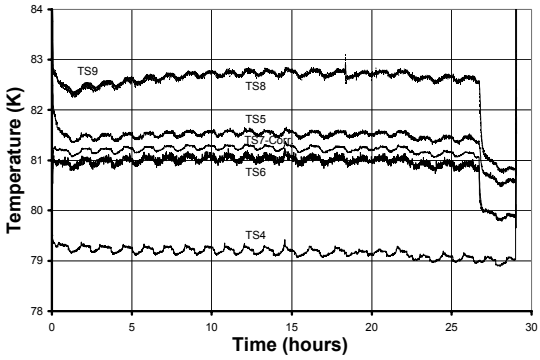

Fig. 2.12. Measured HTS cable system temperatures for Run 4.

A 26-h test, Run 4, was conducted. The temperatures for this test are shown in Fig. 2.12. During the first hour, there was some cooling down of the system. Temperature cycling was observed due to the periodic filling of the subcooler. During the subcooler-filling process, the bath-side pressure changed, raising or lowering the saturation temperature of the bath; in turn, the supply temperature of the liquid

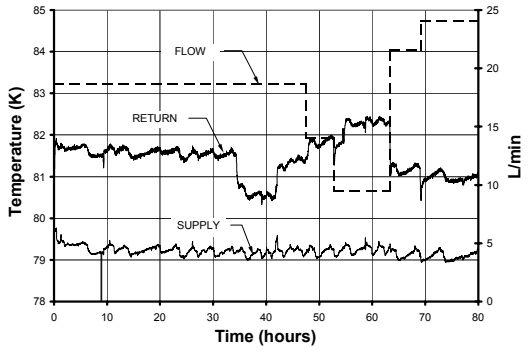

Fig. 2.13. Measured HTS cable flow rate, system supply, and return temperatures for Run 5.

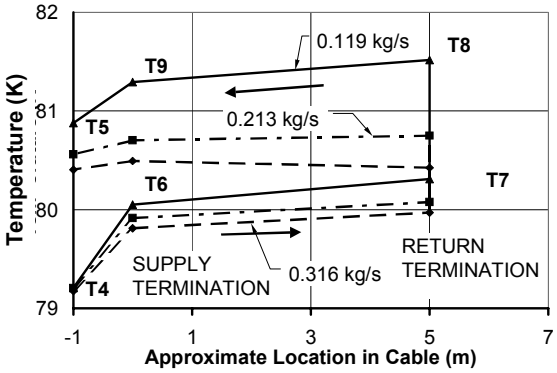

Fig. 2.14. Measured temperature distribution in the HTS cable system for Run 1 at different flow rates using average termination heat load of 291 W to estimate T7.

nitrogen to the HTS cable changed. After 14 h, the temperatures of the liquid nitrogen external to the cable (T8 and T9) reached a maximum and even decreased afterward. This finding demonstrates that the HTS cable system will operate stably over long time periods.

The inlet and outlet temperatures for Run 5, along with the corresponding flow of liquid nitrogen, are shown in Fig. 2.13. At about 35 to 42 h into the run, there was an electrical problem in the power supply, and the current was turned off. This is the cause for the drop in the return temperatures during this period. This shows that the HTS cable system responds quickly to changes in current. From 47 h until the end of the run, the flow was changed to measure the cable response. The cable operated with flows down to 9.5 L/min without any difficulty.

The temperatures throughout the system for Run 1 are shown in Fig. 2.14 for three different flow rates. The temperature sensor T7, had a broken lead that was repaired. The repair produced a slight drift in the calibration, which was corrected either by calorimetry or by an in situ calibration. For this graph, a calorimetric method using an average termination heat load of 291 W was used to correct T7. The liquid nitrogen enters the cable at T4, leaves the termination at T6, enters the far end termination after T7, leaves the far end termination at T8, continues to flow over the outside of the HTS cable to T9, passes through the supply termination, and leaves the system at T5. The highest flow rate measured, 316 g/s, produces the lowest system temperatures. In this case, the temperature of the liquid nitrogen increases all the way through the HTS cable. These temperature profiles can be expected in the non-ideal heat exchanger with heat transfer from an external source. For this case, the liquid nitrogen gradually increases in temperature until it enters the supply termination, where heat transfer occurs to the supply stream. The highest temperature in the system is just prior to entering the supply termination. For the medium flow case of 213 g/s, the temperatures on the outside of the cable remain nearly the same. The former stream picks up most of the cable heat load. Finally for the lowest flow, 119 g/s, the highest system temperature occurs at the exit of the return termination. This observation agrees with what was determined earlier through analysis because the HTS cable behaves similarly to a counterflow heat exchanger.

The portion of the flow path from T9 to T5 is the last the liquid nitrogen passes through before returning to the cryogenic skid. For the most-efficient operation, it would be better if the temperature increased during this leg. This is not the case here. Instead, the stream leaving the cable heats up the stream supplied to the cable for cooling. This suggests that there may be some better way to design the cooling flow path through the termination.

The temperature distribution through the HTS cable system for Run 3 is shown in Fig. 2.15 for cases with and without current and voltage applied at a constant flow rate. In this figure the in situ approximate calibration was applied to correct T7. The maximum system temperature is about 1.7 K lower for the zero-

current and voltage case. The overall system temperature drop is about 0.9 K lower.

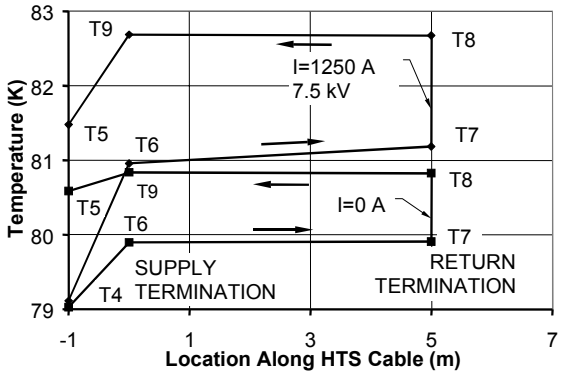

Fig. 2.15. Temperature distributions throughout HTS cable system at the same flow rate with and without current applied. Data are from Run 4.

2.1.5 Over-Current Testing of HTS Tapes

The sample HTS tape lengths were all about 40 cm, which made two periods of 30° lay-angle winding on a 1.5-in. former. The voltage taps covered the middle period of about 21 cm long. Current pulses up to 200 A were applied to monitor the voltage (and thus the resistance) of the sample. For comparison, similar current pulses were applied to a 24 AWG and an 18 AWG copper wire in an open liquid nitrogen bath.

Figure 2.16 summarizes the measured resistivity of the HTS tape and the Cu wires as a function of the pulse current density. The measured critical current of 27 A at the 1 μV/cm criteria gives a resistivity of 2.6×10^{-10} Ω-cm for the Bi-2223/Ag-alloy HTS tape at the overall tape critical current density of 3900 A/cm^2. A measurement of the resistivity of this HTS tape as it was warming up from liquid nitrogen temperature showed a normal transition from 110 K to 128 K. Above that the resistivity increased slowly and linearly with temperatures. Extrapolating a linear fit between 160 K to 130 K down to 77 K indicated a normal resistivity of 4.6×10^{-7} Ω-cm for the HTS tape. Thus, Fig. 2.16 indicated that the HTS did not go fully normal until the pulse current density was above 2.0 kA/cm^2 , a little more than five times the critical current density. At a fault of ten times the design current of the Southwire 30-m cable, each tape would carry about 120 A. At this current the present data showed that the tape resistivity would be about 3.0×10^{-7} Ω-cm. Thus, the HTS is still not fully normal and will carry a significant fraction of the total current. At higher current densities, the second test had somewhat higher resistivity than the first test. Due to the adjustment of the power supply in the second test, the current did not decrease as much after the sample resistivity went high, so there was more heating in the second test during the pulse.

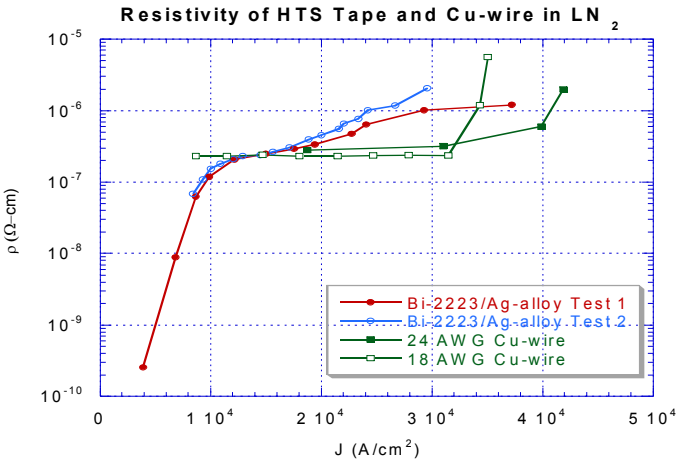

Fig. 2.16. Resistivity of HTS tape and copper wires as a function of the over-current density.

The resistivity of the copper wires was seen to be about 2.3×10^{-7} Ω-cm at liquid nitrogen temperature as expected. No overheating was seen at pulse current density up to about 30 kA/cm^2. Above this, the resistivity increased rapidly, and burnout occurred at less than 40 kA/cm^2 for the 24 AWG wire (which has smaller surface to area ratio than the 18 AWG wire).

2.1.6 Summary of Critical Current Tests on 30-m HTS Cable

Southwire completed manufacturing the first and second of three 30-m cables by June 1999. Southwire installed the cables in a cryostat and fabricated end connections for the cryostat. ORNL loaned Southwire a

3-kA dc power supply and data-acquisition system. ORNL staff assisted Southwire in measuring the critical current of both the inner and outer conductors of the first and second 30-m phases with the cable being cooled by liquid nitrogen.

Figure 2.17 summarizes the dc test results of the average of the first two phases of the Southwire 30-m HTS cables. An I_c of 2980 A and an n-value of 9 were observed. For comparison, the 5-m critical current of the 5-m cable is shown with an I_c of 1090 A and an n-value of 3. The difference between the critical current and n-values is attributed to both the difference between silver tapes and silver alloy tapes and the progress made by the tape manufacturers.

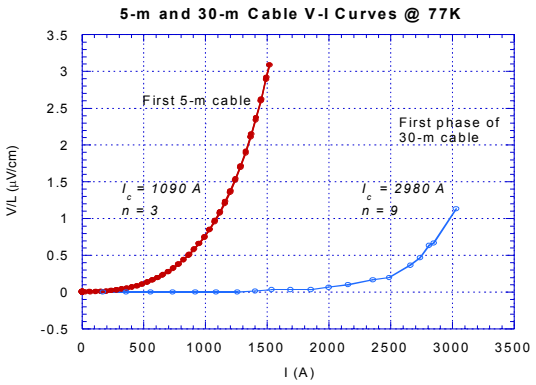

Fig. 2.17. Comparison of critical currents for 5-m and 30-m HTS cables.

2.1.7 Cryogenic System Requirements for HTS Cables

The following requirements of a cryogenic system have been defined.

- **Functionality.** The cryogenic system can be thought of as having different subsystems. Each subsystem performs a necessary function during all operating modes of the overall cryogenic system. Four suggested subsystems are
  - **refrigeration skid,** which transfers heat from the low-temperature HTS cable to warm surroundings;
  - **pump station,** which provides pressurized flow of coolant for cooldown, circulation during normal operation, or rapid recovery from a fault condition;
  - **coolant storage,** which are tanks to maintain a sufficient inventory of liquid nitrogen coolant (these may be used for back-up refrigeration in the event that the refrigeration system shuts down); and
  - **inventory management,** which minimizes losses of inventory in the system due to background losses and fault conditions.
- **Thermal conditions.** In order to operate a HTS power application, such as a cable, the HTS components will necessarily exist in a series of conditions that require the cryogenic system be able to be reconfigured to allow the HTS to transition between these conditions or states. Suggested definitions of the cryogenic-system states are as follows:
  - **warm,** the state in which the HTS transmission line is purged and at room-temperature conditions;
  - **cooldown,** the state in which the system is configured to gradually bring the HTS cable to operating temperature (it is also filled with liquid nitrogen during this operation);
  - **stand-by,** the state in which the HTS transmission cable is filled with liquid nitrogen but the temperatures are too high to permit energizing the cable;
  - **normal,** the state in which the HTS transmission cable is cold (i.e., the temperature everywhere along the cable is below the HTS transition temperature and is ready to be energized); and
  - **warm-up**, the state in which the system is configured to allow the HTS transmission cable to warm up to room temperature.
- **Reliability.** Reliability targets are hard to define without input from a utility partner as to what it would require. Some valuable information is found in a paper by F. J. Kadi and R. C. Longsworth.[7] Two relevant points were made in this paper. First, that for the six standard nitrogen plants tracked in the paper, there were on average 18 outages per year. Due to appropriate backup systems, this resulted in nitrogen delivery failure rate of once in 30 years. The second item was reliability for a He-cooled superconducting transmission line. The required reliability estimates ranged from a 1-d outage every 20 years to a

0.031outages per year per cable mile with an average duration of 336 h. The real reliability requirements should be defined by a utility; these requirements may be considered as preliminary.

- **Maintainability.** An estimated 74% of the nitrogen plant outages reported in the paper by Kadi and Longsworth had a mean time to repair (MTTR) of less than 6 h. Only 1.1% had a MTTR greater than 72 h. These are realistic numbers for a nitrogen plant, and something close could be expected for other similar nitrogen systems.There are several factors to consider in the maintainability of the cryogenic system. A few pertinent suggestions are as follows.
  - **Use standardized equipmen**t wherever possible to optimize interchangeability and to reduce the complexity of maintenance tasks.
  - **Minimize the need** for specialized training beyond what utility technicians already require.
  - **Provide accessibility** so that high-maintenance parts can easily be replaced.
- **Capacity.** The total thermal loads to the system (or refrigeration requirements for a 3-phase system) are in the range of 10 to 15 kW per 1000 m. The lowest temperature in the system may be as low as 67 K. Mechanical loads that must be tolerated by the system include the pressure rating. To prevent bubble formation, it may be expected that a HTS cable system will operate with a maximum pressure of 10 bars. This pressure could be somewhat higher during the cooldown of a very long cable.
- **Efficiency.** The cryogenic system efficiency required is driven by economic factors. It should be as high as possible.
- **Automation.** Two operating modes are defined.
  - **Fully automatic,** in which operator intervention is minimal during normal operation of the HTS power application. State transitions occur "automatically" but may be watched by an attendant. Most transitions between states will occur infrequently. Rapid fault recovery is accomplished automatically.
  - **Load following,** which is linked to cable power demand. Coolant flow and refrigeration adapt to changes in thermal load.
- **Complexity.** In his plenary talk at the 1998 Applied Superconductivity Conference, Dr. Alex Braginsky reported results of an industry survey on the main obstacles to market growth of superconducting technologies. Two points are relevant here.
  - **The psychological factors to the use of cryogenics.** "I think that power plant operators are already familiar with two-phase flow systems and high-temperature applications, and that with some reasonable amount of training, can adapt this existing experience and knowledge to cryogenics."
  - **Superconducting products are difficult to use.** "Power plant operators are already familiar with running large, automated, complex thermal systems (i.e., the boiler plant and steam turbogenerator unit at large power plants). I believe one goal here should be to make the HTS power application no more complicated than existing power plant operations."

2.1.8 Pressurized Termination (T2) Development

The vacuum termination concept was used through most of the 5-m cable test program, and it supported the successful characterization of prototype cable performance. However, it became apparent that the reliability of the cold bushings was an issue that could not be resolved in the schedule allocated for this project. Failure of a cold bushing could spoil the vacuum used for electrical insulation in the termination and result in a breakdown of line voltage to ground. Therefore, it was decided that a more robust insulation system was needed, and a pressurized termination concept (T2) was developed in a several-month period in early 1999. The pressurized termination design is elegant but simple.

- There are no cold inner or shield bushings, just two warm bushings per termination.
- There is no dynamic vacuum system. (There is a static vacuum system with multiple layers of superinsulation for thermal insulation.)

- There is a simplified flange and bus arrangement.
- There is the goal of a reliable design.
  - The entire termination is at the cryogenic system pressure, and there is a natural thermal transition from liquid nitrogen to gaseous nitrogen along the copper conductor pipes.
  - An external leak reduces pressure to atmospheric nitrogen pressure (30 kV/cm), and the system is designed to avoid breakdown in a leak to atmosphere.
  - The termination uses traditional and easier-to-assemble ASA-type flanges and pressure sensors; electric utilities have more experience with these components.
- There is less expense.
  - It eliminates expensive equipment such as a turbomolecular vacuum pumping system and leak detectors.
  - It saves development and production costs for cold bushings.
  - Fabrication costs are decreased for smaller pipes and tubes compared with a vacuum system.
- It is operationally efficient with the elimination of system pumpdown and vacuum leak testing.

It is designed for an 18-kV-ac withstand and a 110-kV basic impulse level (BIL) for 15-kV-class cable. T2 is also designed to maintain 7.2 kV phase-to-ground even with a leak resulting in depressurization to atmospheric pressure. The ac current capability is 1250 A, the same as that for the original vacuum termination (T1). T2 is more compact than T1; the inner diameter is limited to 6 in. to meet ASME code requirements. Pressure components are designed for a maximum operating pressure of 150 psi, but the system normally operates in the 60- to 90-psi range; overpressure protection is via burst discs/relief valves on liquid nitrogen input flanges. Design features were incorporated to minimize partial breakdown. A sketch of T2 is shown in Fig. 2.18.

A full-scale mock-up of the T2 electrical connections was fabricated. The T2 joint mock-up was designed to simulate an internal splice as well as the termination at the warm end of T2. It was tested in the high-voltage laboratory at ORNL with pressurized liquid nitrogen cooling. During ac withstand tests, there was no partial discharge up to 12.5 kV ac and 3–5 pC at 18 kV (2.5 times the operating voltage). Voltage was held at 18 kV for 30 min (12 mA leakage current) and then increased briefly to 40 kV with increased partial discharge. Next the mock-up cable was impulse tested. It withstood voltages at 123 kV and had a breakdown at 137 kV BIL. It withstood 123 kV again after this breakdown and had a second breakdown at 137 kV. These tests confirmed the electrical insulation design of T2.

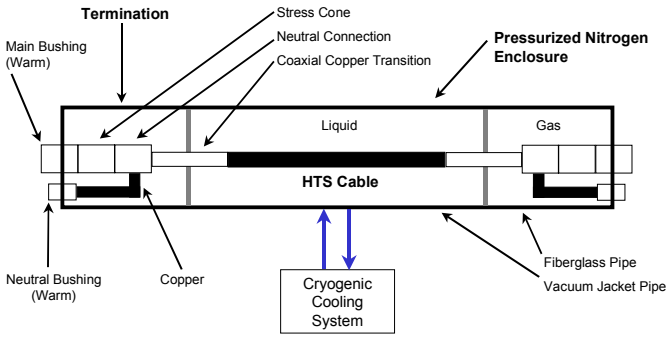

Fig. 2.18. Schematic of pressurized termination.

Next the actual T2 prototype terminations were tested in the ORNL 5-m cable test facility with 5-m HTS cable #2. The two T2 terminations and cable #2 have been through seven cooldown cycles. Cooldown can be accomplished in 1 to 2 h with no component being stressed by the rate of cooldown. Scans of dc current to about 1500 A on the center conductor were conducted. Next a 24-h run was completed at the design ac current, 1250 A, for most of the run, and 1400 A for the last 2 h. The dc V-I and ac losses on cable #2 were close to values measured earlier with T1. An ac withstand test at 18 kV ac for 30 min was successfully completed with no breakdown. Next, a long run (72 h) at design conditions of 7.2 kV and 1250 A ac was carried out. The final ~7 h were at 10 kV. As seen in Fig. 2.19, system temperatures were stable throughout the 3-day run.

During this last test, the heat load of the two T2 terminations and the cable and the liquid nitrogen pressure drops were quantified (Fig. 2.20); this information was needed for the 30-m system design.

All T2 tests met or exceeded design requirements. Based on positive results from the T2 mock-up electrical testing and T2 prototype testing in the 5-m test facility, Southwire has adopted the T2 pressurized termination design (with some revisions) for the 30-m, three-phase demonstration.

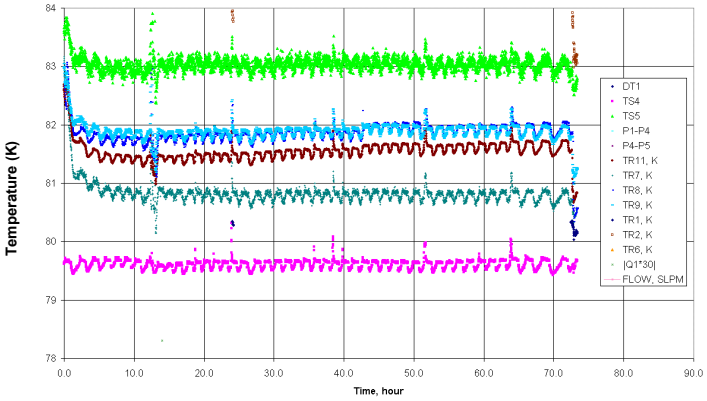

Fig. 2.19. Cable and termination temperatures during the T2 72-h run.

2.1.9 Summary

In FY 1999, our CRADA partner Southwire machine wrapped a second 5-m HTS cable and three 30-m HTS cables. Testing of two 5-m cables and an alternative cable termination at ORNL successfully validated the HTS cable performance and the overall system design. Dielectric testing of model cables at ORNL validated the cable electrical insulation system design. The electrical performance and mechanical performance of superconducting tapes were measured at ORNL. The design of the 30-m HTS cable and supporting subsystems (cable terminations and cryogenic cooling system) was finalized in a team approach with Southwire.

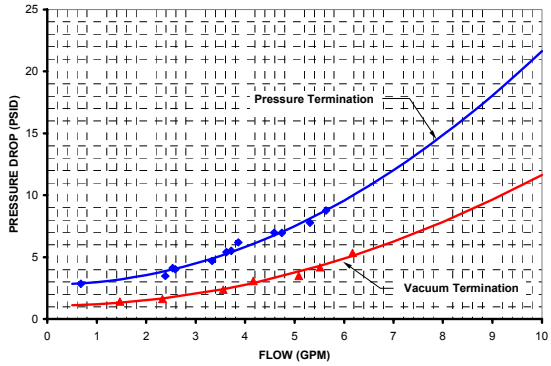

Fig. 2.20. Pressure drop as a function of flow for T1 and T2.

2.1.9.1 Cable Manufacture

For this project, Southwire has built a special superconducting-cable-manufacturing facility in a clean room environment. A cable wrapping or stranding machine has been acquired and modified for winding superconducting cables. In FY 1999, a second 5-m HTS cable was machine-wound to further test the modified stranding machine. After successfully completing this cable, Southwire has wound the three HTS cables for the 30-m SPI project. The critical current of each 30-m cable has been measured, and all three have met the required current specification. The cables were ready for installation at the end of FY 1999. Each cable uses a coaxial conductor configuration with the conductor wrapped from bismuth-strontium-calcium-copper oxide (BSCCO 2223) superconducting tapes.

2.1.9.2 Cable Testing

A rigorous testing program was conducted to measure the performance of two 5-m HTS cables. Test results show both cables meeting or exceeding the design parameters. The dc characteristics of both of the cables have been measured at temperatures between 72 and 82 K. The critical currents were found to increase linearly with decreasing temperatures in this range. The ac loss of the cables was measured as a function of current at several different temperatures; ac losses of 1 W/m for the first cable and 0.7 W/m for the second cable were measured at the design current of 1250 A rms. The ac losses were also found to scale as the ratio of ac current to the critical current as predicted by Dresner's theory.

High-voltage testing of the cable-termination system proved the integrity of the cold dielectrics and the termination design. Both of the cables and the terminations surpassed the 2.5 times operating voltage (18 kV) without breakdown. Both cables have been operated for extended periods of time (up to 72 h) stably at the rated 7.2 kV line-to-ground voltage and the rated 1250 A current continuously. Initial impulse tests were conducted on a prototype 5-m cable at impulse levels up to 75 to 80 kV. An alternative pressurized termination (T2) has been designed, jointly built, and tested successfully. All hardware was provided by Southwire Company. System heat loads, liquid nitrogen flows, and pressure drops have also been measured.

2.1.9.3 HTS Conductor

The mechanical and electrical performance of short samples of superconducting tapes to be used in the 30-m cable were measured. The performance of superconducting tapes purchased by Southwire continues to improve. The short-circuit performance of short samples of superconducting tape was measured.

2.1.9.4 Cryogenic Dielectric Research

The cable electrical insulation system uses a lapped or wrapped dielectric tape (Cryoflex) immersed in liquid nitrogen and pressurized to suppress the formation of bubbles. Performance criteria were established for the cable insulation system for ac breakdown, impulse breakdown, and partial discharge. To determine the cable insulation system performance, a series of model cable tests were conducted during FY 1999 at ORNL. A model cable is 1 m in length and simulates the construction of the entire electrical insulation system for the 30-m HTS cable. Based upon the results of the model cable tests, the partial discharge, ac breakdown, and impulse breakdown were found to meet and exceed the established criteria, thereby validating the insulation system design for the 30-m HTS cable. In addition to model cable tests, impulse breakdown tests were performed on both a ceramic and a nonceramic cryogenic bushing to determine their electrical performance. A cable-termination model was constructed and tested for partial discharge, ac breakdown, and impulse breakdown to validate the cable termination design.

During the past year, the project team has used the expertise of many individuals from Southwire and ORNL in an integrated team approach. In addition, private consultants, cryogenic equipment manufacturing firms, and superconducting materials suppliers have been sought out for expertise and advice. Many major components of the 5-m cable system were procured from subcontractors. The design, assembly, and operation of the Southwire/ORNL HTS Cable Test Facility have been carried out in a totally integrated effort drawing upon scientists, engineers, and technicians from Southwire, ORNL, and private industry. During FY 1999, presentations on this project were made at the IEEE Winter Power Meeting, the IEEE T&D Conference and Exposition, Workshop on ac Losses (WACL 99), the DOE Wire Workshop, and at other venues. Two technical papers were presented in July 1999 at the Cryogenic Engineering Conference.[1,2]

2.1.10 References

1. J. W. Lue et al., “Phase HTS Transmission Cable Tests,” 1999 Cryogenic Engineering and International Cryogenic Materials Conference, July 12–16, 1999, Montréal, Québec, Canada.

2. J. A. Demko, et al., “Cryogenic System For A High Temperature Superconducting Power Transmission Cable,” 1999 Cryogenic Engineering and International Cryogenic Materials Conference, July 12–16, 1999, Montréal, Québec, Canada.

3. J. W. Lue, et al., “AC Losses of Prototype HTS Transmission Cables,” paper presented at the 1998 Applied Superconductivity Conference, Palm Desert, California, Sept. 13–18, 1998.

4. M. J. Gouge, et al., “HTS Cable Test Facility: Design and Initial Results,” paper presented at the 1998 Applied Superconductivity Conference, Palm Desert, California, Sept. 13–18, 1998.

5. L. Dresner, "Hysteresis Losses in Power-Law Cryoconductors, II," *Applied Supercoductivity* **4**(7/8), 337–341 (1996).

6. L. Dresner, "AC Losses in Transmission Line Cables," paper MM2 presented at ICMC98, U. Twente, Netherlands, May 10–13, 1998.

7. F. J. Kadi and R. C. Longsworth, *ASME Journal of Engineering for Industry*, August 1977.

2.2 SUPERCONDUCTING TRANSFORMER PROJECT

S. W. Schwenterly, B. W. McConnell, I. Sauers, and D. R. James

In Phase I of the Superconducting Transformer Project, an experimental prototype 1-MVA, single-phase transformer was built and tested. The objective of the current Phase II Superconductivity Partnership Initiative (SPI) is to demonstrate technical and economic feasibility with an alpha-prototype 5/10-MVA 3-phase HTS transformer to be operated long-term, supplying power from the utility grid to the main Waukesha Electric Systems (WES) plant in Waukesha, Wisconsin. During FY 1999, an inspection and further tests were performed on the 1-MVA prototype transformer to determine the cause of the 11-kV tripoff that occurred during the original operating tests. The team met several times to consider conceptual designs for a commercial 30-MVA transformer, which is the ultimate goal of the project. It was decided that the 5/10-MVA transformer design should be carried out as a scaled-down version of the final 30-MVA design. An extensive program of electrical insulation tests was begun to validate the capabilities of vacuum, solids, and liquid cryogens to handle 550-kV BIL levels and to develop design rules for full-scale systems. Preparations began for further ac-loss tests.

2.2.1 Inspection and Further Testing of the 1-MVA Transformer

During the FY 1998 operational testing of the prototype 1-MVA transformer, resonant-circuit power tests were alternated with open-circuit high-voltage tests in a stepwise fashion. During an open-circuit test at 11 kV, a high-voltage supply tripoff occurred, after which voltages above 5 kV produced high partial discharge. In March 1999, the transformer was untanked and inspected at WES to determine the cause of the tripoff. The interior of the liquid nitrogen tank and the current leads up to the bushings had already been inspected (by means of a fiber-optic bore scope) in February and had been found to be in good condition.

Superinsulation blankets consisting of about 27 layers of thin aluminized Mylar surround the heat shield around the winding. The aluminum thickness on each layer is about 5×10^{-8} m. A 1.3-cm hole was found burned into the first seven layers of superinsulation in one location. A vertical split about 5 cm long was found in the ten innermost layers of the blanket directly under the large hole on the outside. This was directly over a vertical slit that had been cut in the shield for stress relief. The Mylar was blackened around this area as if it had been exposed to heat or electrical discharge (Fig. 2.21). There were ten layers of undamaged superinsulation between these two punctures. A much smaller hole, found about one-fourth of the way around the shield from the first hole, went in only a few layers. No further damage was found in the superinsulation. Both of the holes were roughly even with the top turn of the high-vacuum (HV) winding. This end was grounded during operation so that there was no high voltage under the damaged superinsulation. The shield itself is grounded to the core in such a way that it does not constitute a shorted turn around it. There was no evidence of any arcing on the interior walls of the vacuum tank.

Fig. 2.21. Split in inner shield superinsulation.

After the shield sections were removed, inspection of the shield interior surfaces and external winding areas showed that all components were in good order, with no evidence of arcing. A fiber-optic bore scope was used to inspect highly stressed internal areas of the winding. No damage was found. The bottom of the current feedthrough in the liquid nitrogen tank was carefully inspected and was also found to be undamaged. No evidence of arcing appeared around any of the winding terminals or other highly stressed areas. The numerous instrumentation leads entering the winding had originally been suspected as causes for the breakdown. However, no damage was found on these leads. Megger tests at 600 Vdc on critical components showed no problems. Transformer ratio test results as well as voltage-tap resistance readings agreed well with the original values, indicating that there were no shorted turns.

Because the coil insulation appeared to be undamaged, it was decided after careful consideration of the ground clearances that it was safe to perform a low-current open-circuit test on the coils to full voltage in air. Current vs voltage readings agreed perfectly with the 1998 data, as shown in Fig. 2.22. The maximum operating voltage of 13.8 kV could be applied. Further tests were performed to verify that the transformer would run properly with the shields and the superinsulation carefully installed to prevent shorts. A maximum voltage of 13 kV could be applied in this situation. The voltage was limited by flashover at the liquid nitrogen tank feedthrough, which had marginal clearances for air operation. This would not have occurred under normal operating conditions. No hot spots were found in the superinsulation. When deliberate shorts were made between the SI blankets, faint ticking and buzzing could be heard inside them, and a burned area developed near one of the clip leads.

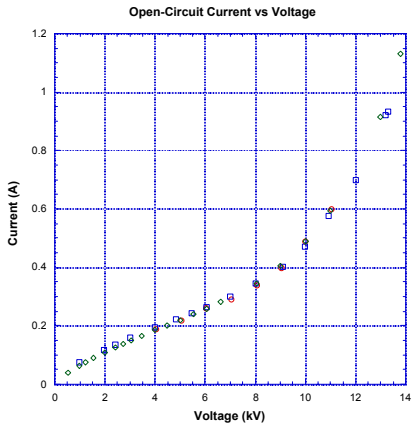

Fig. 2.22. Open circuit current vs voltage. Circles; 3/23/98. Squares and diamonds; 3/30/99.

Because the full operating voltage was reached in room-temperature air under much lower dielectric strengths than the winding would see in vacuum at operating temperature, it appears that high-voltage breakdown was not the cause of the tripoff in the 1998 tests. The only damage found was in the form of burn marks in the superinsulation. The burn marks were on the outside of the grounded shield and were adjacent to areas of the winding that were very close to ground potential. Thus it seems unlikely that they could have been caused by high-voltage breakdown. A possible alternative explanation is that the burned areas were caused by eddy currents induced in the aluminizing by the ac field. Three scenarios are possible (see Fig. 2.23).

1. Radial leakage fields penetrate the superinsulation layers perpendicularly and cause eddy-current heating.
2. Axial leakage fields in the superinsulation parallel to the layers could cause circulating currents in the aluminizing if some of the layers contact each other at their edges to form a closed loop. A second possibility is that the shield itself on one side could form the loop; the induced current would then return through one or more superinsulation layers on the other side.
3. Contacts between the various superinsulation blankets at their edges form a complete loop around the core and have the potential to induce large currents in the aluminizing.

The heating caused by each of these scenarios can be estimated with Maxwell's equations. It can be easily shown that heating is negligible for the first two scenarios, mainly because the leakage fields are small. For the third scenario, the situation is much different. At 11 kV, enough flux is in the core to induce 38 V per turn. The resistance at 77 K for one layer of superinsulation on the outer shield cylinder making a complete turn around the core can be calculated easily from the aluminum resistivity and the layer dimensions. The power V 2/R works out to about 7.7 kW for each single layer. The actual power was

probably lower because of resistance at the superinsulation blanket edges and because of higher resistivities in the outer, warmer layers, but substantial heating is definitely possible. Because the superinsulation layers are very thin, high electric fields could develop at their edges even at 38 V, leading to field emission and arcing in vacuum. It is not clear why the heating was concentrated at only the two spots where the burnouts occurred. However, when the layers are packed closely together, such as where they crossed the edge of the shield slit at the large hole, it seems possible that hot spots and burnouts could develop there. Because the closely packed layers draw energy from the high-voltage supply, they could easily have caused a tripoff. Intermittent arcing between the edges of the various blankets could have produced a signal that would have looked very similar to partial discharge.

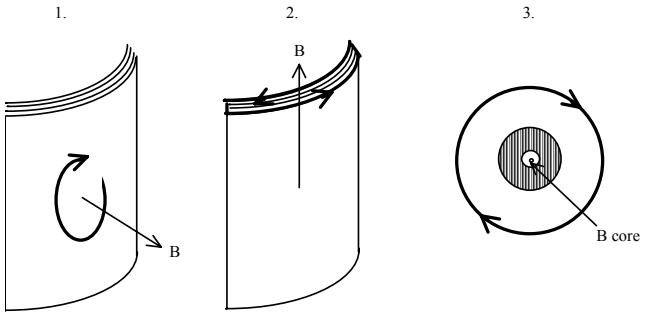

Fig. 2.23. Induced current flow paths in superinsulation for three scenarios.

One might ask why there were no tripoff problems in the earlier short-circuit tests. The explanation is simple; with the secondary shorted, there is very little voltage per turn, and any power developed in a shorted superinsulation loop around the core would be low. These tests indicate that the superinsulation damage found after the FY 1998 tests was probably caused by short circuits between the blankets and that the transformer should operate properly when measures are taken to prevent these shorts.

2.2.2 AC Loss Testing

A new ac loss test sample was received from IGC in July 1999. This sample incorporates several design improvements that are expected to reduce ac losses in the conductor. Because the variable-temperature liquid helium cryostat used on the previous ac loss tests did not have very good temperature stability for calorimetric tests and was expensive to operate, we decided to mount the new sample on a new cryocooler purchased earlier in the year. Figure 2.24 shows a side view of the cryostat, which is mounted in a standard liquid helium dewar. The inner vessel of this dewar is evacuated to provide good thermal insulation for the cryocooler cold head and the sample. The dewar has its own liquid nitrogen shield, which will provide additional radiation shielding. The sample is thermally connected to the cold head through its leads and by sheet-copper straps between the cold head and the outer support structure of the sample. This cryostat is under construction, and tests are expected in the first part of FY 2000.

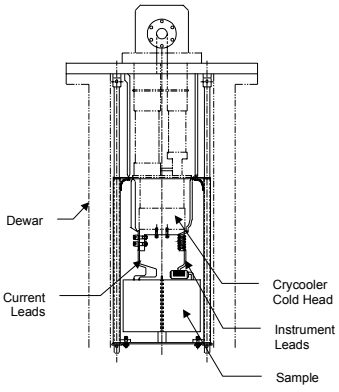

Fig. 2.24. Cryocooled ac loss test cryostat.

2.2.3 Transformer Design Studies

The team met on several occasions to work out conceptual designs for the 30-MVA transformer. The 5/10-MVA unit will incorporate several features of the commercial 30-MVA design to provide extended operation at twice rating, and to remain superconducting through a 10X fault current and a 3-day power outage. It will have basically the same physical size as the 30-MVA, 138-kV unit, but will have fewer turns in the coils, which is consistent with its 26.4-kV rating. Much of the effort was devoted to development of a dielectric design that could withstand the 550-kV impulse-voltage tests required for 138-kV equipment. ORNL took an active role in design of the bushing and lead configuration, electrical insulation, cryogenic system, and component layout. The preliminary

conceptual design has been completed, and detailed design is under way in order to provide a framework for the 5/10-MVA design effort. Figure 2.25 shows an external view of the 30-MVA transformer.

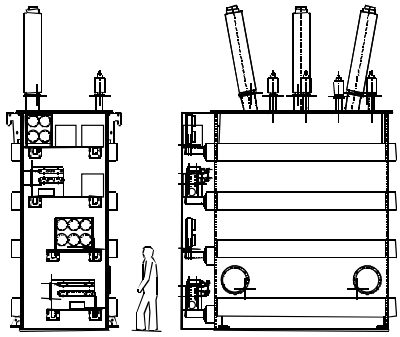

Fig. 2.25. External view of 30-MVA transformer.

2.2.4 High-Voltage Insulation Development

High-voltage insulation development efforts continued on both theoretical and experimental bases. A generic program addressed the issues of cryogenic electrical insulation systems at power systems voltage. Testing in support of preconceptual designs was conducted. The scaling of cryogenic electrical insulation data for area and volume effects to values approximating those found in the HTS transformer will require at minimum one-fourth-scale tests of bushings and other electric insulation components. Design of a test chamber for bushing tests and larger-scale tests on simulated coils and cryogenic assemblies is under way, and testing at laboratory scale continues. Results are summarized in Sect. 2.3 of this report.

2.3 INSULATION STUDIES AT ORNL IN SUPPORT OF SUPERCONDUCTING POWER APPLICATIONS

I. Sauers and D. R. James

ORNL is conducting research into the aspects of multicomponent insulation systems for use in power apparatus. During the past year, efforts have been concentrated on development of basic techniques for use in measurement and characterization of cryogenic insulation, construction of new apparatus, and application-specific testing of proprietary systems.

Insulation systems studies require a careful blending of basic, small-scale, scientific measurements and theory of dielectrics with larger, more elaborate sub-scale engineering studies. The small-scale studies provide guidance and understanding of the breakdown mechanisms and the initial information needed to design the sub-scale experiments. These latter sub-scale experiments are generally proprietary in nature, expensive, and crucial to the overall success of larger-scale applications.

Bulk breakdown of small-scale systems is well characterized in the literature; therefore, the program efforts are concentrating on the dielectric performance at the interface between two different insulating materials and large-scale studies of bulk performance. The systems under study include vacuum-solid, gas-solid, liquid-solid, and solid-solid interfaces. The dielectrics and high-voltage research facility includes a high bay, a high-voltage laboratory, and a control room for impulse testing cryogenic model cable; a laboratory where model cables can be constructed in-house; and another laboratory housing a shielded room for making partial-discharge and breakdown measurements. In addition, a new cryostat has been constructed to perform sensitive partial-discharge and aging studies on short lengths of model HTS cables.

During the past year, we have conducted research on surface flashover of fiber-reinforced epoxy composite [sometimes referred to as fiberglass-reinforced plastic (FRP)] insulation in vacuum at cryogenic temperature, high-voltage breakdown tests (including impulse, ac, and partial discharge) on lapped-tape/liquid nitrogen insulated model HTS cable, and breakdown tests of a new HTS termination design. We have also initiated new studies of partial-discharge and aging of model cables and breakdown and thermal tests of new solid epoxy dielectrics.

2.3.1 Surface Flashover of Fiberglass-Reinforced Epoxy Composite Insulation

2.3.1.1 Introduction

Following the development of HTS materials manufactured into practical conducting tapes, there has been renewed activity in the development of superconducting power equipment. In general, the electrical insulation for HTS power equipment will follow either of two design paths: vacuum insulation with solid spacer or solid-lapped tape insulation immersed in a cryogen (generally liquid nitrogen).[1–3] This section summarizes the preliminary data on solid spacer in vacuum design. Much of the past work in this area has focused on dc breakdown at room temperature and to a lesser extent ac and impulse voltage waveforms at cryogenic temperature. Dielectric materials that have been of particular interest are FRPs, which can have high breakdown puncture strength and has high mechanical strength.[4–6] An undesirable property is the tendency to outgas in a vacuum, which would could lead to lower-than-expected flashover strength. At low temperature, however, outgassing might be suppressed, leading to an improvement in the flashover strength. We will present preliminary data on the flashover strength at room temperature and low temperature, and we will compare these to a pure vacuum gap (for both cooled and uncooled electrodes).

2.3.1.2 Experiment

Vacuum Chamber and Electrodes

All breakdown experiments were conducted with "Rogowski" profiled stainless steel electrodes inside a stainless steel vacuum chamber that could be evacuated to pressures as low as 2×10^{-8} Torr using an 80-L/s turbomolecular pump bolted directly to the chamber. A more typical operating pressure was about one order of magnitude higher. The electrodes were 14 cm in diameter, and the central flat region was 25 cm^2 in area. Figure 2.26 shows the experimental apparatus that was used for all the high-voltage breakdown tests. Two electrode configurations were employed. In the first (Fig. 2.27), each electrode was mounted independently of the other; ground electrode was attached to a linear-motion drive connected to vacuum feedthrough so that the gap could be adjusted externally for studies of pure vacuum gaps of varying lengths. This configuration was also used for some of the surface-flashover studies in which a solid dielectric disk was placed on the bottom (ground) electrode and this electrode was adjusted so as to place the disk in contact with upper high-voltage electrode (Fig. 2.28). In the second arrangement (Fig. 2.26), both electrodes were mounted in a frame consisting of either G-10 or teflon posts, and the entire assembly was supported from the same flange (which also supported the high-voltage bushing.) There were also provisions for cooling either or both electrodes. This was done by placing a metal (either

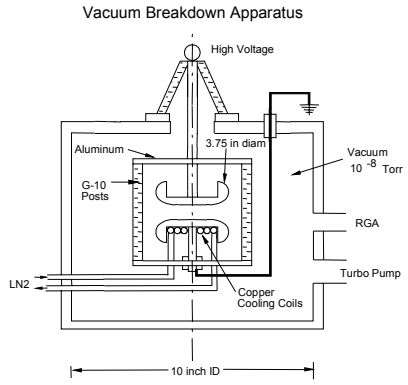

Fig. 2.26. Vacuum breakdown apparatus.

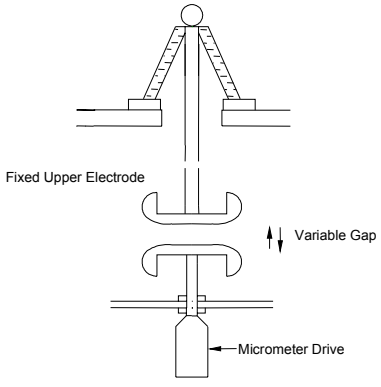

Fig. 2.27. Adjustable electrode arrangement.

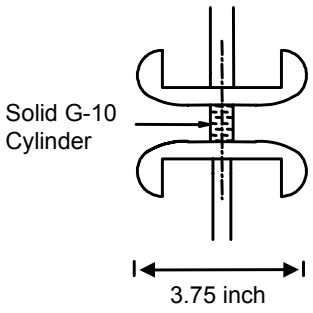

Fig. 2.28. Electrode-solid sample arrangement.

copper or stainless steel) coil on the back of each electrode. The coils were connected to flexible tubes for electrical isolation. However,problems were experienced with partial-discharge-induced failure of the tube used for the high voltage electrode isolation. Therefore, it became necessary to cool only the ground electrode, although this electrode could still be isolated from ground, permitting partial discharge measurement and breakdown current for triggering a digital oscilloscope.

Dielectric Materials

Two forms of FRP with commercial designations, G-10 and G-11, were obtained from two sources as either solid rod or tube and then were cut to various lengths. The samples were cleaned with methanol and are dried in a vacuum oven. No other cleaning techniques were employed, and the microscopic surface condition was not further characterized. The samples were placed at the center flat region of the profiled electrodes butting against both electrodes; that is, the electrodes were not recessed, and no metallized coating was applied to the dielectric samples to improve electrode contact. It is known, however, that these techniques help to suppress electron emission at the cathode triple junction (which for ac voltages can be either electrode), resulting in higher surface flashover breakdown strengths.[7–9] The disk and tube specimens were 3.8 cm and 1.3 cm in diameter, respectively.

High-Voltage Supplies and Electronics

Power-frequency (60-Hz) ac breakdown measurements were made using a Phenix Technologies 150-kV, 20-mA power supply. Impulse breakdown (1.2/50 μs rise/fall time) measurements were made using a Haefely Marx bank generator (500 kV maximum). However, limitations of the high-voltage bushing restricted the experiments reported here to vacuum gaps up to 3 mm and the dielectric spacer length to 50 mm. Voltage waveforms were fed into a digital oscilloscope, which was triggered upon breakdown (either from the current surge or a voltage drop). The breakdown voltage was then determined from the last voltage reading before breakdown. This value was also consistent with the last-held value on the Phoenix supply and the peak reading voltmeter on the Haefely impulse generator.

Mass Analysis

The chamber was also equipped with a residual gas analyzer (MassTorr) with a mass range of 2 to 100 amu, permitting an examination of the quality of the vacuum and, in some cases, a diagnostic on the type of breakdown (i.e., gap breakdown or surface flashover). The primary contaminants at room temperature were water and air.

2.3.1.3 Results and Discussion

Measurements of the ac breakdown strength of the vacuum gap were made for electrodes cooled with liquid nitrogen and at room temperature. In either case, electrode conditioning was observed in which the breakdown voltage increased with breakdown number before reaching a plateau. The rise in breakdown voltage varied from experiment to experiment, presumably because of unknown surface conditions and prior breakdown history of the electrode. Figure 2.29 shows an example of the conditioning process, showing approximately a twofold increase of the conditioned value over the first breakdown. Unless otherwise noted, the breakdown values given are the conditioned values, and the reported voltages are the ac rms values. The field strengths are determined by dividing the ac rms values by the gap or spacer length (in millimeters). In cases where several experimental runs were made, the “conditioned” values were averaged and the mean value is reported.

AC Breakdown in Vacuum at Room Temperature

The ac breakdown voltage, V_b, generally increased with gap length, d. Figure 2.30 shows the dependence of breakdown voltage with gap for small gaps and the decrease in breakdown strength for one set of data at the largest gap of 2 mm. The breakdown-field-strength data from several data runs, shown in

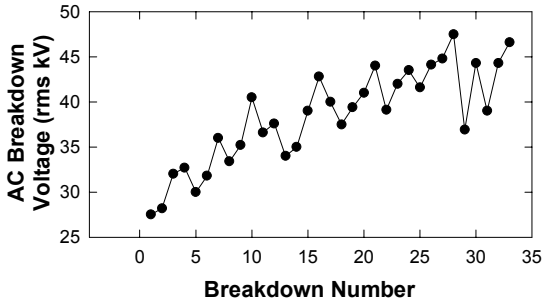

Fig. 2.29. Breakdown as a function of breakdown number showing conditioning.

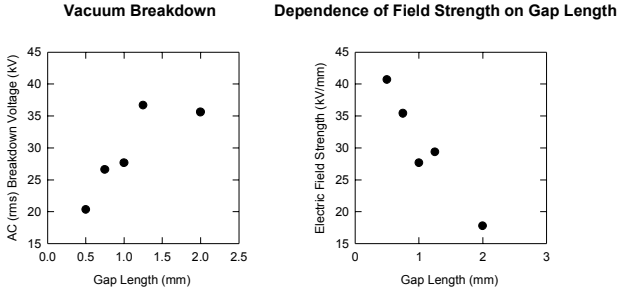

Fig. 2.30. Breakdown voltage and corresponding field strength as function of gap length.

Fig. 2.31 (along with the surface flashover data), yields a voltage dependence (in kilovolts) on gap length (in millimeters) given by

$$V = 24.9 \times d^{0.59}$$

and electric field (in kilovolts per millimeter) dependence on gap length (in millimeters) given by

$$E = 24.9 \times d^{-0.41}$$

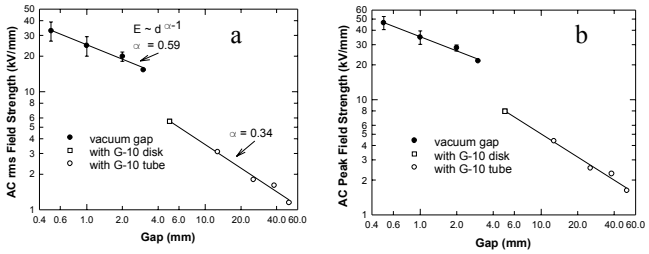

Fig. 2.31. AC rms (*a*) and ac peak value (*b*) field strength of G-10 spacers and pure vacuum gap as a function of gap length.

The voltage dependence is consistent with the roughly $\sqrt{d}$ dependence reported by others where values of the exponent in the range of 0.4 to 0.6 have been found.[10] The error bars in Fig. 2.31 represent the standard deviation of the mean values of the data.

Comparison of cold vs room temperature (Table 2.2) indicated an increase in field strength of 30% for room-temperature electrodes over that of cold-temperature electrodes for a 2-mm vacuum gap. In the table, V_b (peak) is the peak voltage of the 60-Hz waveform and is $\sqrt{2} \times V_b$, max, the maximum rms breakdown value measured.

Table 2.2. Effect of temperature on a 2-mm vacuum gap

Temperature (K)	Breakdown voltage V_b (kV)			
	V_b, mean	$\pm \Delta V$	V_b, max	V_b (peak)
300	38.2	6.7	46.3	65.4
90	27.8	3.5	34.9	49.4

AC Surface Flashover for G-10 Disk and Tubes

Fiber-reinforced plastic, G-10 and G-11, were tested in cylindrical disk form. The disks were 5 mm thick and 38 mm in diameter. For the G-10 samples, the fibers were oriented perpendicular to the electric field; for the G-11 samples the disks were cut so that the fibers were oriented parallel to the field. All breakdowns observed for the G-10 disks were flashover (i.e., no breakdowns resulted in puncture), but flashover occurred along (or near) the disk surface. In the case of flashover, no surface damage could be observed by the unaided eye. However, in the G-11 sample, in which the fibers ran parallel to the field, punctures were observed at a voltage below the voltage needed to flashover. Figure 2.32 shows a photograph of a failed sample of G-11. Table 2.3 lists the results. Low breakdown voltages caused by breakdown along the fibers have also been reported by Park et al.[4]

Table 2.3. Effect of material fiber orientation on breakdown

Orientation	Material	Breakdown voltage (kV)	Process
Normal to fibers	G10	28	Surface flashover
Along fibers	G11	10-15	Puncture

One set of data (Table 2.4) was taken for the 5-mm G-10 disks at low temperature (~90 K) and at room temperature (~300 K). Very little difference was observed, which may seem surprising because the G-10 suffers from the problem of outgassing. Although very little heat (< 0.1 mW) is generated in these samples based on calculations of power losses (using a $\tan \delta = 1 \times 10^{-3}$), desorption of condensed gases can

Fig. 2.32. Breakdown along the fibers of G11 leading to puncture.

Table 2.4. Effect of temperature on breakdown of 5-mm-thick G10 disk

Temperature (K)	Breakdown voltage, V_b (rms kV)			
	Mean	$\pm \Delta V$	Max	V_b, peak
300	27.3	2.8	31.9	45.1
90	25.3	2.4	29.4	41.6

occur via electron impact processes. Tourreil[11] observed a decrease in hold-off strength for several materials when cooled to liquid-nitrogen temperatures, which may be attributed to heating during the conditioning process.[12] Other researchers[13] have observed little or no difference between room temperature and 100 K for lexan (polycarbonate).

We have also tested 12.7-mm-diam tubes made of G-10 in lengths ranging from 12.7 to 50.8 mm (0.5–2 in.). The dependence of flashover voltage (kilovolts) with length (in millimeters) is given by

$$V = 16.4 \times d^{0.34} .$$

Breakdown field strength dependence on length given by

$$E = 16.4 \times d^{-0.66} .$$

These measurements were made at room temperature. The data are also presented in Fig. 2.31, along with the vacuum-gap data. The voltage dependence on tube length appears to follow a $\sqrt[3]{d}$ dependence. As can be seen from the data in Fig. 2.31, the electric field strength falls to about 1 kV/mm for 50-mm lengths at G-10 tube. Hawley[14] reported the work of Ramm,[15] who measured the breakdown strength of a long (65-cm) insulator to be around 390 kV, yielding the very low field strength of 600 V/mm. The present data also indicate very low (sub-kilovolt) strengths for long dielectric spacers. Table 2.5 lists the ac surface-flashover strengths of a few selected materials reported in the literature,[11, 16, 17] including the present data on FRP.

Impulse Breakdown of G-10 Disk

One set of data was taken of the impulse breakdown (negative polarity) of 5-mm G-10 disks in vacuum. The highest withstand voltage measured was 49 kV; the lowest breakdown voltage measured was 51 kV. This gives an impulse-to-peak ac-breakdown ratio of approximately 1.4.

2.3.1.4 Summary

Sixty-cycle ac and negative-polarity impulse tests have been made on FRP disks and tubes. The breakdown strength is lowered considerably from a pure vacuum gap. Lowering the temperature of FRP has little effect on the surface flashover strength and, if anything, tends to lower the strength slightly. This may be due to electron-impact desorption of condensed gases from the dielectric surface during the conditioning process. The appearance of glows near the surface during breakdown tends to support this view. The merit of using FRP as spacer material in low-temperature vacuum applications is not clear based on the present data, suggesting that additional work is needed. Furthermore, the significant lowering of the flashover strength with insulation length indicates that experimental data are needed on large bridged vacuum gaps at cryogenic temperatures, not only for FRP, but for other dielectric materials as well, for designing large-scale HTS equipment.

2.3.2 Studies of Lapped-Tape (Cryoflex)/Liquid-Nitrogen Dielectric

Model cables were constructed by wrapping the Cryoflex dielectric around a 4-ft mandrel with stress cones to reduce the electric field at each end. The test cables were immersed in pressurized liquid nitrogen to reduce the deleterious effects of bubbles. (Bubbles tend to reduce breakdown strength.) The high-voltage tests included impulse breakdown, having a waveform with a 1.2-μs rise time and 50-μs fall time; a 60-Hz ac breakdown test; and partial discharge measurements. Figure 2.33 shows the results of negative-impulse-voltage breakdown of Cryoflex-insulated model cable over a range of pressure, showing very little, if any, pressure dependence and an average value of 160.6 kV. Because the BIL requirement for this

Table 2.5. Comparison of surface flashover strengths of various materials

Material	Length (mm)	E_b (kV/mm)	Reference
Fused quartz	22.5	2.9	*a*
Polyethylene	16	5.6	*b*
Polycarbonate	16	6.3	*b*
Pyrex glass	4	11.5	*c*
Pyrex glass	22.5	2.0	*a*
Polystyrene	22.5	3.3	*a*
Plexiglass	4	12.0	*c*
Nylon	16	6.3	*b*
Teflon	4	10.9	*b*
Teflon	16	5.0	*b*
Teflon	22.5	2.2	*a*
PRF (G10)	5	6	Present
PRF (G10 tube)	50.8	1.6	Present

[a]P.H. Gleichauf, "Electrical Breakdown over Insulators in High Vacuum," *J. Appl. Phys.* **22**(6), 766-71 (1951).
[b]A.S. Pillai and R. Hackam, "Surface Flashover of Solid Insulators in Atmospheric Air and in Vacuum," *J. Appl. Phys.* **58**(1), 146 (1985).
[c]C. H. de Tourreil, "Surface Flashover Voltage of Spacers in Vacuum at Cryogenic Temperatures," *Advances in Cryogenic Engineering,* 22:306 (1977).

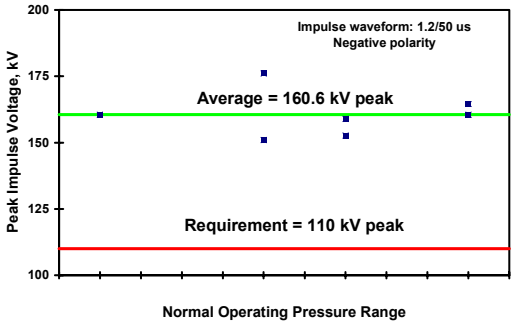

Fig. 2.33. Impulse breakdown strength as a function of pressure. Experimental values are indicated by the solid squares and the solid lines indicate the mean value (upper line) and cable requirement (lower line).

cable is 110 kV, the electrical insulation exceeds the requirement by 45%. Similarly, the ac breakdown tests indicated that the dielectric strength exceeds the requirement (in this case, 18 kV rms) by 290% (Fig. 2.34). The ratio of impulse strength to ac strength was found to be 2.3. When the number of layers of Cryoflex was varied from half the standard design, 0.5 *N*, to *N* the impulse breakdown strength increased approximately linearly as indicated in Fig 2.35. Partial-discharge measurements made at the onset voltage (24 kV) showed partial discharge pulses at the peaks of the ac waveform (Fig. 2.36). The partial-discharge charge amplitude was less than 5 pC at 21.6 kV, meeting the dielectric requirements for the cable.

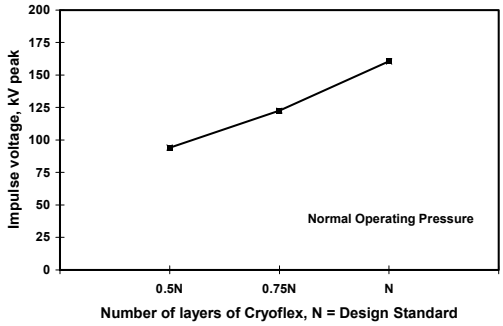

Fig. 2.34. Impulse breakdown strength as a function of insulation thickness, by varying the number of layers from half the design standard, 0.5 *N*, to the design standard, *N*.

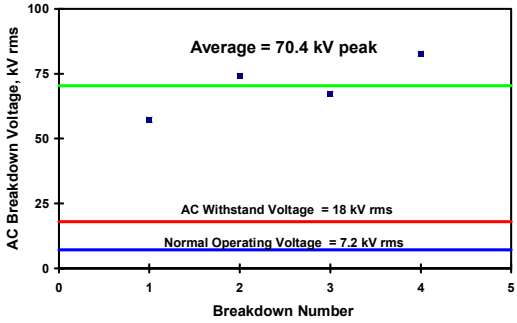

Fig. 2.35. AC rms breakdown strength of Cryoflex insulated model cable. Experimental data are indicated by the solid squares and the solid lines from top to bottom are the mean value, the ac withstand requirement, and the normal operating voltages, respectively.

2.3.3 Partial-Discharge and Aging Studies for HTS Model Cables

The failure mechanism of a HTS cable is expected to be caused primarily by partial discharge occurring in the lapped-tape liquid nitrogen dielectric system. Experiments to assess the expected life of the cable have been initiated. Two different apparatuses are being used: the large cryostat that was used for the breakdown studies of 4-ft model cable, and a second cryostat recently constructed to study shorter (2-ft) model cable (similar in design to the 4-ft cable). The second cryostat has the provision of making sensitive partial-discharge measurement on both the center of the cable and the stress cones. When a high-voltage stress, V, is applied to a cable, the time-to-breakdown, t, is generally related to the stress by the power law relation, $t \times V^n = \text{const}$, where n depends on the thickness and type of dielectric. Assuming that this relationship is valid for HTS cable, a determination of n from aging experiments conducted at different voltage stresses can be used to determine the expected life of a cable at its operating stress. Of course, in the field, a cable will experience overvoltages due to switching or lightning surges that can accelerate the aging and can thus shorten the cable life. An aging test was performed on a model at a voltage stress of 5 kV below the breakdown voltage. The cable failed after about 30 s. Other aging tests will be performed over a range of voltage stresses to establish the value of n for the Cryoflex dielectric, which is used on the Southwire HTS cable. Because partial discharge leads to dielectric failure, we will monitor the partial-discharge onset voltage. Subsequently, we will look at partial discharge at the stressed voltage to correlate time-to-failure with the level of partial discharge.

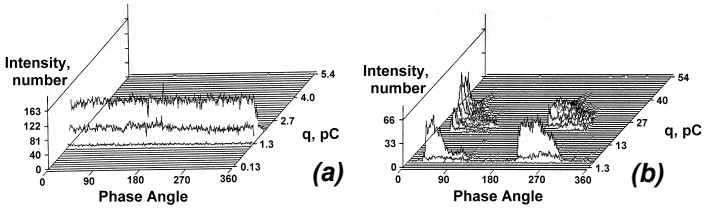

Fig. 2.36. 3-D plot of partial discharge intensity as function of phase angle and pulse size (in pC). (*a*) Background signal at 18 kV; (*b*) PD at the onset at 24 kV.

2.3.4 Hardware Development

A suitable arrangement has been chosen that should keep inductance barely low enough to avoid pulse ringing while keeping capacitance low enough to avoid more broadening of the pulses than is desired. (Some broadening is desired.) The inductance and capacitance are inversely proportional.

Three circuits have been designed, built, and tested to support the partial discharge/aging studies of solid cryogenic insulation in liquid nitrogen with ac high-voltage stress. Two circuits, fast-pulse-acquisition boxes, connect on the chamber exterior and provide three functions:

- they receive the fast partial-discharge pulses and pass them to preamplifiers;
- they remove 60-Hz signal, which is generally much larger than the pulses; and
- they survive a breakdown in the chamber (which partially connects the signal lead to the high voltage) and keep the large currents and voltages from damaging the preamplifiers and other sensitive connected devices.

The third circuit, a phase/Lissajous figure box, provides certain signals when observing partial discharge pulses from a separate acquisition circuit. The signals are needed for data receptors such as computers or oscilloscopes. Future adjustments may be required to best interface with given acquisition circuits and data receptors when they are identified.

The first function is to provide a signal representing the instantaneous phase of the 60-Hz signal (independent of amplitude), primarily for a computer that is acquiring partial discharge pulses. The computer then knows the phases when pulses occur. Inputs/outputs are provided for choosing the ac waveform, viewing the processed ac waveform, adjusting the signal scale, defining where zero phase is on the AC waveform, providing pulses marking zero phase occurrence, and providing the phase signal.

The second function is to form a Lissajous figure with partial-discharge pulses superimposed, primarily for an oscilloscope. Inputs/outputs are provided for introducing partial-discharge pulses and for choosing the amplitude, phase, and direction of the Lissajous figure, as well as for the two signals required for the figure.

Aging and partial-discharge experiments using the new high-pressure dewar (Fig. 2.37) will be performed in the next year. Higher accuracy on the expected life will be obtained for longer aging times (on the order of days or weeks); therefore, an automatic liquid nitrogen fill system will also be obtained.

Fig. 2.37. Partial discharge and aging pressurized cryostat for short-length (2-ft) model cables. Partial-discharge pulses can be monitored on the ground side of the cable.

2.3.5 Epoxy Dielectric Studies

Studies have been initiated on the breakdown strength and thermal properties of various formulations of solid epoxy-hardener combinations at room temperature and at cryogenic temperatures. For practical HTS applications, epoxy dielectrics must have high hold-off voltage strength, good thermal properties (including resistance to cracking through multiple cooling cycles), low partial discharge, and low tan delta (a measure of the power losses when ac voltage is applied). ORNL is working with manufacturers of epoxy materials to screen materials for testing at the ORNL high-voltage lab. Initial studies on one candidate epoxy-hardener combination were made with stainless steel electrodes with sphere-sphere and plane-plane geometries for different gap lengths at room temperature. Plane-plane geometry yields lower strength because of area effects. Thermal shock tests indicated heavy cracking after immersion in liquid nitrogen. Other candidate materials will be examined during the next year.

2.3.6 References

1. H. Fengnian and W. Weihan, “Electrical Breakdown of Vacuum Insulation at Cryogenic Temperature,” IEEE Trans. on Elect. Insul. **25**(3), 557 (1990).

2. J. Gerhold, "Properties of Cryogenic Insulants," *Cryogenics* **38**(11), 1063 (1998).

3. M. Kosaki, M. Nagao, N. Shimizu, and Y. Mizuno, "Solid Insulation and its Deterioration," *Cryogenics* **38**(11), 1095 (1998).

4. C. H. Park, M. Hara, and M. Akazaki, "Effects of Mechanical Stresses on the Dielectric Breakdown Strengths of PET and FRP," *IEEE Trans. on Electr. Insul.* **EI-17**(3), 234 (1982).

5. C. H. Park, M. Hara, and M. Akazaki, "Effects of Mechanical Stresses on the Dielectric Breakdown Strengths of PET and FRP Under Mechanical Stresses," *IEEE Trans. on Elect. Insul.*, **EI-17**(6) 546 (1982).

6. G. Lupo et al., "A Methodological Approach for Improvement of Vacuum-Insulated HV Bushings," in *Proc. XVII Int. Symp. On Discharges And Elect. Insul. In Vacuum* (1996).

7. H. Craig Miller, "High Voltage Performance Characteristics of Solid Insulators in Vacuum," p. 299 in *High Voltage Vacuum Insulation*, ed. R. V. Latham, Academic Press, London (1995).

8. J. M. Wetzer, "HV Design of Vacuum Components," *IEEE Trans. on Diel. and Elect. Insul.* **2**(2), 202 (1995).

9. J. M. Wetzer, "Vacuum Insulator Flashover," *Proc. of the XVII Int. Symp. on Discharges and Electrical Insulation in Vacuum*, 449, Berkeley (1996).

10. R. V. Latham, "The Operational Characteristics of Practical HV Gaps," p. 48 in *High Voltage Vacuum Insulation, Basic Concepts and Technological Practice,* ed. R. V. Latham, Academic Press Limited, London, (1995).

11. C. H. de Tourreil, "Surface Flashover Voltage of Spacers in Vacuum at Cryogenic Temperatures," *Advances in Cryogenic Engineering,* 22:306 (1977).

12. B. Mazurek, "High Voltage Vacuum Insulation at Cryogenic Temperatures," p. 487 in *High Voltage Vacuum Insulation,* ed. R. V. Latham, Academic Press Limited, London (1995).

13. A. Neuber, H. Krompholz, and L. L. Hatfield, "Dielectric Surface Flashover in Vacuum at Cryogenic Temperature (100 K)," *IEEE Annual Report—Conference on Electrical Insulation and Dielectric Phenomena,* 575 (1997).

14. R. Hawley, "Solid Insulators in Vacuum: A Review," *Vacuum,* **18**(7), 383 (1968).

15. C. A. Ramm, *International Conference on Instrumentation for High Energy Physics,* Berkeley, (1960).

16. A. S. Pillai and R. Hackam, "Surface Flashover of Solid Insulators in Atmospheric Air and in Vacuum," *J. Appl. Phys.* **58**(1), 146 (1985).

17. P. H. Gleichauf, "Electrical Breakdown over Insulators in High Vacuum," *J. Appl. Phys.* **22**(6), 766-71 (1951).

3. Summary of Technology Partnership Activities

3.1 BACKGROUND

Oak Ridge National Laboratory (ORNL) is a key participant in DOE's national effort on electric power applications of high temperature superconductivity (HTS). ORNL has formed effective teams that combine the resources of the Laboratory with the entrepreneurial drive of private companies. New technology partnership mechanisms, a feature of the ORNL Superconducting Technology Program for Electric Power Systems since its inception in 1988, have resulted in 41 superconductivity "pilot center" cooperative agreements and 7 cooperative research and development agreements (CRADAs). Eight agreements were active during FY 1999. In addition, licensing agreements, joint inventions, and joint publications with the private industry partners have ensured that there is technology transfer throughout the program.

Technology partnering on Laboratory–industry teams can occur in several ways. Spinoff technology partnering involves the licensing of patentable Laboratory inventions to industry, continued product or process development to the point of demonstration of precommercial viability, or both. In the ORNL program the cooperative development level of technology partnering is emphasized: joint Laboratory–industry teams work on a problem that (1) requires combined resources and expertise and (2) has a clear objective of precompetitive research and technology development. For the project to succeed, each partner depends on the success of the other. Most of the cooperative projects with private industry and the Laboratory precompetitive research and development projects are developing key technology in which commercialization of the results is expected to occur after a minimum of 3 to 5 years.

3.2 RELATIONSHIP TO THE DOE MISSION

The ORNL program mission is that of its program sponsor, DOE's Office of Power Technologies, Superconductivity Program: to develop the technology base necessary for industry to proceed to commercialization of electric energy applications of HTS. HTS will enable new energy-efficient motors, transformers, and transmission lines and will also provide electric power equipment manufacturers with strategic technology for global competitiveness. Electric utilities can defer acquisition of new transmission rights-of-way with successful introduction of superconducting cables. System stability and protection will be enhanced with the introduction of fault current limiters. Distributed utility systems in the future, which will include distributed generation systems, will benefit from the small size and weight of the next generation of electric power equipment. Finally, oil-free power transformers and cables will provide a cost-effective, more environmentally friendly option for the utility sector.

3.3 FUNDING

DOE funding for the program, subcontracting activities in 1999, and a summary of funds-out cooperative agreements are shown in Tables 3.1, 3.2, and 3.3.

3.4 TECHNOLOGY PARTNERSHIP APPROACH

Our interdisciplinary approach uses many of the resources available at ORNL to meet the program goals for joint Laboratory–industry development of HTS technology for electric power applications. Our superconductivity agreement mechanism interlinks research and development projects with industry and universities that optimize utilization of facilities, expertise, and program resources for the benefit of all participants. This program also coordinates the ORNL activities with the other national laboratories, government agencies, university centers, and industry groups.

Cooperative agreements ensure that technology development is industry-driven. The Office of Technology Transfer, the Office of Science and Technology Partnerships, and patent counsel work together to place these agreements. Where appropriate, these efforts are coordinated with projects within ORNL that are funded by the DOE Office of Science, as well as Work for Others and ORNL Laboratory Director's Research and Development Fund projects.

Effective funds-out to industry is used to supplement industry cost share. In FY 1999, $4.04 million in funds-out to industry and universities was provided through cooperative agreements and subcontracts. To keep industry involved from the start of the program and to ensure commercialization potential, all of these technology partnering mechanisms are augmented by CRADAs, user agreements, and licensing activities.

Responsiveness to American industry has high priority in this program. An ORNL ad hoc technical review committee, consisting of a project manager, a scientific coordinator, a manager for conductor development, and a manager for applications development, reviews all inquiries from industry and recommends a project for possible funding. This review ensures that (1) the proposed work fits the program mission, (2) the work is collaborative, (3) there is legitimate commercial interest, and (4) the work is feasible. Substantial private-sector cost share is required on cooperative agreements.

ORNL provides support to the DOE Headquarters (DOE-HQ) Superconductivity Program for Electric Power Systems by identifying, guiding, and monitoring research and development at ORNL and ORNL subcontractor sites and by performing coordination, analysis, and planning of activities related to the national program.

Some of the various activities performed as part of this task include the following:

- technical, project, and budget guidance;
- project identification and development;
- exploratory research and development;
- support of consultants and subcontracts providing technical, program, or technology partnering support;
- identification, placement, and technical monitoring of subcontractors, review committee members, and workshop guests;
- guidance and support on technology partnering;
- publication of reports and proceedings from workshops;
- identification and initiation of cooperative agreements, interagency agreements (i.e., National Institute of Standards and Technology), and memoranda of understanding;
- distribution of reports to program managers;
- preparation of assessments to address technical, economic, regulatory, and institutional issues in the DOE program;
- coordination of interlaboratory technical team meetings;
- assistance to the DOE-HQ program manager in preparation of the Superconducting Technology Program Annual Operating Plan;
- collection and dissemination of programmatic information and program-wide assessments;
- assistance in organizing the HTS Wire Development Workshop (in partnership with ANL and LANL); and
- review of industrial collaboration opportunities through multilaboratory meetings and conference calls.

ORNL works with the other program laboratories to address such issues as communication among program participants, workshop and meeting implementation, planned competitive solicitations and superconductivity agreements, and coordination of technical and economic assessments.

An Industrial Overview Committee is charged with reviewing program activities and advising Laboratory management as to program progress, policy, and direction. The committee consists of

representatives of electric utilities, original equipment manufacturers, and HTS wire manufacturers. This committee meets occasionally at ORNL, Argonne National Laboratory (ANL), or Los Alamos National Laboratory (LANL).

3.5 PROGRAM INVENTIONS AND PATENT LICENSE AGREEMENTS

A summary of the new invention disclosures for FY 1999 is shown in Table 3.4. All patent license agreements and issued patents since 1988 are shown in Tables 3.5 and 3.6, respectively.

Table 3.1. Superconducting Technology Program funding: authorization and outlay by fiscal year

	New budget authorization/outlay ($ × 1000)				
	1995	1996	1997	1998	1999
Direct scientific and technical[a]	3,434	2,995	3,046	5,356	5,416
Management and outreach	300	310	310	400	400
Subtotal—ORNL	3,734	3,305	3,356	5,756	5,816
Subcontracts[a]	198	1,290	1,021	2,437	3,244
Funds-out cooperative agreements	611	286	789	589	795
Total program	4,543	4,881	5,166	8,782	9,855

[a]Details are provided in separate table. Funds-out cooperative agreements provide partial financial support to U.S. industry for cost-shared cooperative research and development.

Table 3.2 Superconductivity Program
Summary of cooperative agreements as of September 30, 1999

Participant	Approved Term	Type*	Total Agreement Cost Share ($K) by DOE to ORNL	by DOE to Ind	by Industry	Technology Area
American Superconductor	8/15/96-10/31/2000	FI	1000	0	1785	BSCCO-2223 Wire Development Group and SBIR project
EURUS Technologies	9/9/99-9/9/2001	C	150	0	500	Development of buffered, textured metal substrates for superconducting wires
MicroCoating Technologies	9/15/97-3/31/2000	FI	50	0	1000	Develop coated conductor technology
NIST-Gaithersburg	9/93-11/99	IAG	0	625	625	BSCCO and TBCCO phase diagram support
NIST-Boulder	3/98-2/2001	IAG	0	367	367	Electromechanical properties for superconductor applications
Oxford Instruments	1/94-1/31/2000	C	650	0	875	Develop technology for dip-coated BSCCO-2212 wire and RABiTS
Southwire Company	2/1/97-6/30/2000	FO	2946	500	3408	Develop HTS cable technology
3M	6/1/99-11/30/99	FO	0	150	150	Development of HTS wire using coated conductor technologies
3M-Southwire-LANL-ORNL	4/3/97-8/3/2000	C				Development of HTS wire using coated conductor technologies
3M					2458	
Southwire					480	
LANL			1050	**1680	2938	
ORNL						
Waukesha Electric Systems	6/15/97-12/31/99	FO	234	250	398	HTS transformer
Total Active Agreements			6080	1892	12046	
Total Completed Agreements			13224	5070.6	14552.7	
TOTALS			19304	6962.6	26598.7	

*NFE = No-Funds-Exchange; FO = Funds-Out; FI = Funds-In; IAG = Interagency Agreement, ; and C = CRADA. **DOE to LANL

Table 3.3 FY 1999 active subcontracts

Subcontractor	Term	Obligated Amount	Subject
Imtech	10/3/94-2/29/2000	358	Superconducting powder synthesis/scale-up, strengthened substrates
Massachusetts Institute of Technology	4/29/96-3/31/98 4/1/98-3/31/99 4/1/99-3/31/2000	215 120 120	Stability of HTS conductors and coils
Oak Ridge Institute for Science and Edu.	Ongoing	400	Postdoctoral research fellowships
State University of New York at Buffalo	11/1/95-5/31/96 10/1/96-10/31/97 11/1/97-10/31/98 2/1/99-5/31/99	25 30 50 16	Supply epitaxial films of thallium-based high temperature superconducting materials
University of Tennessee	Ongoing	80	Students (3) - Deposited conductor development
Energetics, Inc.	4/96-7/96 8/96-7/97 8/97-7/98 8/98-2/00	70 450 350 290	Technical and analytical support to ORNL
Bob Lawrence & Associates (competed)	2/17/97-2/16/98 2/17/98-2/16/99 3/15/99-1/14/00	155 220 183	Technical and economic benefits assessment and market study HTS outreach
University of South Carolina	4/1/98-3/31/99 9/1/99-9/30/2000	10 20	High temperature conductor development and characterization
Stanford University (competed)	10/1/98-9/30/01	513	Ion-beam assisted deposition of buffer layers and in-situ deposition of YBCO by electron beam evaporation
University of Wisconsin (competed)	10/1/98-9/30/01	325	BSCCO critical currents and microstructures, YBCO coated conductor microstructure, and pulse tube cryocooler research
University of Houston (competed)	10/1/98-9/30/01	165	Research into high-rate photon-assisted MOCVD for YBCO onto buffered, textured metallic substrates.
Marshall O. Pace	4/97-9/97 11/17/97-11/16/98 12/11/98-12/10/99	10 24 25	High voltage breakdown studies on cryogenic insulation
Western Technology, Inc.	3/1/99-8/31/99	24	Cryogenic system analysis for electric power sector
National Conference of State Legislatures	3/22/99-3/21/00	19	State Legislative Report on Superconductivity
Boston College	6/28/99-1/31/00	49	Development of Epitaxial Film Growth and Properties for Coated Conductors

Table 3.4. Superconducting Technology Program (FY 1999) invention disclosures

ERID No.	Subject[a]	Submitted by
643	Termination for a High Temperature Superconductor Cable System (CRADA ORNL95-0381)	S. W. Schwenterly, J. A. Demko, R. Martin
649	Method of Depositing Buffer Layers on RABiTS™ from Solution	R. K. Williams, D. B. Beach, J. S. Morrell, M. Paranthaman, T. Chirayil, E. D. Specht, A. Goyal
672	High Temperature Superconducting Cable Pressurized Nitrogen Termination	C. A. Foster, P. W. Fisher, M. J. Gouge
726	Method of Depositiong YSZ on RABiTS™ via Pulsed Laser Deposition	D. P. Norton, C. Park, A. Goyal
734	Solution Process for Depositing Rare Earth Zirconium Oxide Buffer layers on Biaxially Textured Metal Substrates for Superconducting Tapes	R. K. Williams, M. Paranthaman, T. Chirayil, D. F. Lee, A. Goyal, R. Feenstra
749	Method and article for fabricating epitaxial oxide films on biaxially textured alloy substrates	A. Goyal, D. M. Kroeger, M. Paranthaman, D. F. Lee, R. Feenstra, and D. P. Norton
757	Multifilament Superconducting Wire for AC Applications	A. Goyal
758	Method of Joining Biaxially Textured Substrates to Enable Fabrication of Superconducting Joints	A. Goyal, S. A. David, and D. M. Kroeger

[a]Numbers in parentheses are cooperative agreement numbers under which the work was conducted.

Table 3.5. Superconducting Technology Program patent license agreements

ID No.	Company
1039-X	Superconductive Components, Inc. (complete)
1640-X (RABiTS™)	Midwest Superconductivity, Inc. (complete)
1640-X (RABiTS™)	Oxford Superconducting Technology
1640-X (RABiTS™)	CCVD, Inc., dba MicroCoating Technologies
1640-X (RABiTS™)	EURUS Technologies
1640-X (RABiTS™)	3M

Table 3.6. Superconducting Technology Program patents issued

Number	Subject	Date issued
5,357,756 (ESID 1185-X)	Bipolar pulse field for magnetic refrigeration	October 25, 1994
5,395,821 (ESID 1039-X)	Method of producing PB-stabilized superconductor precursors and method of producing superconductor articles therefrom	March 7, 1995
5,525,583 (ESID 1471-X)	To American Superconductor for Superconducting Magnetic Coil	June 11, 1996
5,546,261	Hermetically sealed superconducting magnet motor	August 13, 1996
5,646,097	Method of fabricating a (1223) Tl-Ba-Ca-Cu-O superconductor	July 8, 1997
5,739,086	Structures having enhanced biaxial texture and method of fabricating same	April 14, 1998
5,741,377	Structures having enhanced biaxial texture and method of fabricating same	April 21, 1998
5,830,828 (ESID 1193-X)	Process for fabricating continuous lengths of superconductors	November 3, 1998
5,846,912 (ESID 1512-X)	Method for preparation of textured$YBa_2Cu_3O_x$ Superconductor	December 8, 1998
5,898,020	Structures having enhanced biaxial texture and method of fabricating same	April 27, 1999
5,958,599	Structures having enhanced biaxial texture	September 28, 1999

4. Publications and Presentations

S. E. Babcock, C. Y. Yang, J. L. Reeves, Y. Wu, A. E. Polyanskii, D. C. Larbalestier, A. Goyal, M. Paranthaman, F. A. List, D. P. Norton, D. M. Kroeger, and A. Ichinose, "Electromagnetic Connectivity and Microstructure in $YBa_2Cu_3O_{7-d}$ Films on Rolling-Assisted Biaxially-Textured Substrates," *Intergranular and Interphase Boundaries in Materials, Mater. Sci. Forum IIB98*, 294-2, 165–68 (1999).

R. N. Bhattacharya, R. D. Blaugher, Z. F. Ren, W. Li, J. H. Wang, M. Paranthaman, D. T. Verebelyi, and D. K. Christen, "Superconducting Epitaxial $(TlBi)_{0.9}Sr_{1.6}Ba_{0.4}Ca_2Cu_3Ag_{0.2}O_x$ Film from an Electrodeposited Precursor," *Electrochem. and Solid State Lett.*, **1**(4), 165–67 (1998).

R. N. Bhattacharya, P. A. Parilla, R. D. Blaugher, Z. F. Ren, W. Li, J. H. Wang, Y. T. Wang, A. M. Hermann, M. Paranthaman, A. Goyal, D. T. Verebelyi, and D. K. Christen, "Superconducting Thallium Oxide Films from Electrodeposited Precursors," 1681–83 *IEEE Trans. on Appl. Supercond.* **9** (1999).

C. Cantoni, D. P. Norton, D. K. Christen, A. Goyal, D. M. Kroeger, D. T. Verebelyi, and M. Paranthaman, "Transport and Structural Characterization of Epitaxial $Nd_{1+x}Ba_{2-x}Cu_3O_y$ Thin Films Grown on $LaAlO_3$ and Ni Metal Substrates by Pulsed-Laser Deposition," *Physica C* **324**(3–4), 177–86 (1999).

C. Cantoni, D. P. Norton, D. M. Kroeger, M. Paranthaman, D. K. Christen, D. Verebelyi, R. Feenstra, D. F. Lee, E. D. Specht, V. Boffa, and S. Pace, "Phase Stability for the In-Situ Growth of $Nd_{1+x}Ba_{2-x}Cu_3O_y$ Films using Pulsed-Laser Deposition," *Applied Physics Letters* **74**, 96 (1999).

C. Cantoni, D. T. Verebelyi, D. K. Christen, and D. P. Norton, "Effects of Pulsed-Laser Deposition Regimes on Flux-Pinning Properties of YBCO Thin Films," submitted to the Fall 1999 Materials Research Society Meeting, Boston Mass., November 29–December 3.

T. G. Chirayil, M. Paranthaman, D. B. Beach, D. F. Lee, A. Goyal, R. K. Williams, X. Cui, D. M. Kroeger, R. Feenstra, D. T. Verebelyi, and D. K. Christen, "Epitaxial Growth of $La_2Zr_2O_7$ Thin Films on Rolled Ni Substrates by Sol-Gel Process for High T_c Superconducting Tapes," paper submitted to *Physica C*.

T. G. Chirayil, M. Paranthaman, D. B. Beach, J. S. Morrell, C. David, A. Goyal, D. F. Lee, D. M. Kroeger, R. Feenstra, D. T. Verebelyi, and D. K. Christen, "Oxide Buffer Layers on Textured-Ni Substrates by Sol-Gel Process for High Current YBCO Conductors," submitted to the Fall 1999 Materials Research Society Meeting, Boston Mass., November 29–December 3.

T. G. Chirayil, M. Paranthaman, D. B. Beach, J. S. Morrell, E. Y. Sun, A. Goyal, R. K. Williams, D. F. Lee, P. M. Martin, D. M. Kroeger, R. Feenstra, D. T. Verebelyi, and D. K. Christen, "Epitaxial Growth of Yb_2O_3 Buffer Layers on Biaxially Textured Ni (100) Substrates by Sol-Gel Process," *Mat. Res. Soc. Symp. Proc.* **574**, 51–56 (1999).

D. K. Christen,"Critical Currents in Epitaxial YBCO Films: Issues Related to Coated Conductors," submitted to the Fall 1999 Materials Research Society Meeting, Boston Mass., November 29–December 3.

X. Cui, F. A. List, D. M. Kroeger, A. Goyal, D. F. Lee, J. E. Mathis, E. D. Specht, P. M. Martin, R. Feenstra, D. T. Verebelyi, D. K. Christen, and M. Paranthaman, "Continuous Growth of Epitaxial CeO_2 Buffer Layers on Rolled Ni Tapes by Electron Beam Evaporation," *Physica C* **316**, 27–33 (1999).

X. Cui, F. A. List, D. M. Kroeger, A. Goyal, D. F. Lee, J. Mathis, E. D. Specht, P. M. Martin, R. Feenstra, D. T. Verebelyi, D. K. Christen, and M. Paranthaman, "Reel-to-Reel Continuous Deposition of Epitaxial CeO_2 Buffer Layers on Biaxially Textured Ni Tapes by Electron Beam Evaporation," *IEEE Trans. on Appl. Supercond.* **9**, 1967–70 (1999).

J. A. Demko, J. W. Lue, M. J. Gouge, and J. P. Stovall (ORNL) and R. Martin, U. Sinha, and R. L. Hughey (Southwire), "Cryogenic System for a High-Temperature Superconducting Power Transmission Cable," accepted for publication in *Advances in Cryogenic Engineering* **45**.

J. A. Demko, J. W. Lue, U. Sinha, R. L. Hughey, L. Dresner, and S. K. Olsen, "Testing of the Dependence of the Number of Layers on the Performance of a One-Meter HTS Transmission Cable Section," *IEEE Trans. on Appl. Supercond.* **9**, 126–29 (1999).

R. Feenstra, "High J_c YBCO Films on RABiTS and IBAD Substrates via an Ex Situ Process: Correlations with Texture," abstract submitted to 9th U.S./Japan Workshop on High T_c Superconductors, Yamanashi, Japan, October 13–15, 1999.

R. Feenstra, A. Goyal, D. Verebelyi, D. K. Christen, M. Paranthaman, and D. Lee (ORNL) and P. Arendt (LANL), "Grain-to-Grain Correlations and Strong Supercurrent Transport in Ex Situ Processed YBCO Coated Conductors," abstract submitted to Materials and Mechanisms of Superconductivity and High Temperature Superconductors, Feb. 20–25, 2000, Houston, Texas.

R. Feenstra, A. Goyal, D. T. Verebelyi, D. K. Christen, M. Paranthaman, D. F. Lee, E. D. Specht, D. M. Kroeger, P. N. Arendt, R. F. DePaula, and J. R. Groves, "Single-Crystal-Like Supercurrent Transport in RABiTS and IBAD Type YBCO Coated Conductors due to Grain-to-Grain Correlations," abstract submitted to the March 1999 Centennial Meeting of the American Physical Society, Atlanta, Ga.

D. K. Finnemore (Ames Lab), K. E. Gray (ANL), M. P. Maley (LANL), D. O. Welch (BNL), and D. K. Christen and D. M. Kroeger (ORNL), "Coated Conductor Development: An Assessment," *Physica C* **320**, 1–8 (1999).

G. N. Glavee, R. D. Hunt, and M. Paranthaman, "Low Temperature Preparation of $BaCeO_3$ and $Ce_{0.75}Zr_{0.25}O_2$ Thin Films Using Sol-Gel Processing Techniques," *Mater. Res. Bull.* **34**(5), 817–25 (1999).

M. J. Gouge, J. A. Demko, J. W. Lue, J. P. Stovall, R. L. Hughey, R. Martin, and U. Sinha, "HTS Cable Test Facility: Design and Initial Results," *IEEE Trans. on Appl. Supercond.* **9**, 134–37 (1999).

A. Goyal, R. Feenstra, F. A. List, M. Paranthaman, D. F. Lee, D. M. Kroeger, D. B. Beach, J. S. Morrell, T. G. Chirayil, D. T. Verebelyi, X. Cui, E. D. Specht, D. K. Christen, and P. M. Martin, "Using RABiTS to Fabricate High-Temperature Superconducting Wire," *JOM*, 19–23 (July 1999).

A. Goyal, F. A. List, J. Mathis, M. Paranthaman, E. D. Specht, D. P. Norton, C. Parks, D. F. Lee, D. M. Kroeger, D. K. Christen, J. D. Budai, and P. M. Martin, "High Critical Current Density $YBa_2Cu_3O_x$ Tapes Using the RABiTS Approach," *J. of Supercond.* **11**(5) 481–87 (1998).

A. Goyal, S. X. Ren, E. D. Specht, D. M. Kroeger, R. Feenstra, D. Norton, M. Paranthaman, D. F. Lee, and D. K.Christen, "Texture Formation and Grain Boundary Networks in Rolling Assisted Biaxially Textured Substrates and in Epitaxial YBCO Films on Such Substrates," *Micron* **30**, 463–78 (Special Issue, 1999) .

A. Goyal, E. Y. Sun, R. Feenstra,, J. Mathis, C. Park, M. Paranthaman, D. F. Lee, F. A. List, D. P. Norton, P. M. Martin, D. Verebelyi, X. Cui, E. D. Specht, D. M. Kroeger, and D. K. Christen, "High-J_c YBCO Conductors Fabricated by Epitaxial Deposition of YBCO on Strengthened, Nonmagnetic Rolling Assisted Biaxially Textured Substrates (RABiTS)," abstract submitted to the 1999 International Cryogenic Materials Conference, Montreal, Quebec, Canada, July 12–16.

R. A. Hawsey, D. M. Kroeger, and D. K. Christen, "Development of Biaxially Textured $YBa_2Cu_3O_7$ Coated Conductors in the U.S.," paper submitted for publication in *Advances in Superconductivity XII,* Proceedings of the 12th International Symposium on Superconductivity, Morioka, Japan, October 17–19.

Q. He, D. K. Christen, R. Feenstra, D. P. Norton, M. Paranthaman, E. D. Specht, D. F. Lee, A. Goyal, and D. M. Kroeger, "Growth of Biaxially Oriented Conductive $LaNiO_3$ Buffer Layers on Textured Ni Tapes for High-T_c Coated Conductors," *Physica C* **314**, 105–11 (1999).

H. R. Kerchner and D. K. Christen, "Magnetic Field Scanner of High T_c Superconductors," submitted to the Fall 1999 Materials Research Society Meeting, Boston Mass., November 29–December 3.

H. R. Kerchner, D. P. Norton, A. Goyal, J. D. Budai, D. K. Christen, D. M. Kroeger, M. Paranthaman, D. F. Lee, F. A. List, and E. H. Brandt, "Alternating Transport-Current Flow in Superconductive Films: The Role of a Geometrical Barrier to Vortex Motion," *Phys. Rev. B* **60**(9), 6878–83 (1999).

H. R. Kerchner, D. P. Norton, A. Goyal, J. D. Budai, R. Feenstra, D. K. Christen, D. M. Kroeger, E. D. Specht, M. Paranthaman, D. F. Lee, F. A. List, and E. H. Brandt, "Power Loss of AC Transport Current Flow in Superconductive Films,"abstract submitted to the March 1999 Centennial Meeting of the American Physical Society, Atlanta, Ga.

M. N. Kunchur (Univ. of South Carolina) and T. R. Askew, "Hysteretic Internal Fields and Critical Currents in Polycrystalline Superconductors," *J. of Applied Physics* **84**(12), 6763–67 (1998).

J. Y. Lao, J. H. Wang, D. Z. Wang, S. X. Yang, Y. Tu, J. G. Wen, H. L. Wu, Z. F. Ren, D. T. Verebelyi, M. Paranthaman, T. Aytug, D. K. Christen, R. N. Bhattacharya, and R. D. Blaugher, "Synthesis and Characterization of Thallium-Based 1212 Films with High Critical Current Density on $LaAlO_3$ Substrates," *Supercon. Sci. and Technol.* **12** (1999) (in press).

D. F. Lee, M. Paranthaman, J. E. Mathis, A. Goyal, D. M. Kroeger, E. D. Specht, R. K. Williams, F. A. List, P. M. Martin, C. Park, D. P. Norton, and D. K. Christen, "Alternative Buffer Architectures for High Critical Current Density YBCO Superconducting Deposits on Rolling Assisted Biaxially-Textured Substrates," *Jpn. J. Appl. Phys.* **38**, L178–80 (1999).

W. Li, D. Z. Wang, J. Y. Lao, Z. F. Ren, J. H. Wang, M. Paranthaman, D. T. Verebelyi, and D. K. Christen, "Epitaxial Superconducting $Tl_{0.5}Pb_{0.5}Sr_{1.6}Ba_{0.4}Ca_2Cu_3O_9$ Films on $LaAlO_3$ by Thermal Spray and Post-Spray Annealing," *Supercond. Sci. Technol.* **12**, L1–L4 (1999).

F. A. List, A. Goyal, M. Paranthaman, D. P. Norton, E. D. Specht, D. F. Lee, and D. M. Kroeger, "High J_c YBCO Films on Biaxially Textured Ni with Oxide Buffer Layers Deposited Using Electron Beam Evaporation and Sputtering,"*Physica C* **302**, 87–92 (1998).

J. W. Lue, G. C. Barber, J. A. Demko, M. J. Gouge, S. W. Schwenterly, J. P. Stovall, R. Martin, R. L. Hughey, U. Sinha, and J. C. Tolbert, "5-m Single-Phase HTS Transmission Cable Tests," paper submitted for proceedings of 1999 Cryogenic Engineering and International Cryogenic Materials Conference, Montreal, Canada, July 12–16.

J. W. Lue, J. A. Demko, L. Dresner, R. L. Hughey, U. Sinha, J. C. Tolbert, and S. K. Olsen, "AC Losses of Prototype HTS Transmission Cables," *IEEE Trans. on Appl. Supercond.* **9**, 416–19 (1999).

J. W. Lue, J. A. Demko, M. J. Gouge, R. L. Hughey, U. Sinha, and J. C. Tolbert, "AC Loss of 5-m HTS Transmission Cables," abstract submitted to Workshop on AC Losses, EPRI, Palo Alto, Calif., April 8–9, 1999.

J. W. Lue, M. S. Lubell, and M. J. Tomsic, "AC Losses of HTS Tapes and Bundles With De-Coupling Barriers" *IEEE Trans. on Appl. Supercond.* **9**, 793–96 (1999).

P. Maheswaranathan, D. K. Christen, H. R. Kerchner, D. T. Verebelyi, and J. E. Mathis, "A High-Temperature Superconducting Thin-Film Meander as a Superconducting Switch," *American Journal of Physics* (submitted).

A. P. Malozemoff, S. Annavarapu, L. Fritzemeier, Q. Li, V. Prunier, M. Rupich, C. Thieme, and W. Zhang (American Superconductor) and A. Goyal, M. Paranthaman, and D. F. Lee (ORNL), "Low-Cost YBCO Coated Conductor Technology," paper given at the European Conference on Applied Superconductivity, Sept. 14–17, Sitges, Barcelona, Catalonia, Spain.

J. E. Mathis, A. Goyal, D. F. Lee, F. A. List, M. Paranthaman, D. K. Christen, E. D. Specht, D. M. Kroeger, and P. M. Martin, "Biaxially Textured $YBa_2Cu_3O_{7-\delta}$ Conductors on Rolling Assisted Biaxially Textured Substrates with Critical Current Densities of 2-3 MA/cm^2," *Jpn. J. Appl. Phys*. **37**, L1379–82 (1998).

I. Matsubara, M. Paranthaman, S. W. Allison, M. R. Cates, D. L. Beshears, and D. E. Holcomb, "Preparation of Cr-doped $Y_3Al_5O_{12}$ Phosphors by Heterogeneous Precipitation Methods and Their Luminescent Properties," *Materials Research Bulletin* (in press).

I. Matsubara, M. Paranthaman, T. Chirayil, E. Y. Sun, P. M. Martin, D. M. Kroeger, D. T. Verebelyi, and D. K. Christen,"Preparation of Epitaxial $YbBa_2Cu_3O_{7-\delta}$ on $SrTiO_3$ Single Crystal Substrates Using a Solution Process," *Jpn. J. Appl. Phys.* **38**, L727–30 (1999).

I. Matsubara, M. Paranthaman, A. Singhal, C. Vallet, D. F. Lee, P. M. Martin, R. D. Hunt, R. Feenstra, Chau-Yun Yang, and S. E. Babcock, "Preparation of Textured YBCO Films Using All-Iodide Precursors," *Physica C* **319**, 127–32 (1999).

J. S. Morrell, Z. B. Xue, E. D. Specht, A. Goyal, P. M. Martin, D. F. Lee, R. Feenstra, D. T. Verebelyi, D. K. Christen, T. G. Chirayil, M. Paranthaman, C. E. Vallet, and D. B. Beach, "Epitaxial Growth of Gadolinium Oxide on Roll-Textured Nickel Using a Solution Growth Technique," *J. Mater. Res.* (in press).

B. W. McConnell, J. W. VanDyke, and J. W. Mulholland, "Market Impacts of the Economic and Engineering Performance of High Temperature Superconductors in Electric Power Applications," abstract submitted to the International Conference on Electricity Distribution, Nice, France, June 1–4, 1999.

D. P. Norton, C. Park, C. Prouteau, D. K. Christen, M. F. Chisholm, J. D. Budai, A. Goyal, E. Y. Sun, D. F. Lee, D. M. Kroeger, E. Specht, M. Paranthaman, and N.D. Browning, "Epitaxial $YBa_2Cu_3O_7$ Films on Rolled-Textured Metals for High Temperature Superconducting Applications," *Materials Science and Engineering B—Solid State Materials for Advanced Technology* **56**, 86–94 (1998).

M. Paranthaman and B. C. Chakoumakos, "Synthesis and Characterization of Bulk $HgBa_2Ca_{N-h1}Cu_NO_{2N+2+\delta}$ (N=1,2,3,4) Superconductors," pp. 133–52 in *Studies of High Temperature Superconductors*, Vol. 26, Nova Science Publishers.

M. Paranthaman and B. C. Chakoumakos, "Synthesis and Characterization of the Superconducting Quaternary Intermetallic Compound YNi_2B_2C—A Review," pp. 97–112 in *Studies of High Temperature Superconductors*, Vol. 26, Nova Science Publishers.

M. Paranthaman, T. G. Chirayil, J. S. Morrell, D. B. Beach, F. A. List, A. Goyal, X. Cui, D. F. Lee, E. D. Specht, D. M. Kroeger, R. Feenstra, D. P. Norton, and D. K. Christen, "Reel-to-Reel Dip-Coating Unit for Fabricating Long RABiTS for HTS Coated Conductors," submitted to the Fall 1999 Materials Research Society Meeting, Boston Mass., November 29–December 3.

M. Paranthaman, R. Feenstra, D. F. Lee, D. B. Beach, J. S. Morrell, T. G. Chirayil, A. Goyal, X. Cui, D. T. Verebelyi, J. E. Mathis, P. M. Martin, D. P. Norton, E. D. Specht, D. K. Christen, and D. M. Kroeger, "Demonstration of High Current Density YBCO Coated Conductors on Re_2O_3 Buffered Ni Substrates with Two New Alternative Architectures," paper submitted for proceedings of 1999 Cryogenic Engineering and International Cryogenic Materials Conference, Montreal, Canada, July 12–16.

M. Paranthaman, A. Goyal, D. P. Norton, D. F. Lee, E. D. Specht, P. M. Martin, D. M. Kroeger, D. K. Christen, C. Park, and J. E. Mathis, "Fabrication of High Current $YBa_2Cu_3O_{7-y}$ Coated Conductors Using Biaxially Textured Buffer Layers on Rolled-Ni Substrates" pp. 169–76 in *Proc. of 9th Cimtec-World Forum on New Materials, Symposium VI – Science and Engineering of HTC Superconductivity*, ed. P. Vincenzini, Techna Srl, 1999.

M. Paranthaman, D. F. Lee, R. Feenstra, A. Goyal, D. T. Verebelyi, D. K. Christen, E. D. Specht, F. A. List, P. M. Martin, D. M. Kroeger, Z. F. Ren, W. Li, D. Z. Wang, J. Y. Lao, and J. H. Wang, "Optimization of Buffer Layers on Rolled-Ni Substrates for High Current YBCO and Tl,Bi-1223 Coated Conductors Using Ex-Situ Precursor Approaches," *IEEE Trans. on Appl. Supercond.* **9**, 2268–71 (1999).

M. Paranthaman, D. F. Lee, A. Goyal, E. D. Specht, P. M. Martin, X. Cui, J. E. Mathis, R. Feenstra, D. K. Christen, and D. M. Kroeger, "Growth of Biaxially Textured RE_2O_3 Buffer Layers on Rolled-Ni Substrates Using Reactive Evaporation for HTS-Coated Conductors," *Supercond. Sci. Technol.* **12,** 319–25 (1999).

M. Paranthaman, D. F. Lee, E. D. Specht, P. M. Martin, X. Cui, J. E. Mathis, R. Feenstra, D. K. Christen, and D. M. Kroeger, "Growth of Biaxially Textured RE_2O_3 Buffer Layers on Rolled-Ni Substrates Using Reactive Evaporation for HTS-Coated Conductors," *Supercond. Sci. Technol.* **12**, 31–25 (1999).

M. Paranthaman, S. S. Shoup, D. B. Beach, J. S. Morrell, A. Goyal, E. D. Specht, J. E. Mathis, D. T. Verebelyi, and D. K. Christen, "Growth of Textured Buffer Layers and Superconductors on Rolled Ni Substrates Using Sol-Gel Alkoxide Precursors" pp. 185–92 in *Proc. of 9th Cimtec-World Forum on New Materials, Symposium VI – Science and Engineering of HTC Superconductivity*, ed. P. Vincenzini, Techna Srl, 1999.

P. A. Parilla, C. M. Carlson, Y. T. Wang, R. N. Bhattacharya, R. D. Blaugher, D. S. Ginley, M. Paranthaman, A. Goyal, D. K. Christen, and D. M. Kroeger, "Buffer Layers and Thallination of Tl-based Superconductors on Flexible Metal Substrates," *IEEE Trans. on Appl. Supercond.* **9**, 1673–76 (1999).

C. Park, D. P. Norton, J. D. Budai, D. K. Christen, D. Verebelyi, R. Feenstra, D. F. Lee, A. Goyal, D. M. Kroeger, and M. Paranthaman, "Bend Strain Tolerance of Critical Currents for $YBa_2Cu_3O_7$ Films Deposited on Rolled-Textured (001) Ni," *Appl. Phys. Lett.* **73**(13), 1904–1906 (1998).

C. Park, D. P. Norton, D. K. Christen, D. T. Verebelyi, R. Feenstra, J. D. Budai, A. Goyal, D. F. Lee, E. D. Specht, D. M. Kroeger, "Long Length Fabrication of YBCO on Rolling Assisted Biaxially Textured Substrates (RABiTS) Using Pulsed Laser Deposition," *IEEE Trans. on Appl. Supercond.* **9**, 2276–79 (1999).

Z. F. Ren, W. Li, D. Z. Wang, J. Y. Lao, J. H. Wang, M. Paranthaman, D. T. Verebelyi, D. K. Christen, "Growth and Characterization of Superconducting Films $Tl_{0.78}Bi_{0.22}Sr_{1.6}Ba_{0.4}Ca_2Cu_3O_9$ on CeO_2-Buffered Single Crystal YSZ," *Physica C* **306**, 149–53 (1998).

Z. F. Ren, W. Li, D. Z. Wang, J. Y. Lao, J. H. Wang, M. Paranthaman, D. T. Verebelyi, D. K. Christen, D. F. Lee, A. Goyal, D. M. Kroeger, "In-Plane Aligned Superconducting $Tl_{0.78}Bi_{0.22}Sr_{1.6}Ba_{0.4}Ca_2Cu_3O_9$ Films on Rolling Assisted Biaxially Textured Substrates," *Physica C* **313**(3–4), 241–45 (1999).

M. W. Rupich, W. Palm, W. Zhang, E. Siegal, S. Annavarapu, L. Fritzemeier, M. D. Teplinsky, C. Thieme, M. Paranthaman, "Growth and Characterization of Oxide Buffer Layers for YBCO Coated Conductors," *IEEE Trans. on Appl. Supercond.* **9**,1527–30 (1999).

I. Sauers, *Effect of Outgassing on AC and Impulse Surface Flashover of Fiberglass Reinforced Epoxy Composite Insulation in Vacuum*, abstract submitted to the 1999 Cryogenic Engineering Conference, Montreal, Quebec, Canada, July 12–16.

I. Sauers, D. R. James, H. Rodrigo, M. O. Pace, B. W. McConnell, V. P. Patania, and A. R. Ellis, "Surface Flashover of Fiberglass Reinforced Epoxy Composite Insulation in Vacuum at Liquid Nitrogen and Room Temperatures using Power Frequency ac and Lightning Impulse Waveforms," paper submitted for proceedings of 1999 Cryogenic Engineering and International Cryogenic Materials Conference, Montreal, Canada, July 12–16.

S. W. Schwenterly, "High Voltage Testing of Superconducting Power Apparatus," *Cryogenics* **38**(11), 1051–90 (1998).

S. W. Schwenterly, M. D. Carter, F. R. Chang-Diaz, and J. P. Squire, "HTS Magnets for Advanced Magnetoplasma Space Propulsion Systems," accepted for publication in *Advances in Cryogenic Engineering*.

S. W. Schwenterly, S. P. Mehta, and M. S. Walker, "Development of Cryogenic High Voltage Bushings for Utility Power Equipment," abstract submitted to the 1999 Cryogenic Engineering Conference, Montreal, Quebec, Canada, July 12–16.

A. Sheth, V. Lasrado, M. White, and M. Paranthaman,"Bench Scale Evaluation of Batch Mode Dip-Coating of Sol-Gel $LaAlO_3$ Buffer Materials," *IEEE Trans. on Appl. Supercond.* **9**, 1514–18 (June 1999).

S. S. Shoup, M. Paranthaman, A. Goyal, E. D. Specht, D. F. Lee, D. M. Kroeger, and D. B. Beach, "Epitaxial Thin Film Growth of Lanthanum and Neodymium Aluminate Films on Roll-Textured Nickel Using a Sol-Gel Method," *J. Am. Ceram. Soc.* **81**(11), 3019–21 (1998).

S. S. Shoup, S. Shanmugham, D. Cousins, A. T. Hunt, M. Paranthaman, A. Goyal, P. M. Martin, and D. M. Kroeger, "Low-Cost Combustion Chemical Vapor Deposition of Epitaxial Buffer Layers and Superconductors," *IEEE Trans. on Appl. Supercond.* **9**, 2426–29 (1999).

V. F. Solovyov, H. J. Wiesmann, M. Suenaga, and R. Feenstra, "Thick $YBa_2Cu_3O_7$ Films by Post Annealing of the Precursor by High Rate e-Beam Deposition on $SrTiO_3$ Substrates," *Physica C* **309(**3–4), 269–74 (1998).

E. D. Specht, A. Goyal, D. F. Lee, F. A. List, D. M. Kroeger, M. Paranthaman, R. K. Williams, and D. K. Christen, "Cube-textured Nickel Substrates for High-temperature Superconductors," *Supercond. Sci. Technol.* **11**, 945–49 (1998).

E. Y. Sun, A. Goyal, D. P. Norton, C. Park, D. M. Kroeger, M. Paranthaman, and D. K. Christen, "High-Resolution Transmission Electron Microscopy/analytical Electron Microscopy Characterization of Epitaxial Oxide Multilayers Fabricated by Laser Ablation on Biaxially Textured Ni," *Physica C* **321**, 29–38 (1999).

D. T. Verebelyi, D. K. Christen, R. Feenstra, and C. Prouteau, "Critical Current of YBCO Grain Boundaries in High Magnetic Field," abstract submitted to the March 1999 Centennial Meeting of the American Physical Society, Atlanta, Ga.

D. T. Verebelyi, R. Feenstra, A. Goyal, D. K. Christen, C. Prouteau, and P. N. Arendt, "Critical Current and Low Angle Grain Boundaries in YBCO Coated Conductors," submitted to the Fall 1999 Materials Research Society Meeting, Boston Mass., November 29–December 3.

D. T. Verebelyi, R. Feenstra, A. Goyal, D. K. Christen, C. Prouteau, P. N. Arendt, R. F. DePaula, and J. R. Groves, "Effects of Grain Boundaries on the Critical Current of YBCO Coated Conductors," extended abstract submitted to 9th International Workshop on Critical Currents, Madison, Wis., July 7–10, 1999.

R. K. Williams, P. M. Martin, and J. O. Scarbrough,"Thermal Conductivity of Partially Substituted $YBa_2Cu_3O_{7-\delta}$," *Physical Review B*, **59**(21) (1999).

Chau-Yun Yang, S. E. Babcock, A. Goyal, M. Paranthaman, F. A. List, D. P. Norton, D. M. Kroeger, A. Ichinose, "Microstructure of Electron-Beam-Evaporated Epitaxial Yttria-Stabilized Zirconia/CeO_2 Bilayers on Biaxially Textured Ni Tape," *Physica C* **307**, 87–98 (1998).

INTERNAL DISTRIBUTION

1. D. B. Beach
2. D. K. Christen
3. L. M. Dickens
4. L. B. Dunlap
5. R. G. Gilliland
6. M. J. Gouge
7-16. R. A. Hawsey
17-21. W. Koncinski
22. D. M. Kroeger
23. M. Paranthaman
24. A. C. Schaffhauser
25. J. P. Stovall
26. R. K. Williams
27-28. Laboratory Records Dept.
29. Laboratory Records—RC
30. Central Research Library

EXTERNAL DISTRIBUTION

31. L. Adams, EURUS Technologies, 2031 East Paul Dirac Dr., Innovation Park, Tallahassee, FL 32310
32. N. Aversa, Consultant, Waukesha Electric Systems, 400 S. Prairie Ave., Waukesha, WI 53186-5937
33. U. Balachandran, Argonne National Laboratory, ET/212, 9700 South Cass Avenue, Argonne, IL 60439-4838
34. R. D. Blaugher, National Renewable Energy Laboratory, 1617 Cole Boulevard, Golden, CO 80401
35. S. Bray, National Institute of Standards and Technology, 325 Broadway, Boulder, CO 80303
36. J. G. Daley, EE-15, U.S. Department of Energy, 6H-034/FORS, 1000 Independence Avenue, S.W., Washington, DC 20585.
37. R. Dixon, EE-15, U.S. Department of Energy, 1000 Independence Ave. SW, Washington, D.C. 20585.
38. D. Driscoll, Rockwell Automation, 24800 Tungsten Road, Cleveland, OH 44117
39. K. Efferson, American Magnetics, Inc., P.O. Box 2509, Oak Ridge, TN 37831-2509
40. J. Ekin, National Institute of Standards and Technology, 325 Broadway, Boulder, CO 80303
41. G. H. Epstein, Intermagnetics General Corporation, P.O. Box 461, Latham, NY 12110-0461
42. L. B. Fritzemeier, American Superconductor Corporation, Two Technology Drive, Westborough, MA 01581
43. A. Funkenbusch, 3M Corporate Research Tech. Dev. Laboratory, 3M Center Bldg. 218-1-05, St. Paul, MN 55144-1000
44. R. L. Hughey, Jr., Southwire Company, P. O. Box 1000, Carrollton, GA 30119
45. A. T. Hunt, MicroCoating Technologies, 3901 Green Industrial Way, Chamblee, GA 30341
46. R. H. Jones, Rochester Gas and Electric, 89 East Avenue, Rochester, NY 14649-0001

47. D. C. Larbalestier, University of Wisconsin–Madison, Applied Superconductivity Center, 1500 Engineering Drive, Madison, WI 53706-1687
48. W. C. Lin, U.S. Department of Energy, Office of Assistant Manager for Energy Research and Development, Oak Ridge Field Office, P.O. Box 2008, Oak Ridge, TN 37831-6269
49. K. R. Marken, Jr., Oxford Superconducting Technology, P.O. Box 429, Carteret, NJ 07008-0429
50. S. P. Mehta, Waukesha Electric Systems, 400 S. Prairie Ave., Waukesha, WI 53186-5937
51. C. E. Oberly, WL/POOX-2, Aerospace Power Div., Wright Laboratory, 2645 Fifth St., WPAFB OH 45433-6563
52. J. Parks, EE-15, U.S. Department of Energy, Office of Utility Technologies, 1000 Independence Avenue, S.W., Washington, DC 20585.
53. D. E. Peterson, Los Alamos National Laboratory, Superconductivity Technology Center, P.O. Box 1663, MS K763, Los Alamos, NM 87545
54. W. C. Pittman, Hqtrs, U.S. Army Aviation and Missile Command, Attn: AMSAM-RD-MG, Redstone Arsenal, AL 35898-5000
55. E. Pleva, Waukesha Electric Systems, 400 S. Prairie Ave., Waukesha, WI 53186-5937
56. G. B. Riley, American Superconductor Corporation, Two Technology Drive, Westborough, MA 01581
57. J. Romans, EURUS Technologies, 2031 East Paul Dirac Dr., Innovation Park, Tallahassee, FL 32310
58. M. W. Rupich, American Superconductor Corporation, Two Technology Dr., Westborough, MA 01581
59. S. S. Shoup, MicroCoating Technologies, 3901 Green Industrial Way, Chamblee, GA 30341
60. U. K. Sinha, Southwire Company, One Southwire Drive, Carrollton, GA 30119
61. J. Storer, 3M Industrial and Consumer Sector, 3M Center, Bldg. 60-1N-01, St. Paul, MN 55144-1000
62. M. Suenaga, Brookhaven National Laboratory, Bldg. 480, P. O. Box 5000, Upton, Long Island, NY 11973-5000
63. M. J. Tomsic, Plastronic, Inc., 110 E. Canal St., Troy, OH 45373
64. T. Vanderah, National Institute of Standards and Technology, Ceramics Division, Building 223, A-256, Gaithersburg, MD 20899
65. J. Voight, Sandia National Laboratories, MS 1405, P.O. Box 5800, Albuquerque, NM 87185-1405
66. J. E. Wagner, Waukesha Electric Systems, 400 S. Prairie Ave., Waukesha, WI 53186-5937
67. M. S. Walker, Intermagnetics General Corporation,450 Duane Ave., Schenectady, NY 12304.
68. D. O. Welch, Brookhaven National Laboratory, Materials Science Division, Upton, Long Island, NY 11973
69. J. V. Worth, Oxford Superconducting Technology, P.O. Box 429, Carteret, NJ 07008-0429
70. G. J. Yurek, American Superconductor Corporation, Two Technology Drive, Westborough, MA 01581